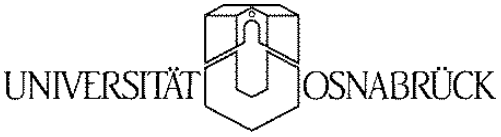

Beiträge des Instituts für Umweltsystemforschung der Universität Osnabrück

Herausgeber: Prof. Dr. Michael Matthies

Beitrag Nr. 33

Micelles as Containers for Protocells

Harold Fellermann

Dezember 2005

ISSN-Nr. 1433-3805

Beiträge des Instituts für Umweltsystemforschung der Universität Osnabrück

ISSN 1433-3805

Herausgeber

Prof. Dr. Michael Matthies
Universität Osnabrück
Institut für Umweltsystemforschung
Artilleriestr. 34

D-49069 Osnabrück

Tel. 0541/969-2575
Fax. 0541/969-2599

E-Mail: matthies@uos.de
http://www.usf.uni-osnabrueck.de

Abstract

We extended the mesoscopic simulation method Dissipative Particle Dynamics to incorporate chemical reactions on the basis of rate equations. With the extended model, we analyzed micellar systems in the context of early life and artificial protocells. We studied whether micelles have the potential to serve as embodiments for protocells, i. e. whether they are able to grow in size and divide into two daughter cells. It was found that the ability of micelles to grow depends on the pathway new surfactants are provided: micelles grow only if new surfactants are provided faster than the monomers dissociate from the assembly. We compared the growth scenario of two distinct scenarios that envision micelles as protocells: the origin of life theory "Lipid World" and the currently explored artificial protocell "Los Alamos bug". We found that relaxation in micellar kinetics is likely to jeopardize the pathway proposed by the Lipid World theory, but not the "Los Alamos bug". We finally developed a toy model that delineates the whole life-cycle of the "Los Alamos bug".

Key words: dissipative particle dynamics, artificial life, origin of life, micelles, artificial protocell, Lipid World, Los Alamos bug

Contents

Chapter 1

Introduction

Despite a long history of scientific tinkering, the transition from nonliving to living matter is still a poorly understood phenomenon. The obstacles in understanding the processes that lead to nowadays or even the very first organisms are manifold: contemporary life is far too sophisticated to give insight into its very origin; no fossil remnants of this origin can be found on todays earth; and last but not least, the single implementation of life as we know it makes it hard if not impossible to distinguish between generic and singular properties of this transition. Surely, whichever way had been taken towards nowadays organisms, a wide range of intermediate systems of increasing organizational complexity must have been passed, and no particular step on this path can be singled out as the exact boundary between nonliving and living matter.

One of the major steps in the evolution of early life was the emergence of cellular organisms, i. e. the transition from loose chemical reaction networks in a premordial soup to embodied entities. There is evidence that encapsulation of chemcial reactions increases the achievable complexity in prebiotic reaction systems, e. g. by allowing for spatial heterogeneity and interface processes [1]. Furthermore, encapsulation is a necessity for reaching basic autonomy. The importance of encapsulation in the early evolution of life has already been pointed out in the 1930s by Aleksandr I. Oparin, whose scenario of the origin of life is based on the *coacervation* or self-aggregation of lipids to supramolecular assemblies:

> "At first there were the simple solutions of organic substances, the behavior of which was governed by the properties of their component atoms and the arrangement of those atoms in the molecular structure. But gradually, as the result of growth and increased complexity of the molecules, new properties have come into being and a new colloidal-chemical order was imposed on the more simple organic chemical relations. These newer properties were determined by the spatial arrangement and mutual relationship of the molecules... In this process biological orderliness already comes into prominence. Competition, speed of growth, struggle for existence and, finally, natural selection determined such a form of material organization which is characteristic of living things of the present time." [2]

All nowaday organisms are encapsulated in phospholipid membranes with embedded

proteins. However, in its actual composition, these membranes are far too complex to serve as potential embodiments for the very origin of cellular life. One of the involved problems is for example, that a lipid membrane prohibits the supply of nutrients from the environment unless it contains pore proteins to regulate the diffusion of resources through the membrane. However, it seems unlikely that such sophisticated molecules as pore proteins have been present in the very first organism. Therefore, alternative ways of encapsulation—namely oil droplets and micelles—have been proposed as intermediate steps towards more sophisticated cells.
In this work, we examine whether micelles are applicable as protocellular containers. To serve as container of a protocell which is able to reproduce itself, micelles must be able to grow and—when their size reaches a certain threshold—divide into two daughter micelles. The growth of micellar aggregates by catalytic reactions has been experimentally studied by Pascale A. Bachmann, Pier L. Luisi and Jacque Lang [3] and has later achieved theoretical support [4]. Less attention has been payed to the actual division of a micellar protocell. In this work, we focus on the kinetics of micellar systems using dissipative particle dynamics—a mesoscopic simulation technique of the family of coarse grained molecular dynamics.
We will apply our model to two different systems, where micelles are envisioned to play the role of a protocellular containers. The first one is the so-called *Lipid World* scenario which has been introduced into the debate on the origin of life by Doron Lancet and co-workers. The second is the *Los Alamos bug* designed by Steen Rasmussen et al. as an attempt to create an artificial protocell.

The document is structured as follows: in the remainder of this chapter, we introduce the protocellular scenarios we aim to model—we ouline the general scenario and the work done so far.
Chapter 2 summarizes properties of micellar systems known from experiments and theories. These properties are obtained from equilibrium systems. However, the knwoledge we present is also valuable for the non-equilibrium cases, that we describe.
The model used in this study—Dissipative Particle Dynamics—is described in chapter 3. We give a general introduction of the method, discuss its relation to microscopic (atomistic) as well as macroscopic (continuous) models, as well as its mesoscopic (thermodynamic) properties. We describe how we extended the standard formalism to incorporate chemical reactions. Former applications of the method are briefly presented in section 3.6.
In chapter 4, we present the results of four different scenarios, that we have analyzed in this work. In section 4.1, we studied a pure aqueous system. We performed these simulation to validate the method and gain insight into the simulation, that is used in the latter. In section 4.2, we studied a single component micellar system. We show how the method can be related to physical length and time scales of the system and present results for the equilibrium scenario. We further present results for a scenario, where a chemical reaction is introduced to drive the system out of its equilibrium. 4.3 summarizes results of modelling the Lipid World with several parameter sets. In 4.4 perform simulations on several aspects of the Los Alamos bug.
The above results will be discussed in chapter 4. We discuss artefacts of the model and how they affect the outcome of our simulations. We compare the growth sce-

narios of the Lipid World and the Los Alamos bug. We will come to the conclusion, that only the scenario implemented by the Los Alamos bug is likely to allow micelles to serve as protocellular containers.

1.1 The Lipid World

One proposal to overcome the gap between simple autocatalytic reactions and the higher ordered organization of early cellular life has been introduced by Doron Lancet and Daniel Segré in the early 1980s. In the so-called *Lipid World Scenario*, amphiphilic molecules themself—the building blocks of micelles and membranes—are subject to evolutionary selection and therefore have a hereditary potential. They actually play the role of a preliminary genome before intricate biopolymer templates like RNA emerged.
In the theory of Lancet, proto-organisms are supramolecular assemblies of a variaty of different amphiphiles. These assemblies are located in a premordial soup of precursor molecules that can synthesize into new amphiphiles. Assemblies are supposed to undergo a replication-like behavior: in the scenario of Lancet et al. they grow by the incorporation of new synthesized amphiphiles, until they reach a critical size, bezond which they are supposed to become unstable and divide into two smaller aggregates. Although the theory of Lancet et al. is in principle not restricted to a certain type of assembly, micelles are envisioned to be the aggregates of choice for this early biotic scenario.
Based on experimental results (see [3], [5], as well as references therein), Lancet and co-workers assume, that many amphiphiles are able to possess auto- and cross-catalytic activity for the synthesis of new amphiphiles. They call these amphiphiles *lipozymes* in imitation of the terms *enzymes* and *ribozymes*. Auto- and cross-catalytic lipozymes finally form a catalytic network, in which catalytic cycles can compete for precursor molecules. In this way catalytic cycles become subject of an evolutionary selection process:

> "We propose that crucial steps in the origin of life might have been carried out by lipid-like molecules alone, potentially prior to the emergence of polynucleic acids and polypeptides. We suggest that heterogeneous autocatalytic lipozymes with defined internal compositions might have been gradually selected out of an initial highly complex repertoire of micelles and vesicles formed spontaneously by abiotic processes." [5]

Segré and Lancet developed a mathematical model to back up their hypothesis of possible evolution in such catalytic micellar systems [6, 7, 8]. The *Graded Autocatalysis Replication Domain* (GARD) model consists a set of N_G amphiphiles, that can be synthesized from an unlimited precurser supply. Amphiphiles are organized in micelles, that are composed of n_i molecules of type i where $i = 1, \ldots, N_G$ (see figure 1.1). In the GARD model, however, the micelles are only represented as multisets over $\{1, \ldots, N_G\}$, that is, only the composition of the micelles is modeled, not their spatial configuration. The micelles grow by the incorporation of amphiphiles whose synthesese are catalyzed by the present amphiphiles in the micelles (β_{ij} in figure

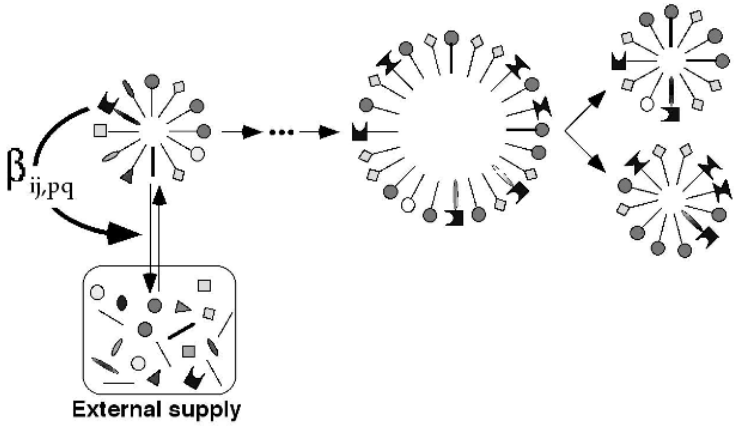

Figure 1.1: In the GARD model of the Lipid World, micelles are composed of many different amphiphiles. The different head groups of the amphiphiles act as catalysts for the creation of other amphiphiles from an external supply of precursor. New synthesized amphiphiles are supposed to enter the assembly that grows to critical size where it divides into two daughter aggregates [9].

1.1). Segré and Lancet assume that a micelle splits into two daughter assemblies, once a critical size N has been reached. To keep the model simple, the authors observe only the evolutionary path of the micelle that reproduces fastest—once a micelle divides, its daughters replace the former generation. This generation cycle introduces a selective pressure in the model.

Segré and Lancet could show that for the case $N_G \gg N$ an initially homogeneous amphiphile distribution is rapidely biased by this selective pressure, i. e. catalytic cycles reduce the number of amphiphiles present in the micelle. They could further show that after an initial transient, the amphiphilic composition of micelles remains rather stable over many generations, thus, the information stored in this composition is inherited. Lancet et al. therefore call this information the compositional genome of the system and stress out, that it could have played a functional role in the early evolution of life, probably before more complex information carrier like biopolymers had been established. For more detailed description of the GARD model and its analysis, see [6].

One of the drawbacks of the GARD model is the simplistic modelling of micellar kinetics [10] and the ignorance of space in the simulation [11], although the fission process of amphiphilic aggregates might be significantly influenced by the arrangement of surfactants on the surface into domains (see figure 1.2). Domain formation in amphiphilic aggregates is both experimentally and theoretically a well known phenomenon. Due to different physico-chemical properties of the involved molecules, the chemical potential of amphiphiles near the domain boundary is higher than inside a domain. This is the driving force for the growth of such domains. Temperature and entropy, on the other hand, limit the domain growth. Such domain formation can even induce the budding and fission of small vesicles from the origin vesicle [12, 13].

Domain formation is also known from a certain type of micelles, called binary bilayered mixed micelles or just *bicelles*. Bicelles are composed of two amphiphiles

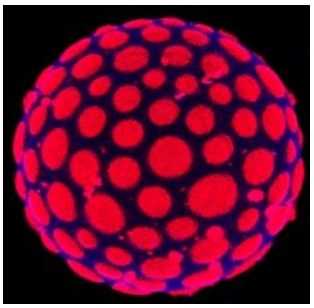

(a) Domain formation of sphingomyelin, cholesterol and another phospholipid on a giant unilamellar vesicle [12].

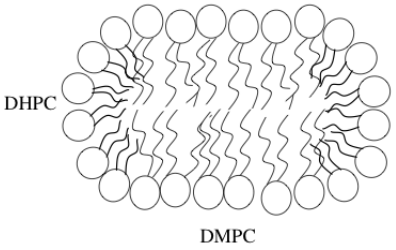

(b) Schematic cut through a bicelle showing the two amphiphilic domains [14].

Figure 1.2: Domain formation in mixed amphiphile aggregates: mixed vesicles (a) and bicelles (b).

with different surfactant parameter. Therefore the two surfactants assemble into domains with different curvature. The resulting shape is a disclike aggregate where one domain forms a flat bilayer which is surrounded by a hoop-shaped cap domain. The ration of the two surfactants determines the size of these discs.
In this work, the impact of space on the dynamics of the Lipid World is analyzed for the first time. The affect of more realistic micellar kinetics on the generation cycle of Lancet et al.'s theory will also be discussed.

1.2 The Los Alamos Bug

The second system of our studies is a proposal for an artificial protocell, that is intented to be build *vitro* as a minimal molecular machine, able to undergo self-replication and finally evolution. While this project will deepen the transition from non-living to living matter, it is also meant as a starting point for new technolgy based on living matter.
Although there is a controversal debate about the definition of life, there is a general agreement that a system, in order to be called alive, must be able to self-maintain its structure, to self-reproduce, and eventually to undergo evolution. These functionalities are provided by three components: container, metabolism, and genome, i. e. inheritable information that influences the functioning of the organism. Many different designs of such proto-organisms have been proposed that differ in the actual coupling between these components [15, 16, 17, 18, 19]. The minimal organism analyzed in this work—the Los Alamos bug—has been proposed by Steen Rasmussen, Liaohai Chen and co-workers in 2003 [18].
In the Los Alamos bug, the three ingredients for container, metabolism and genome are fatty acid surfactants, sensitizer molecules and single stranded PNA (peptide nucleic acid). In aqueous solution, fatty acids assemble into micelles—orders of

magnitude smaller than phospholipid vesicles. The sensitizer is an aromatic molecule and will therefore agglomerate in the interior of the micelle. In Rasmussen et al.'s design, the PNA is decorated with hydrophobic anchors. However, the nucleic acids exhibit numerous hydroxyl groups turning the single strand into an amphiphile. Hence, it is supposed to stick at the surface of the micelle. Such a loaded micelle forms the complete protocell (see figure 1.3.2).

The metabolism transforms externally provided precursors into building blocks of the protocell. Supplied resources are sensitizers, surfactant precursors, and PNA precursors two nucleotides in length. In the envisioned chemical implementation, precursors are esters. The sensitizer uses light energy to break the ester bonds and thereby transform the precursors into actual surfactants and PNA dimers which can then polymerize into longer oligomers (figure 1.3.4). Nearby nucleotides can act as charge relays to prevent a backward reaction to the esters. Because the efficiency of this prevention depends on the actual type of bases, the information stored in the PNA incluences the functioning of the metabolism, turning the template into an actual genome.

The protocell grows with the incorporated nutrients. With the reach of a critical size, the container becomes unstable and divides into two daughter cells (figure 1.3.6). Supposed that nutrients are provided in the right stoichiometric ratio, the two daughter cells will be replicates of the original organism.

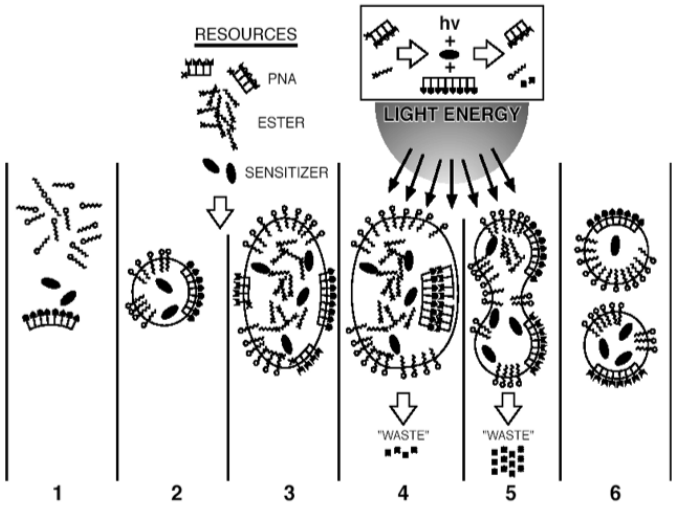

Figure 1.3: Schematic life cycle of the Los Alamos Bug: Components of the protocell spontanously form a micellar container within which the sensitizer resides while the PNA sticks at the surface of the container (1-2). Resources are added to the system and get incorporated into the container (3). The PNA genome acts as a template for supplied dimers to polymerize and replicate the PNA. This process is driven by the sensitizers which use light energy to catalyze hydrolysis (4). Light energy is also used to break the supplied surfactnt precursor into functional surfactant and waste. The container grows as new surfactants are produced (5). Once the container reaches a critical size, it becomes unstable and divides into two daughter cells (6). This completes the life cycle of the protocell.

Current work on the Los Alamos bug includes both experimental and theoretical studies. Among the current protocell research projects, it is maybe one with the most theoretical efford. Mathematical models and computer simulations of this system range from quantum molecular dynamics to mesoscopic simulations and formal chemical kinetics. Beyond the limitations imposed by experimental constraints, an important issue is the likelyhood of finding appropriate parameter domains where stable protocell formation and replication can take place. If dynamical simulations of simple and yet reasonably accurate models of protocell behavior are consistent with a feasible cell division cycle, it will support the expectation of effectively observing such phenomena in the real world. Instead, if such a coupling were shown to be seldom able to trigger replication, it would indicate that an experimental implmentation might fail to work. In this work, the first whole simulation of the Los Alamos bug is presented, providing support for a scenario favoring protocell replication under a generic set of conditions.

Chapter 2

Chemical background

2.1 Properties of water and amphiphiles

The term *amphiphile* is an umbrella term for substances with a special sort of solvability in aqueous systems. If a substance is solvable in water, its individual molecules can disperse freely in the medium to form a homogenous solution. Such substances are called hydrophiles. On the other hand, substances like oil cannot be solved in aqueous mediums and are therefore called hydrophobes: if one adds these substances to water, one can observe the formation of two phases with a sharp phase interface inbetween them.
Whether a molecule is hydrophobic or hydrophilic depends on its charge or charge distribution. Water molecules are dipoles: electrons within the water molecules are attracted by its oxygen atom, making it partially negative charged, while the hydrogen atoms are partially positive charged. As the water molecule is not linear but has a bond angle of approximately 109 degree, the partial charges do not cancel each other out but superpose to a dipole momentum.

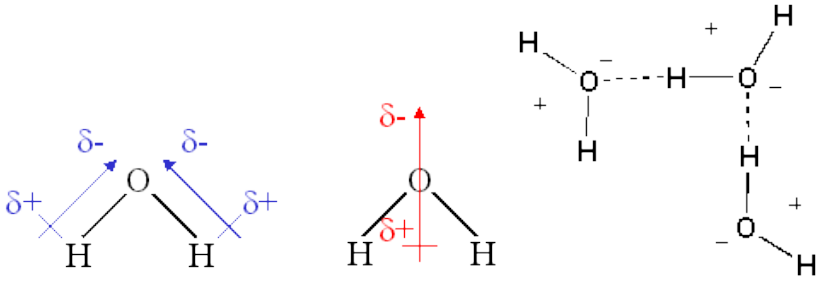

Due to this charge distribution, water molecules interact with each other as well as with other solvents by electrostatic forces: the partially positive charged hydrogen atoms form hydrogen bonds (H-bonds) with the negatively charged oxygen. Unlike the electrostatic field of a point charge, the dipole momenta are strongly directed. Due to this directed force field, a water molecule can interact with four other water molecules: in two of them, it acts as donor, in the other two as acceptor in a hydrogen bond. As a result of these interactions, water molecules form extensive networks in which local interactions can roughly be classified as satisfied (H-O) or frustrated (H-H or O-O), making negative or positive contribution to the global energy.

Ions and polar molecules can interact with the dipolar water. When solved in water, the surrounding solvent molecules arrange according to the (local) charge of the solved molecule. If the solved molecule is positively charged, water molecules arrange with their oxygen side towards the solved particle. Vice versa, if the solved molecule is negatively charged, water molecules arrange with their hydrogen side towards the charge. Uncharged and unpolar molecules cannot interact with water dipoles. The phase separation one can observe in e.g. mixtures of oil and water results from this lack of interactions. The dialectic characterization of substances into hydrophiles and hydrophobes breaks down, however, if one considers molecules, that are composed both of hydrophilic and an hydrophobic parts, usually refered to as head and tail, respectively. These substances are called amphiphiles or surfactants. Amphiphiles form a huge class of chemical substances, differing both in shape and properties of heads and tails. Typical examples of surfactants include fatty acids, long chain alcohols, alcyl sulfates, and amines. Some examples are shown in figure 2.1.

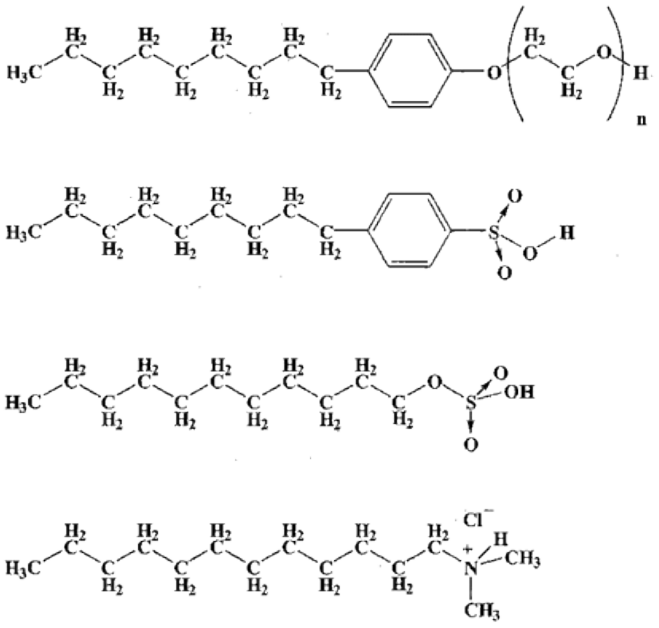

Figure 2.1: Typical examples of surfactant molecules. The hydrophilic head is located on the right side of each molecule.

2.1.1 Aggregation of amphiphiles

If one tries to solve amphiphiles in aqueous mediums, they spontanously form supramolecular aggregates of various shapes. Driving force of this aggregation process is the minimization if free Gibbs energy $G = H - TS$, where H denotes the enthalpy, T the temperature and S the entropy of the system. The entropy is related to the number of possible micro-state that result in the same enthalpy of the system: the higher the number of micro-states, the higher the entropy. Solving a hydrophobic molecule in bulk water introduces possibilities to resolve some frustrations in the water network, reducing the enthalpy of the system. On the same

time, the number of possible micro-states is reduced—i. e. the entropy of the system is reduced. Thus, by minimizing the interface between water and hydrophobic molecules, entropy is maximaizes the number of possible micro-states and therefore the entropy. For the aggregation of amphiphiles, the maximazation of entropy outranges the minimization of enthalpy and can therefore be seen as the driving force of aggregation [20, 21].
Amphiphilic aggregates come in a huge variety of shapes and sizes, depending on the chemical properties and concentration of the amphiphilic molecules, co-solvents, pH value, as well as temperature and pressure. Figure 2.2 shows the most prominent among these aggregates.

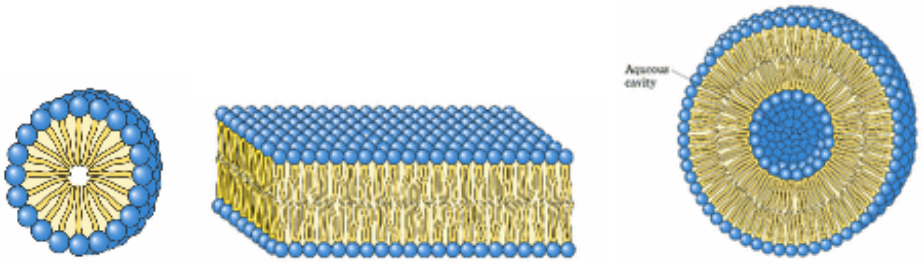

Figure 2.2: Typical amphiphilic aggregates: a) micelles, b) bilayers and c) vesicles

It is important to mention, that these aggregates are dynamic structures: individual molecules diffuse over the surface of the aggregate, and are in constant exchange with monomers in the bulk phase. Amphiphilic aggregates can be best understood as "fluids solved in fluids". This makes them subject to the study of soft condensed matter.

2.1.2 The surfactant parameter

A simple concept to explain the manifold of shapes amphiphilic aggregates can form is the so-called *surfactant parameter* that has been introduced by Israelachvili et al. in the late 1970s [22]. The surfactant parameter—also called *molecular packing parameter*—catches the geometrical shape of an amphiphile in solution. It is defined as

$$N_S = \frac{v}{a_0 l}$$

where v measures the volume of the hydrophobic portion of the molecule, l the length of its hydrocarbon chain, and a_0 the effective area of the hydrophilic head. Therefore N_S relates the volume of the hydrophobic portion to its length normed by the hydrophilic area.
The values of v and l can be easily estimated from the chemical structure of the hydrocarbon chains of the amphiphile. For their estimation, only the number of carbon atoms and the number of methyl groups in the chains have to be known. While v and l are molecular properties, the value of a_0 "is a thermodynamic quantity obtained from equilibrium considerations of minimum free energy and is not a simple variable connected to the geometrical shape and size of the surfactant headgroup" [23]. Thus, it depends on thermodynamic variables like temperature and pressure,

as well as the concentration of surfactants and cosolvents and the pH of the solution. (see [24] p. 15-18 for details).

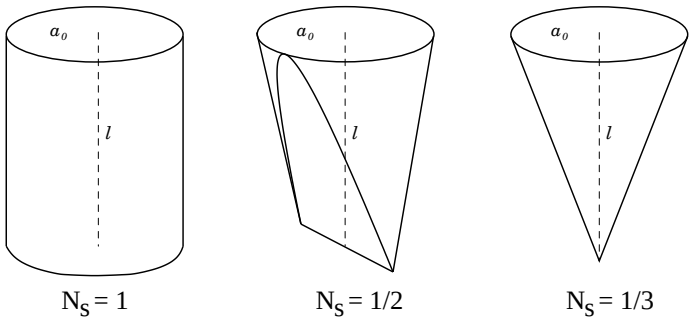

Figure 2.3: Simple geometrical shapes elucidate the relation between a_0, v, l and the surfactant parameter N_S.

The surfactant parameter can help to determine the optimal curvature of the aggregate that will emerge from a given set of amphiphiles. To understand the implications of N_S it is most easy to consider a circular shape of the hydrophilic group (see figure 2.3). Then, if N_S equals to one, the shape of the surfactant will be a cylindar and the favorite shape of the emerging aggregate will be a bilayer. If N_S equals 1/3, the surfactant has the shape of a cone and prefers to form micelles in an aqueous solution. For values between 1/3 and 1, more sophisticate aggregates can be found including cylinders and even scaffolds of interconnected cylinders. If N_S is greater than 1, inverse structures are favored, where the surfactant surrounds and encapsulates parts of the solution. This is especially important if the system is composed of different amphiphiles whose N_S are inverse to each other. In this case, the aggregates will tend to form closed, curved bilayer structures – i. e. small size vesicles.
Because a_0 is a parameter of the system rather than the individual surfactant molecules, N_S—and therefore the shape of amhiphilic aggregates—can vary with thermodynamic variables (temperature, pressure, ...) as well as surfactant concentrations. Figure 2.4 shows a typical phase diagram for a surfactant system.

2.2 Micelles

Micelles are the smallest possible amphiphile assemblies. In these assemblies, the tails of the amphiphiles stick together to form the inside of a closed sphere whose surface is built by the hydrophilic heads of the amphiphile. Micellar structures are preferably formed by fatty acids, alcylsulfates and other surfactants with only one hydrocarbon chain (figure 2.1). Lipids and other amphiphiles with several hydrocarbon chains preferably form layers, as the volume of the hydrophobic chains cannot completely shielded by the head groups.

2.2.1 Size and shape of micelles

Micelles have been experimental analyzed since the 1970s. Although micellar systems are very dynamic, scattering (light scattering, X-ray scattering, a.s.o.) and

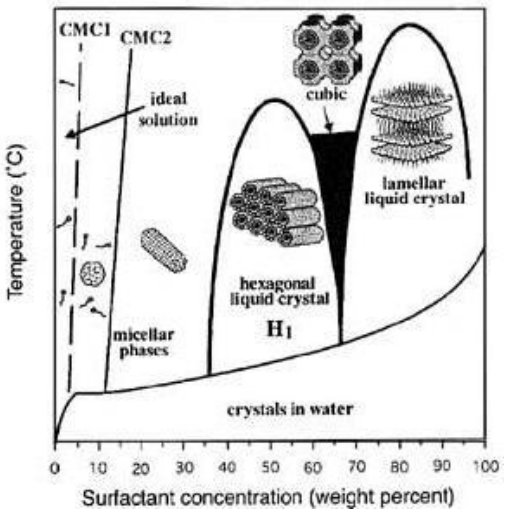

Figure 2.4: Phasediagram of a surfactant solution for constant pressure. By increasing the surfactant concentration, the system undergoes several phase transitions from solved monomers to spherical micelles (CMC), rodlike micelles (CMC2), hexagonal stacked rocks (H1), cubic structures to bilayered lamellar crystal structures (picture from `www.chembio.uoguelph.ca/educmat/chm753/synthesis/physical/evap_self_assembly1.htmlK`).

relaxation experiments (temperature or pressure jumps) could be successfully applied to give insight into the properties of such systems [24]. These experiments showed that there is a sharp transition of the system, when a certain threshold in the concentration of dissolved surfactants is crossed: below this *critical micelle concentration* (CMC) surfactants are mainly solved in bulk phase, whereas above the CMC, the molecules assemble into micelles. Many macroscopic parameters (viscosity, foamabolity, etc.), when plotted against the concentration of dissolved surfactant, exhibit a sudden change when the concentration equals the CMC.
Furthermore, it has been observed that spherical micelles have a characteristic size distribution (see figure 2.5). Micelles have a prefered aggregation number N that denotes the number of constituent amphiphiles (typically between 20 and 100). Micelle size varies around the aggregation number with a standard deviation of σ. Appart from the the assemblies, a micellar system consists of monomers and small submicellar aggregates in bulk phase. The fraction between monomers and micelles depends on the surfactant concentration (as will be seen in section 2.2.2), N and σ, on the other hand, are only little affected by the surfactant concentration. Table 2.1 lists aggregation numbers and CMC for a number of alcylsulfates.

2.2.2 Micellar kinetics

Mathematical models of micellar kinetics have been first introduced in the 1970s [26, 27, 25, 28] by Aniansson and coworkers. They formalized the aggregation process of surfactant monomers in terms of chemical kinetics under the major assumption that surfactant aggregation is a stepwise process that involves only the association and dissociation of single monomers. This assumption leads to the so-called Becker-

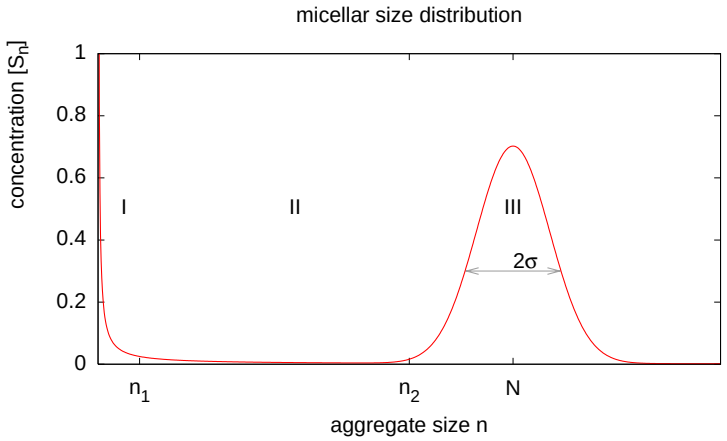

Figure 2.5: Typical size distribution of a surfactant system for concentrations of spherical micelles. Micelles concentrate around a mean aggregation number N with a small standard deviation σ (region III). The system further contains monomers and small submicellar aggregates (dimers, trimers, ...) in bulk phase (region I). In the intermediate region II (with $n_1 < n < n_2$) only very few aggregates are found.

surfactant	N	CMC (M)	k^- (s^{-1})	k^+ $(M^{-1}s^{-1})$
$NaC_6H_{13}SO_4$	17 ± 6	0.42	1.32×10^9	3.2×10^9
$NaC_7H_{15}SO_4$	22 ± 10	0.22	7.3×10^8	3.3×10^9
$NaC_8H_{17}SO_4$	27	0.13	1.0×10^8	7.7×10^9
$NaC_9H_{19}SO_4$	33	6×10^{-2}	1.4×10^8	2.3×10^9
$NaC_{11}H_{23}SO_4$	52	1.6×10^{-2}	4×10^7	2.6×10^9
$NaC_{12}H_{25}SO_4$	64 ± 13	8.2×10^{-3}	1×10^7	1.2×10^9
$NaC_{14}H_{29}SO_4$	80 ± 16.5	2.05×10^{-3}	9.6×10^5	4.7×10^8

Table 2.1: Aggregate number (N), critical micelle concentration (CMC), and association and dissociation rates (k^+, k^-) for sodiumalcylsulfate surfactants with different hydrocarbon chain lengths (from [25] and references therein).

Döring scheme:

$$S_{n-1} + S \underset{k_n^-}{\overset{k_n^+}{\longleftrightarrow}} S_n \quad n \geq 2 \tag{2.1}$$

where S stands for a surfactant monomer and S_{n-1}, S_n for aggregates of size n and $n-1$ respectively.
By relating the equations 2.1 to a heat-transfer and later to a diffusion problem, Aniansson et al. could derive analytical expressions for the fast and slow relaxation times: Under the assumptions that a) $k_n^- = K^-$ and $k_n^+ = k^+$ are independent of n in the region of proper micelles, b) the micellar distribution is a Gaussian with mean N and standard deviation σ, and c) σ is broad enough to replace differences by derivatives, they estimate the fast relation time τ_1 as:

$$\frac{1}{\tau_1} = \frac{k^-}{\sigma^2}\left(1 + \frac{\sigma^2}{N}a\right) \quad \text{with } a = \frac{[S]_T - [S]}{[S]} \tag{2.2}$$

With the additional assumptions that d) the flow of monomers between submicellar aggregates is constant, $J_n = J = constant$ for $n_1 \leq n \leq n_2$, e) fast relaxation is instantaneous compared to slow relaxation, hence $J_n = 0$ for $n < n_1$ or $n > n_2$, and f) the concentration of dimers, trimers and other submicellar aggregates is negligible, $[S_2] = [S_3] = \ldots = [S_{n_1-1}] = 0$, the slow relaxation time can be expressed as

$$\frac{1}{\tau_2} = \frac{N^2}{[S]}\frac{1}{R}\left(1 + \frac{\sigma^2}{n}a\right)^{-1} \quad \text{with } R = \sum_{n=n_1+1}^{n_2} \frac{1}{k_n^- A_n} \tag{2.3}$$

Later, laboratory experiments [29] suggestaed that the Becker-Döring scheme is an oversimplification of the aggregation process: For higher surfactant concentrations, micellar aggregation happens not only by association of monomers but submicellar aggregates also, which effectively increases the speed of micellar aggregation. To account for the fusion of submicellar units, equation 2.1 can be rewritten as a Smoluchowsky scheme

$$S_n + S_m \underset{k_{m,n}^-}{\overset{k_{m,n}^+}{\longleftrightarrow}} S_{m+n} \tag{2.4}$$

which, of course, reduces to the former reaction scheme if $k_{m,n} = 0$ for $m \neq 1$. In 1999, Mailet et al. verified the presence of submicellar fusion in systems of nonyltrimethylammonium and erucyl bishydroxyethylmethylammonium using fully atomistic molecular dynamics simulations [30].
Whichever reaction scheme one might use, the main problem is to identify the reaction rate constants $k_n^{+/-}$ and $k_{m,n}^{+/-}$, which, for mean aggregate numbers up to around 100 add up to 200 and 10.000 values respectively. Due to the small length scale and fast kinetics of micellar systems, it is impossible to measure these rate constants by laboratory experiments.
Although we cannot obtain reliable kinetic constants for equations 2.1 and 2.4, we can gain some insight into the properties of micellar systems by further simplifying these models. Assuming one dominant aggregate number N, we can simplify the kinetics to the *closed association model*, where the system is composed only of monomers S and aggregates S_N of size N. The overall reaction then reads:

$$NS \longleftrightarrow S_N \tag{2.5}$$

with the equilibrium constant

$$K_N = \frac{[S_N]}{[S]^N} \tag{2.6}$$

For the closed association model, the total surfactant concentration is related to the monomer concentration by

$$[S]_T = N[S_N] + [S] = NK_N[S]^N + [S] \tag{2.7}$$

We can use this relation to estimate the fraction of added surfactants that will enter into aggregates, by solving equation 2.7 for $\partial N[S_N]/\partial[S]_T$. Elementary calculus

leads to the ordinary differential equation

$$\begin{aligned}\frac{\partial N[S_N]}{\partial [S]_T} &= \frac{\partial N K_N [S]^N}{\partial [S]_T} \\ &= N^2 K_N [S]^{(N-1)} \frac{\partial [S]}{\partial [S]_T} \\ &= N^2 K_N [S]^{(N-1)} \left(1 - \frac{\partial N[S_N]}{\partial [S]_T}\right) \\ &= \frac{N^2 K_N \left([S]_T - N[S_N]\right)^{(N-1)}}{1 + N^2 K_N \left([S]_T - N[S_N]\right)^{(N-1)}} \end{aligned} \tag{2.8}$$

In the closed association model, the CMC equals the concentration where added surfactant enters an aggregate with the same probability than remaining in the bulk phase; hence:

$$\left.\frac{\partial N[S_N]}{\partial [S]_T}\right|_{CMC} = \left.\frac{\partial [S]}{\partial [S]_T}\right|_{CMC} = 0.5 \tag{2.9}$$

By inserting this in equation 2.8 we obtain the concentration of monomers at the CMC

$$[S]_{CMC} = (N^2 K_N)^{-1/(N-1)} \tag{2.10}$$

We can even express $[S]_{CMC}$ independent of K_N if we substitute $[S]_T = CMC$ in equation 2.7:

$$CMC = [S]_{CMC} + N K_N [S]_{CMC}^N = [S]_{CMC}(1 + N^{-1}) \tag{2.11}$$

It follows that the amount of micellized surfactant at the CMC is

$$N[S_N]_{CMC} = \frac{[S]_{CMC}}{N} = \frac{CMC}{N+1} \tag{2.12}$$

and the concentration of micelles at the CMC is

$$[S_N]_{CMC} = \frac{CMC}{N^2 + N} \tag{2.13}$$

Finally, we can calculate the equilibrium constant K_N combining 2.11 and 2.12:

$$K_N = \frac{1}{N^2 \left(\frac{N\,CMC}{N+1}\right)^{(N-1)}} \tag{2.14}$$

To obtain the fraction of micellized surfactant outside the CMC, we integrated equation 2.8 numerically for the surfactant parameters listed in table 2.1 with the initial condition $N[S_N]_{CMC} = CMC/(N+1)$. Some of the results are shown in figure 2.6 and 2.7. The greater N the more abrupt is the onset of micelle formation above the CMC. For $N \to \infty$ micelle formation becomes a sharp first order phase transition.
From the equilibrium constant we can calculate the free energy change ΔG^0 that accompanies the aggregation process of equation 2.5. In the closed association model, this energy change is N times the energy change of a single monomer, which again can be expressed as a change of the chemical standard potential $\Delta\mu^0$:

$$\Delta G^0 = N \Delta G^0_{mono} = N(\mu^0(micelle) - \mu^0(solvent)) = -RT \ln K_N \tag{2.15}$$

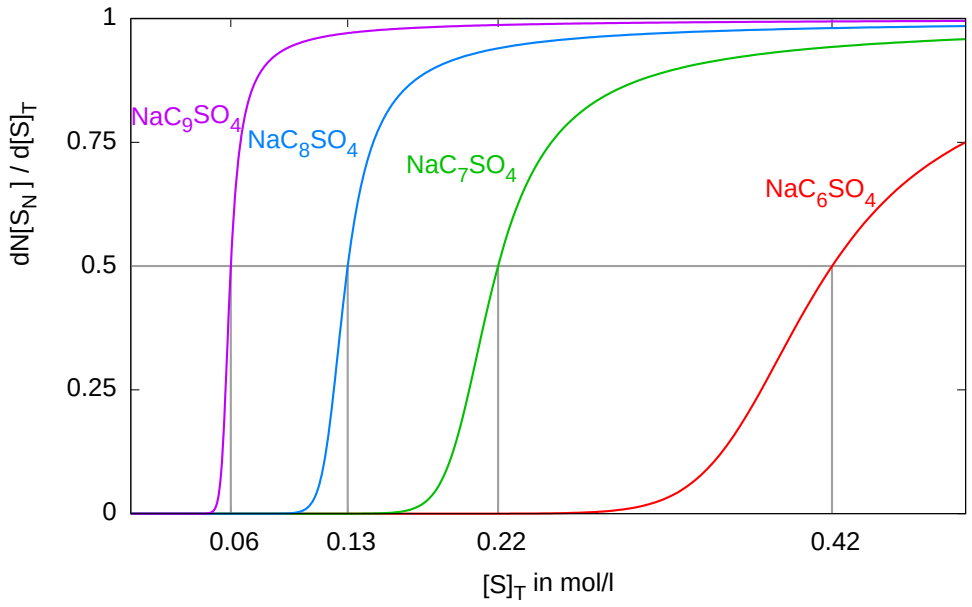

Figure 2.6: Fraction of added surfactant that enters an aggregate against total surfactant concentration $[S]_T$ for some surfactants listed in table 2.1. The greater N, the more abrupt is the onset of micelle formation above the CMC. The CMC is the concentration at which the curves exceed a value of 0.5 (vertical grey lines). For $N \to \infty$ micelle formation becomes a sharp first order phase transition.

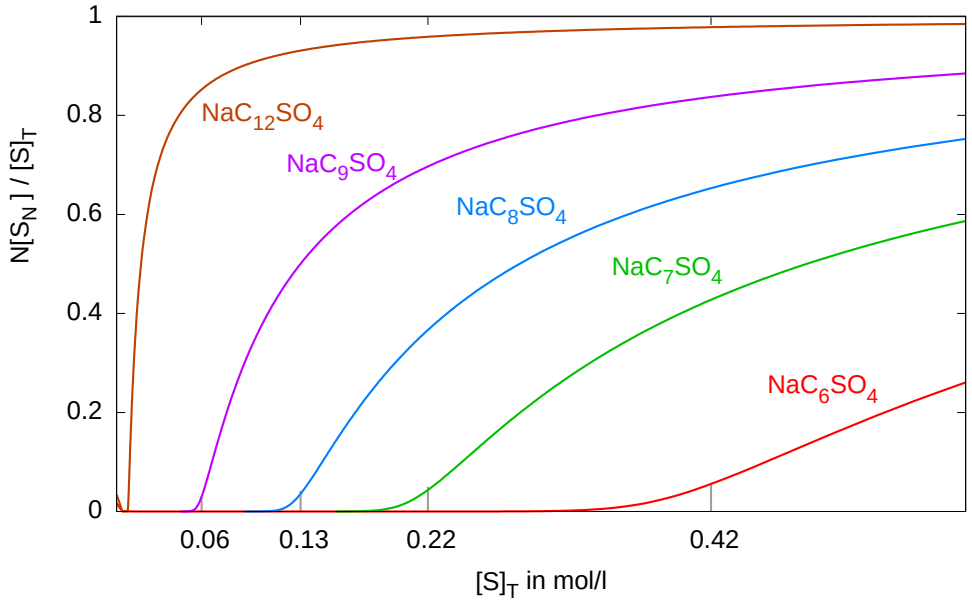

Figure 2.7: Fraction of micellized surfactant $N[S_N]/[S]_T$ against total surfactant $[S]_T$. Vertical lines mark the CMC of the respective surfactants. For greater N the amount of micellzed surfactant increases rapidly with the surfactant concentration. At $[S]_T = 2CMC$, around 50% of the surfactants are micellized, independent of the length of their hydrocarbon tail.

Table 2.2 lists K_N and $\Delta G^0_{mono}/RT$ for the surfactants observed. As expected, the longer the hydrocarbon chain of the surfactant, the bigger is the free energy gained by micellization.

surfactant	N	CMC (in M)	K_N	$\Delta G^0_{mono}(in\mathrm{RT})$
$NaC_6H_{13}SO_4$	17	0.42	9.21×10^3	-0.5369
$NaC_7H_{15}SO_4$	22	0.22	3.39×10^{11}	-1.2067
$NaC_8H_{17}SO_4$	27	0.13	3.85×10^{20}	-1.7555
$NaC_9H_{19}SO_4$	33	6×10^{-2}	3.00×10^{36}	-2.5452
$NaC_{11}H_{23}SO_4$	52	1.6×10^{-2}	3.80×10^{88}	-3.9224
$NaC_{12}H_{25}SO_4$	64	8.2×10^{-3}	1.74×10^{128}	-4.6139
$NaC_{14}H_{29}SO_4$	80	2.05×10^{-3}	9.81×10^{208}	-6.0153

Table 2.2: Equilibrium constants K_N for the surfactants of table 2.1 calculated with the closed association model. See text or details.

It is worth mentioning that the described mathematical models of micellar kinetics assume the system to be in its equilibrium state. There is no closed theory for micellar systems far away from their equilibrium state. Our systems of interest, however, are far from equilibrium due to ongoing chemical reactions. Thus, more detailed models are needed to successfully analyse them. The model of our choice is introduced in chapter 3.2. However intricate this model and its predicted dynamics might be, it should allow to obtain the above results when applied to an equilibrium system.

Chapter 3

Dissipative Particle Dynamics

The dynamics of micellar systems occur in physical length and time scales, that make their treatment by computer simulation extremely intricate. Ideally, one might wish to model such systems in their fully atomistic detail. For such an approach, molecular dynamics (MD) would be the tool of choice, where the position and momentum of every single atom in the system is tracked through time. However, despite the overwhelming increase of computer performance, MD is still restricted to several orders of magnitude below both length and time scale of interest. On the other hand, the number of constituent molecules of micellar systems is too small to allow for continuum descriptions based on partial differential equations, like e.g. density field theory. This makes it necessary to analyze micellar kinetics with mesoscale simulation techniques, which intend to bridge the gap between atomistic and continuum descriptions.

3.1 Coarse graining Molecular Dynamics

The general idea behind mesoscopic simulation methods is to somehow coarse grain the original atomistic approach. This is possible because the dynamics of MD simulations can be decomposed into fast and slow types of motion: the fastest degrees of motion in classical (non-quantum) MD simulations are the vibrational fluctuations of covalent bonds, which act on the order of femtoseconds – several orders of magnitude below rotational and translational degrees of freedom [31]. We can think of the potential energy landscape of a typical MD simulation as a slowly decreasing path (slow manifold) at the bottom of a steep valey (fast manifolds). However, most properties of mesoscopic systems are relatively unaffected by the underlying fast degrees of freedom. Mesoscopic simulation techniques intent to catch the motion along the slow manifold while effectively averaging along the fast manifold, leading to a much greater time step. A consequence of the time coarsing is, that the spatial resolution of of the method decreases (as space and time are related by particle velocities), which leads to an effective spatial coarse graining. Instead of individual atoms, mesoscopic simulation methods deal with clusters of atoms or even molecules: beads of a polymer strand or a “lump” of water.
A variety of mesoscopic methods has been established, each one having its own strengths and limitations. Basically, there are two strategies to simplify the details

of a fully atomistic model: one is to move from the continuos physical space to an approximating lattice and to build an automaton that mimicks the particle motion within that simplified space. The most prominent models in this category are possibly Lattice Gas (LGA) and Lattice Boltzmann automata (LBA) [32, 33, 34]. The second approach —coarse grained MD—preserves the continuity of space. However, unlike MD, coarse grained methods assume an underlying medium which aggeregates degrees of freedom on the micrscale. Particles interact with this medium according to the Ginzberg-Landau equation

$$\frac{d^2\mathbf{r}_i}{dt^2} = -\nabla\phi_i - \mu\mathbf{v}_i + \xi_i \tag{3.1}$$

where $\mathbf{r}_i, \mathbf{v}_i$ denote the position and velocity of particle i, μ models the viscous damping and the random variable ξ the Brownian motion of the fluid. Several modeling techniques have been based on equation 3.1. The most prominent among them are Brownian and Stokesian Dynamics.

Dissipative particle dynamics (DPD) is a coarsed graind MD method for fluids based on equation 3.1. It has been invented 1992 by Hoogerbrugge and Koelmann [35]. Since its invention, DPD has received various theoretical support [36, 37, 38, 39, 40, 41, 42, 43]. The method has been proved to successfully describe thermodynamic systems [36]. Furthermore, it has been shown that DPD is an approximation of the Navier-Stokes equation of hydrodynamic motion [35]. Thus, it conserves flow properties of the modeled physical system. In this sense, DPD is a real mesoscale simulation technique, that links both to the atomistic scale of MD simulations, as well as to continuum descriptions of fluids.

The DPD method used throughout this work is the revisited DPD version by Groot and Warren [38]. This variant has become the *de facto* standard for DPD applications over the last decade.

3.2 The DPD Formalism

A DPD simulation consists of a set of N particles located in either two or three-dimensional continuous space with Euclidean metrics. Each particle i has a position $\mathbf{r}_i$, mass m_i and momentum $\mathbf{q}_i$, from which one can derive its velociy $\mathbf{v}_i = \mathbf{q}_i/m_i$. Its motion is determined by a force field $\mathbf{F}_i$ through Newton's third law of motion:

$$\frac{d^2\mathbf{r}_i}{dt^2}(t) = \frac{1}{m_i}\mathbf{F}_i(t) \tag{3.2}$$

The force acting on particle i can be decomposed into pairwise interactions, which respectively are the sum of of three different components – a conservative, a dissipative and a random one:

$$\mathbf{F}_i = \sum_{j\neq i}\mathbf{F}_{ij} = \sum_{j\neq i}\mathbf{F}_{ij}^C + \mathbf{F}_{ij}^D + \mathbf{F}_{ij}^R \tag{3.3}$$

where $\mathbf{F}^C$, $\mathbf{F}^D$ and $\mathbf{F}^R$ are defined by

$$\mathbf{F}_{ij}^C = -\nabla\phi_{ij} \tag{3.4}$$
$$\mathbf{F}_{ij}^D = -\eta\omega^D(r_{ij})\left\langle \mathbf{n}_{ij}, \mathbf{v}_{ij}\right\rangle \mathbf{n}_{ij} \tag{3.5}$$
$$\mathbf{F}_{ij}^R = \sigma\omega^R(r_{ij})\xi_{ij}\mathbf{n}_{ij} \tag{3.6}$$

For each particle pair (i,j) $\mathbf{r}_{ij} = \mathbf{r}_i - \mathbf{r}_j$ is the relative position, $r_{ij} = |\mathbf{r}_{ij}|$ the distance and $\mathbf{v}_{ij} = \mathbf{v}_i - \mathbf{v}_j$ the relative velocity. We denote with $\mathbf{n}_{ij} = \mathbf{r}_{ij}/r_{ij}$ the (unit) direction between the two particles. $\langle\cdot,\cdot\rangle$ denotes the standard scalar product. The conservative force $\mathbf{F}_{ij}^C$ can be defined in the usual way as the negative gradient of a potential $\phi_{ij} = \phi(r_{ij})$. The general DPD formalism does not specify the exact form of ϕ_{ij}, but only states that it should be mostly repulsive. We discuss the choice of ϕ_{ij} in more detail in section 3.3. Here, we only want to state that almost all DPD models dicussed in the literature use a potential of the form

$$\phi(r) = \begin{cases} \frac{a_{ij}r_c}{2}(1-\frac{r}{r_c})^2 & \text{if } r < r_c \\ 0 & \text{otherwise} \end{cases} \tag{3.7}$$

whereby a_{ij} and r_c are constants that define the strength and range of the particle interaction. The resulting repulsion force decreases linearly with particle distance.
The dissipative force $\mathbf{F}_{ij}^D$ is a function of the relative velocity of the two particles. It models the viscous damping of the fluid. The friction coefficient η scales the strength of this force and ω^D is a distance weighing function not determined by the general formalism, that will be specified later. The dissipative force introduces a flow of energy from the explicit modeled mesoscale to the underlying microscale: The friction of the fluid successively breaks down particle flows into less and less ordered motion. In a real fluid, this would lead to local heating (Brownian motion). But as motion on the atomistic scale has been taken out of the model, energy is simply removed from the system.
The random force, $\mathbf{F}_{ij}^R$ accounts for thermal effects. It counteracts the dissipative force by introducing an energy flow from the atomistic scale back into the mesoscale. It is scaled by a strength parameter σ and a second weighing function ω^R. ξ_{ij} is a Gaussian distributed random variable with zero mean and unit deviation.
In order to reproduce the right thermodynamic behavior, the DPD formalism must satisfy the fluctuation dissipation theorem, which states that a fluctuation (perturbation) in the system will be dissipated as the system returns to its well-defined equilibrium, and that this dissipative relaxation is proportional to the fluctuation. As a consequence, the equilibrium state will obey Maxwell-Boltzmann statistics and therefore allows the derivation of thermodynamic properties. As shown by Español and Warren [36], DPD satisfies the fluctuation dissipation theorem if and only if the weighing functions ω^D and ω^R satisfy the relation

$$\omega^D = (\omega^R)^2 \tag{3.8}$$

For historical reasons, as well as with respect to the conservative forces in DPD, most authors set

$$\omega^D(r) = (\omega^R(r))^2 = \left[2(1-\frac{r}{r_c})\right]^2 \tag{3.9}$$

If relation 3.8 is fulfilled, $\mathbf{F}_{ij}^D + \mathbf{F}_{ij}^R$ acts like a thermostat to regulate the temperature of the sytem. The equilibrium temperature k_bT is then given by

$$k_bT = \frac{\sigma^2}{2\eta} \tag{3.10}$$

where k_b denotes the Boltzmann constant $1.38 \cdot 10^{18} JK^{-1}$. Due to the finite size of the system, the measured temperature will fluctuate around this equilibrium expectation value. In MD simulations, a variety of thermostats has been explored but only the DPD-thermostat is guaranteed to conserve momenta of the particles, and thus flow properties of the fluid. It is therefore the only thermostat that allows the study of transport processes (see [43]).
For the study of polymer and amphiphile solutions, it is common to introduce bonding forces into the model. A bond between particles i and j is formalized by an additional harmonic spring force, such that

$$\mathbf{F}_{ij}^S(\mathbf{r}) = \begin{cases} b(1 - \mathbf{r}/r_b) & \text{if } (i,j) \text{ are bonded} \\ 0 & \text{otherwise} \end{cases} \tag{3.11}$$

with strength b and range r_b, respectively. The overall force between particle i and j then becomes

$$\mathbf{F}_{ij} = \mathbf{F}_{ij}^C + \mathbf{F}_{ij}^D + \mathbf{F}_{ij}^R + \mathbf{F}_{ij}^S \tag{3.12}$$

It should be noted, that all involved forces are central ($\mathbf{F}_{ij} = -\mathbf{F}_{ji}$), parallel to the relative position, and conserve linear and angular momenta but not energy. As the forces depend only on relative particle positions and velocities, the model is transrotational invariant (Galilean invariant).

3.3 Soft Core Potential Functions

In almost all DPD publications, the interaction forces $\mathbf{F}^C$ and $\mathbf{F}^S$ are linear relations of the form $\mathbf{F}(\mathbf{r}) = a(1 - \mathbf{r}/r_c)$. They appear as the derivates of a soft core potential function

$$\phi(r) = \begin{cases} \frac{ar_c}{2}\left(1 - \frac{r}{r_c}\right)^2 & \text{if } r < r_c \\ 0 & \text{otherwise} \end{cases} \tag{3.13}$$

(The term "soft core" refers to the elastic properties of the interacting particles. On the other hand, potentials with a singularity at 0 are called "hard core" potentials) The choice for this particular interaction potential is seldom discussed in the DPD literature, and seems to be mainly based on heuristic reasoning: ϕ is the most simple short range potential that is finite and exhibits a continuous force (even at the cutoff distance). Both short range and finiteness have great computational advantages: a short range potential drastically reduces the particle interactions that need to be taken into account, while finiteness allows to increase the numerical step width.
Disregarding the atomistic details, ϕ can be conceptually understood as a penalty for the deviation from a regular equilibrium distribution. Even the far more detailed approach of MD uses such simple "penalty potentials" for modelling covalent bonds (equation 3.11), despite its obvious physical inaccuracy: the harmonic potential

increases without bounds with distance. Hence, it does not account for the formation or bond dissociation. Instead, it only seeks to reflect the energy difference of small deviations from the equilibrium value. According to the DPD philosophy, it is straightforward to transfer this argument also to the interparticle potentials.
However, if DPD aims to be a concise mesoscale method, that can successfully link up to an atomistic description, we need a more rigorous foundation of this potential function. One method to derive a soft core potential from underlying atomistic potentials is given by Forrest and Suter [44] and shall be discussed here in some detail.
In molecular dynamics, non-bonded (and non-charged) interactions are usually modeled by the so-called Lennard-Jones potential:

$$\phi_{LJ}(r) = 4\epsilon \left(\left(\frac{\sigma}{r}\right)^{12} - \left(\frac{\sigma}{r}\right)^{6} \right) \tag{3.14}$$

In this equation, r^{-12} models the strong repulsion resulting from overlying electron clouds due to the Pauli exclusion principle, while $-r^{-6}$ describes the attraction between two atoms due to induced dipole interactions (so called van-der-Waals forces). At the van-der-Waals radius $r^* = 2^{\frac{1}{6}}\sigma$ the potential exhibits a minimum. It is interesting to mention, that even the Lennard-Jones potential cannot be plainly derived from theory: only the attractive part of equation 3.14 can be found as one term in a multipole expansion of an assumed underlying electron distribution (see e.g. [24]). The repulsive term, however, is a pure *ad hoc*-expression that has no quantumphysical explanation.

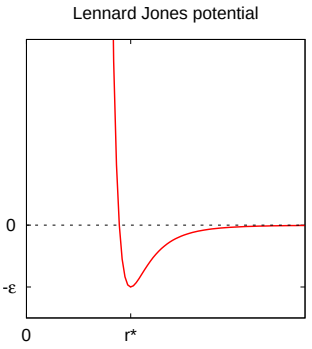

Based on the assumption that the effective mesoscopic motion is relatively unaffected from fast atomistic motion, Forrest and Suter use a time coarse-graining procedure to preaverage the fast degrees of freedom: At each time $t_0 + t$, $t_0 = kt_{av}$, the actual particle position $r_i(t_0 + t)$, $i = 1, \ldots, N$, is given by the mean position $R_i(t_0)$ and a random deviation $\Delta_i(t)$ on the smaller scale:

$$r_i(t_0 + t) = R_i(t_0) + \Delta_i(t) \quad \text{for } t \leq t_{av} \tag{3.15}$$

Forrest and Suter perform atomistic MD and hybrid Monte Carlo simulations to obtain a set of R_i's and Δ_i's for polymer solutions. The potential energy U of the system can be decomposed into bonded and non-bonded (Lennard-Jones) contributions:

$$\begin{aligned} U(\{R_i + \Delta_i\}) &= U_{nb}(\{R_i + \Delta_i\}) + U_b(\{R_i + |Delta_i\}) \\ &\approx U_{nb}(\{R_i + \Delta_i\}) + U_b(\{R_i\}) \end{aligned} \tag{3.16}$$

For a canonical ensemble, the system states $\{r_i(t)\}$ follow a Bolzmann distribution $p_B(\{r_i(t)\}) \propto e^{-1/k_b T U\{r_(t)\}}$.
The aim is now to derive an expression for an effective non-bonded potential energy U_{nb}^{eff} that reveales the $R_i(t_0)$ without knowing the intermediate states at times $t_0 +$

t. The bonding potential U_b can later be added again, to obtain a total effective potential $U^{\mathit{eff}} = U_{nb}^{\mathit{eff}} + U_b$. Forrest and Suter define U_{nb}^{eff} as an observable of the system. Assuming an ergodic sampling of the system, U_{nb}^{eff} can be averaged over a time interval $n_t \Delta t$ (where n_t denotes the number of measurements) according to

$$\left\langle U_{nb}^{\mathit{eff}} \right\rangle = \frac{1}{n_t} \sum_{k=1}^{n_t} U_{nb}^{\mathit{eff}}(\{r_i(k\Delta t)\}) \tag{3.17}$$

Here, $t = n_t \Delta t$ is considered as the time scale of the atomistic scale. Using expression 3.15, we can decompose this sumation into successive blocks of length $\tau = t_{av}/\Delta t$.

$$\left\langle U_{nb}^{\mathit{eff}} \right\rangle = \frac{1}{n_t/\tau} \sum_{k=1}^{n_t/\tau} \frac{1}{\tau} \sum_{l=0}^{\tau-1} U_{nb}^{\mathit{eff}}(\{R_i(k\tau\Delta t) + \Delta_i(l\Delta t)\}) \tag{3.18}$$

With the assumption that Δ-fluctuations have a distribution $p_\Delta(\{\Delta_i\})$ independent of the particle position $\{R_i\}$, one can follow that

$$\begin{aligned} \left\langle U_{nb}^{\mathit{eff}} \right\rangle \quad \propto \quad & \int \left[\prod_{i=1}^{N} d^{(3)} R_i \right] \int \left[\prod_{i=1}^{N} d^{(3)} \Delta_i \right] U_{nb}^{\mathit{eff}}(\{R_i + \Delta_i\}) \\ & \times p_\Delta(\{\Delta_i\}) e^{-\frac{1}{k_b T} U(\{R_i + \Delta_i\})} \end{aligned} \tag{3.19}$$

Forrest and Suter finally derive U_{nb}^{eff} as

$$\begin{aligned} U_{nb}^{\mathit{eff}}(\{R_i\}) \quad = \quad & -k_b T \ln \int \left[\prod_{i=1}^{N} d^{(3)} \Delta_i (2\pi \left\langle \Delta^2 \right\rangle)^{-3/2} \times e^{\frac{-\Delta_i^2}{2\left\langle \Delta_i^2 \right\rangle}} \right] \\ & \times e^{-\frac{1}{k_b T} U_{nb}(\{R_i + \Delta_i\})} \end{aligned} \tag{3.20}$$

We can see, that each of the mean ("block") configurations $\{R_i\}$ appears with the probability density $p_{eff}(\{R_i\}) \propto e^{1/k_b T U_{eff}(\{R_i\})}$. The fast degrees of motion Δ_i are completely rallied in the integral. We therefore have effectively preaveraged over the fast Δ-fluctuations. U_{nb}^{eff} gives the energy of the whole system configuration $\{R_i\}$. However, one can decompose the effective potential into pairwise superpositions of radial potentials: $U_{eff}(R_i) = \sum_{j=1}^{N} V_{eff}(R_i - R_j)$. To see how this can be achieved, consult the original work by Forrest and Suter [44].

Unfortunately, the integral in equation 3.20 is not analytically solvable. Forrest and Suter nummerically integrated U_{nb}^{eff} for different time averages t_{av}. Doing so, they could show, that U_{nb}^{eff} is indistiguishable from the soft-core potential, when t_{av} and thus $\langle \Delta^2 \rangle^{1/2}$ is sufficiently large ($\langle \Delta^2 \rangle^{1/2} = 2$Å). See figure 3.1 for a comparision.

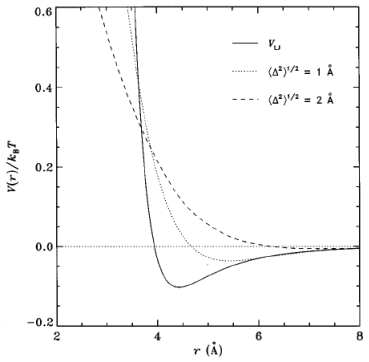

Figure 3.1: Lennard-Jones potential and effective potentials for coarse-graining factors $\langle \Delta^2 \rangle^{1/2} = 1$Åand $\langle \Delta^2 \rangle^{1/2} = 1$Å.

3.4 Thermodynamic properties in DPD

To deepen the understanding of the method, we want to discuss shortly some thermodynamic properties of DPD.
It has already been discussed, how the temperature is regulated by the thermostat $\mathbf{F}^D + \mathbf{F}^R$, and that the equilibrium temperature is given by $k_b T = \sigma^2/2\eta$. As particle number and volume are constant we operate in the NVT ensemble. The pressure of the system configuration can be obtained from the virial expression [45]:

$$p = \rho k_b T + \frac{1}{3V} \left\langle \sum_{i<j} (\mathbf{r}_i - \mathbf{r}_j) \mathbf{F}_{ij}^C \right\rangle \tag{3.21}$$

where the brackets denote the average over all particles. Groot and Warren measured p for various densities ρ and could obtain the equation of state, that is p as a function of ρ as

$$p = \rho k_b T + \alpha a \rho^2 \quad \text{where } a = 0.101 \pm 0.001 \tag{3.22}$$

The approximation is reliable for densities $\rho > 2$. If one wants to run simulations in a NPT ensemble—i. e. the pressure is constant instead of the volume—one can turn the system size V into a dynamic variable. By doing so, Trofimov developed a DPD barostat to dynamically adjust the pressure of the system [43].
From section 3.3, it has become apparent that the potential energy ϕ must not be understood as a "mechanical" potential like the one used in MD, where the potential describes the internal energy U of the system. Rather, the DPD potential is derived from the mesoscopic motion of the system. It catches the driving force of the motion, which is the minimization of free energy. Apart from this heuristical argument, Pagonabarraga and Frenkel derive the DPD potential from a generic expression of the free energy [40]. For the NVT ensemble, ϕ therefore expresses the Helmholtz free energy $A = U - TS$, where T is the temperature and S the entropy of the system. The Helmholtz energy is related to the Gibbs energy by

$$G = A + pV = U + pV - TS \tag{3.23}$$

It is elucidatve to mention that the Gibbs free energy is related to the chemical potential μ^0 of the constituents of the system by $G = \sum_i \mu_i^0$ [45].
For the processes, we are interested in, volume and pressure changes are excepted to be negligible small, thus

$$G = \sum_i \mu_i^0 \approx \sum_{i=1, i<j}^{N} \phi_{ij} = A \tag{3.24}$$

This is very convinient, as ΔG is the main thermodynamic variable accessible by experiments. Experimental observables can be directly used for the simulation, and there is no need to explicitely cope with entropy in our simulation (as needs to be done when operating with the enthalpy of the system).

3.5 Incorporation of chemical reactions

We extended the DPD formalism to account for chemical reactions. The way chemical reactions are implemented in our model is taken from a publication by Naoki Ono [46], where Brownian Dynamics is extended with the same algorithm.

Chemical reactions occur between two reactants and fall into three different classes:

$$\begin{aligned} \text{Synthesis: } & \mathbf{A} + \mathbf{B} \longrightarrow \mathbf{X} - \mathbf{Y} \\ \text{Analysis: } & \mathbf{A} - \mathbf{B} \longrightarrow \mathbf{X} + \mathbf{Y} \\ \text{Configuration change: } & \mathbf{A} - \mathbf{B} \longrightarrow \mathbf{X} - \mathbf{Y} \end{aligned}$$

Each reaction has a given rate for spontaneous occurance k_s.

The spontaneous reaction rate can be enhanced by the presence of nearby catalysts. The catalytic effect linearly decreases with the distance to the reactant. For simplicity, the effect of several catalysts is modeled as a linear superposition. Thus, the overall reaction rate is given as

$$k = k_s + \sum_{\mathbf{C}} k_{cat} \left(1 - \frac{r(\mathbf{C})}{r_{cat}}\right) \tag{3.25}$$

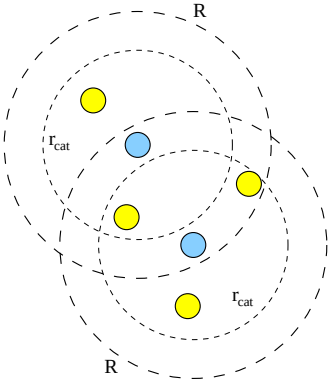

Figure 3.2: Catalytic influence on a synthesis. Reactants are shown in blue, catalysts in yellow. See text for details.

Syntheses have the further restriction, that the distance of the reactants must be less than a maximal reaction range R in order for them to occur.

When obtaining probabilities from these reaction rates, one focuses the problem that reactions are not always independent events. Consider three reactants that are close enough to each other to take place. Despite the equal reaction rates, only one of the two to three possible reations can actually be realized. The rigorous way to solve this problem would be the construction of a master equation where probabilities are given for every possible state transition of the whole system [47]. However, as our system can hold up to hundreds of reactants, such an approach becomes practically unfeasible, simply because of the enormous number of possible state transitions. To determine which reactions take place, we therefore use the agent-based like algorithm introduced by N. Ono [46].

For every reaction scheme, we successively check all possible pairs of reactants $\mathbf{A}, \mathbf{B}$, and compare their effective reaction rate k to a number taken from a pseuorandomnumber generator. If the reaction rate is smaller than this number, we perform the reaction and go on to the next pair of reactants. **A** and **B**, however, will not be considered again in this step. The exact algorithm—notated in the `python` programming language—reads like this:

```
shuffle(reaction_list)
for reaction in reaction_list :
    for A in space.particles(reaction.educt_A) :

        if reaction.is_synthesis :
            # if reaction is a synthesis, possible reaction partners
            # are particles of type educt_B in the vicinity of A.
            partners = A.neighbors(reaction.educt_B,reaction.R)
        else :
            # otherwise, possible reaction partners are particles
            # of type educt_B bonded to A.
            partners = A.bonded(reaction.educt_B)

        for B in partners :
            # compute effective reaction rate
            k = reaction.k
            for C in A.neighbors(reaction.catalyst,reaction.r_cat) :
                k += reaction.k_cat *
                    ( 1 - (A.pos-C.pos).length()/reaction.r_cat )

            if random() < dt * k :
                # perform reaction
                react(A,B,reaction)
                # and leave inner for loop
                continue
```

If a reaction occurs, we change the particle types of the educts $\mathbf{A} \rightarrow \mathbf{X}$, $\mathbf{B} \rightarrow \mathbf{Y}$ and establish or remove a bond between the products, depending on the type of reaction. Particle positions and momenta are conserved.
We also introduced particle exchange into the model to mimick the support of chemicals into the system which drive it out of its equilibrium. Within a given region, particles of a certain class can be exchanged with a given probability. Likewise chemical reactions, we conserve positions and momenta when exchanging particles.

3.6 Applications and limitations of DPD

DPD has been introduced by Hoogerbrugge and Koelman to model the rheology of suspensions (e.g. cement, clay) [35, 48]. To catch the geometry of suspended mesoparticles they connect some DPD beads by rigid bonds. The DPD method can than be applied to analyse flow properties of these complex fluids under various constraints like compression or shear forces [49, 50].
The method has later been used to model block polymers [51, 52]. Polymers are introduced into DPD by connecting several beads by elastic spring forces (as described above). To account for the relative immiscibility of different sections of a block polymer, repulsion parameters between representing DPD beads are varied. One can then observe phase seperation of the immiscible polymer sections and analyze domain formation as an interplay of entropy maximaztion and enthalpie minimazation.
Using the same bead-spring representation, DPD has been applied to phospholipid bilayers that form the basis of biological membranes. Spontenous formation of mem-

branes within a mixture of lipids and solvents has been investigated by Venturoli and Smit [53]. Groot and Rabone used DPD to model surface tension, damage and rupture of model membranes [54]. Yamamoto et al. observed a spontenous bilayer to vesicle transition [55] and later used the method to analyse domain formation for mixed lipid vesicles [13]. Depending on the ratio of lipids on the outer and inner membran, they could induce budding and fission of the membrane.
Only very little efford has been done to model micelles with DPD. To our knowledge, only two publications of R. D. Groot cover the specific issues of micellar systems [56, 57]. However, this work focuses on the interplay between micelles and polymers. Because of the different involved length scales, surfactants are modeled by a very simplistic representation and certain features of micellar systems, namely the characteristic size distribution cannot be observed using Groots parameter set.
It is also known, that DPD cannot model certain phenomena found in real fluidic systems. First, turbulent flows are outside the scope of this method. Turbulence involves all scales of the system. By modelling microscopic motion implicitly through the DPD thermostat, we loose the ability to model such motion. Until today, there is no mesoscale method that can achieve turbulence. Thus, all DPD simulations will be limited to laminar flows.
Second, it is known that the simple repulsion potential commonly used in DPD simulations cannot predict phase separation phenomena like the coexistence of liquid and vapour phases: in a pure aqueous system, particles will spread more or less homogeneously throughout the space without any significant density variation. In a real system, however, we expect water to occupy only a certain portion of the space – preserving a certain pressure – while the remainder of the space is filled with vapour. Frenkel and Pagonabarraga developed a modification of the standard DPD algorithm, called many-body DPD or MDPD, that allows to model such phase separations [40]. The method has further been investigated by Trofimov et al. [42]. Their variant of the method essentially introduces attractive forces between the particles, thus mimicking the long tail of the Lennard-Jones potential. To counterpart this attraction, they use a repulsion that depends on the local density of each interacting particle pair. It can be shown, that this density dependent potential is equivalent to many-body interaction potentials, hence the name of the method. MDPD has been used successfully to model interface phenomena like those occuring in a pending droplet [58].

Chapter 4

Results

4.1 Pure aqueous system

To gain confidence into our implementation of the DPD model, we started with simulations of a pure aqueous system. Simulations have been run in a box of size $10 \times 10 \times 10 r_c^3$. Here and throughout the following experiments, we used the standard DPD parameters for the friction constant $\nu = 4.5$, noise-level $\sigma = 3.0$ (hence $k_b T = 1$), mass $m = 1$, cutoff-distance $r_c = 1$, water water repulsion $25 k_b T$, and water density $\rho = 3 r_c^{-3}$, unless otherwise noted.

4.1.1 Validation

To get an estimate of the quality of our numerical solver, we measured total momentum and energy drift of a conservative system, and total momentum and temperature deviation of a dissipative system.
As mentioned before, all forces in the DPD formalism are central, thus the total momentum $q = \sum_i |m_i v_i|$ should be conserved. Due to numerical noise, momentum conservation cannot hold exactly. This could violate the hydrodynamic consistancy of the simulation. A good algorithm should therefore yield only small fluctuations in the total momentum.
If η and σ are set to 0, the force field reduces to the conservative force $\mathbf{F}^C$ and the total energy should be constant. Although the eventual loss or gain of energy due to numerical inaccuracies would be corrected, once the dissipative forces are reintroduced, a good algorithm should still hold in the conservative regime. The usual way to quantify erroneous energy flucuations in MD simulations is to calculate the energy drift

$$\Delta E(t) = \frac{E(t) - E(0)}{E(0)} \tag{4.1}$$

where E is the sum of potential energy $E_{pot} = \frac{1}{2} \sum_{i,j} \phi(r_{ij})$ and kinetic energy $E_{kin} = \frac{1}{2} \sum_i m_i v_i^2$ at time t. A good numerical solver should yield a small energy drift without significant trend.
An analogy to the energy drift for the dissipative regime is the temperature error

$$\Delta T = \frac{|T_{tunde} - T_{measured}|}{T_{tuned}} \tag{4.2}$$

whereby T_{tuned} is given by relation 3.10 and

$$T_{measured} = \frac{2}{n} E_{kin} \tag{4.3}$$

with n specifying the number of degrees of freedom (number of particles multiplied by the dimension of particle space).

Conservative system

Figure 4.1 shows the time evolution of total momentum and energy drift for a system intialized with total momentum $0 r_c/\tau$, total energy $23731.930 k_T$ and random particle positions. The system has been iterated for $0\tau \leq t \leq 80\tau$ with stepwidth $\Delta t = 0.04\tau$ (2000 iterations). As one can see, the algorithm accumulates energy, but not momenta.
The total momentum fluctuates between 0 and $7 \times 10^{-13} r_c/\tau$ (average is $2.558 \times 10^{-13} r_c/\tau$), which is considerably small compared to the average momentum per particle ($2.161 r_c/\tau$) and is thus considered a minor artefact.
The energy drift increases almost linear from -0.75% to 2% over 2000 iterations – thus, during a longer run, the conservative system gets heated. We could recude the energy growth by decreasing the timestep. However, the timestep is one of the limiting factors for the accessible simulated timespan. Furthermore, with the introduction of the DPD thermostat for all following simulations, the energy surplus is regulated anyway. Compared with the Euler integrator, that was the original algorithm in DPD simulations [35, 48], the performance of our algorithm is actually quite promissing: in our simulation, the energy increases linear with $6.749 k_b T/\tau$, while the use of an Euler integrator with the same stepwidth leads to an exponential increase with a doubling time around 2.5τ – after only 11 iterations, the energy drift reaches 100%. Thus, we also consider the energy drift in our simulation as a minor artefact.

Dissipative system

For the dissipative system, we made simulation runs with a varying stepwidth Δt between 0.02τ and 0.06τ from $t = 0\tau$ until $t = 80\tau$. 0τ to 5τ has been considered as the transient time, and was therefore not taken into account for the analysis.
For $\Delta t = 0.04\tau$, total momentum of the dissipative simulation varied between $1.5 \times 10^{-14} r_c/\tau$ and $5.5 \times 10^{-13} r_c/\tau$ ($2.386 \times 10^{-13} r_c/\tau$ on the average). Thus, no additional numerical fluctuations are introduced by $\mathbf{F}^D + \mathbf{F}^R$. We also found, that the step width Δt has no significant influence on the magnitude of numerical fluctuations (see table 4.1).
The average temperature error increases quadratic with the step width (see figure 4.2). As a compromise between accurate and fast simulations, we chose a step width of $\Delta t = 0.04\tau$ for the forthcoming simulations. With this steo width, the temperature error is less than 5%.
We also compared two types of noise for the random term $\mathbf{F}^R$: Gaussian distributed noise and uniform noise with the same standard deviation. No significant difference could be observed in the outcome of these simulations. As uniform distributed

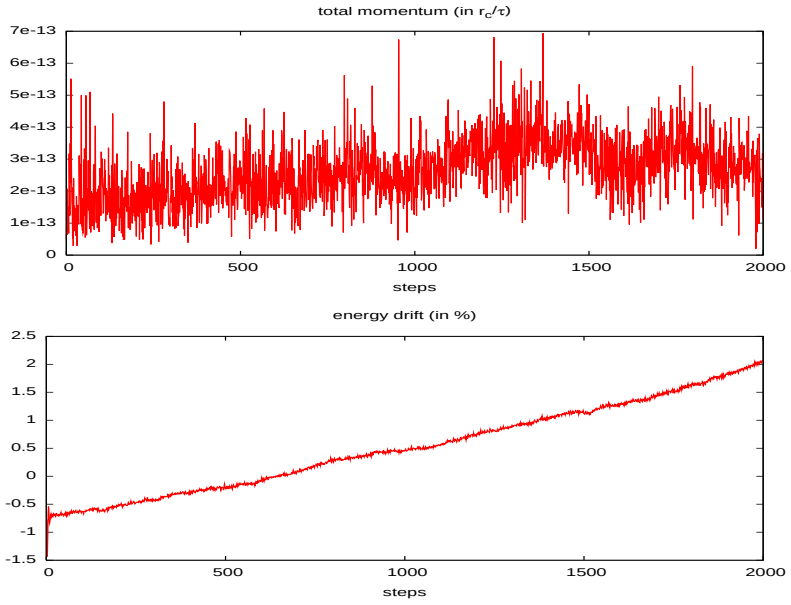

Figure 4.1: Total momentum and energy drift for a conservative pure aqueous system.

Δt	max.	mean
0.02τ	$4.1743 \times 10^{-13} r_c/\tau$	$1.4381 \times 10^{-13} r_c/\tau$
0.04τ	$5.5025 \times 10^{-13} r_c/\tau$	$2.3859 \times 10^{-13} r_c/\tau$
0.05τ	$9.3583 \times 10^{-13} r_c/\tau$	$4.4859 \times 10^{-13} r_c/\tau$
0.06τ	$5.4772 \times 10^{-13} r_c/\tau$	$1.7897 \times 10^{-13} r_c/\tau$
0.07τ	$4.3885 \times 10^{-13} r_c/\tau$	$1.7386 \times 10^{-13} r_c/\tau$
0.08τ	$4.9489 \times 10^{-13} r_c/\tau$	$2.3554 \times 10^{-13} r_c/\tau$

Table 4.1: Numerical fluctuations in the total momentum of the conservative system for different numerical step sizes Δt.

random numbers are faster to calculate, we will perform most of the forthcoming simulations with the latter type of noise.

4.1.2 Estimation of transient time

We can estimate the transient time by means of the fluctuation dissipation theorem that has been discussed in section 3. If we set up the system in a random initial condition (random particle position, 0 initial velocity), chances are, that the potential energy of the system is high compared to its equilibrium value. According to the fluctuation dissipation theorem, the system will respond linear to the amount of the perturbation, hence the relaxation will be exponential in time. Figure 4.3 shows the relaxation of total energy for the system of the last section with $\Delta t = 0.04\tau$. After approxiamtely 3 time units, the total energy is within the range of equilibrium fluctuations.
To see, whether this value is really a good estimate for the transient time, we also observed the evolution of the velocity distribution for our system. For a system in

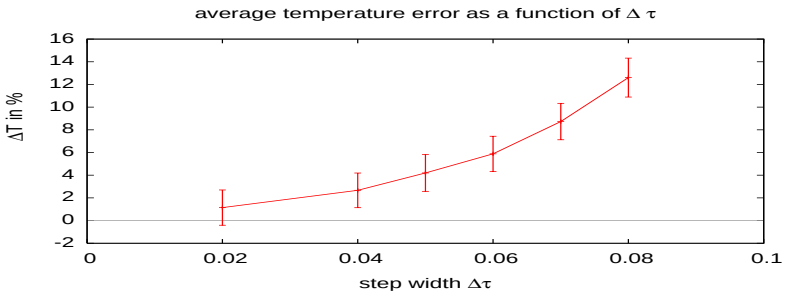

Figure 4.2: Average and standard deviation of the temperature error ΔT as a function of numerical stepwidth $\Delta\tau$.

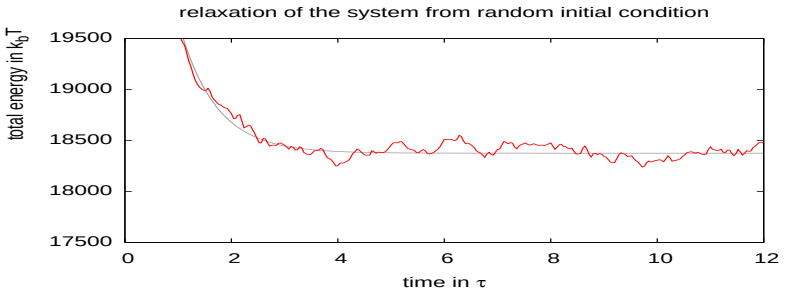

Figure 4.3: The total energy evolution of an aqueous system of size $10 \times 10 \times 10$ with step width 0.04τ follows an exponential decay (fitted to the data). After approximately 3 time units, the system has reached an equilibrium state.

thermodynamic equilibrium, the distribution of velocities is a stationary Maxwell distribution [45]. Figure 4.4 shows the time evolution of the velocity distribution from $t = 0.0\tau$ to $t = 4.0\tau$. Initially, particles feel a strong acceleration due to the high potential energy in their initial state. After only four interations the distribution already obeys its equilibrium shape, but the position of the peak and the variance are too high. At time $t = 1.5\tau$, the velocity distribution has reached its equilibrium shape. It is interesting that the velocity distribution equilibrates faster than the total energy. In other words, the kinetic energy equilibrates faster than the potential one. The only possible cause for this is an overdamping of the system: potential energy is transformed to kinetic energy, but kinetic energy is dissipated faster than it is produced.

4.1.3 Pair correlations and phase transitions

A second distribution that gives insight into our system is the radial distribution function $g(r)$. This pair correlation function expresses the density of particles on a sphere with radius r around another particle, averaged over all particles. It can be approximated by a histogram over spherical shells with width Δr:

$$g(r) = \frac{n(r, r + \Delta r)}{4N\pi r^2 \rho} \tag{4.4}$$

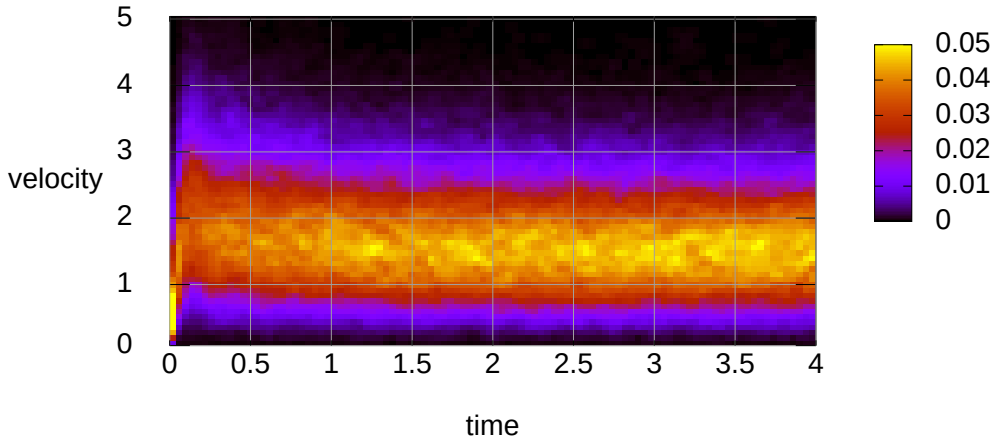

Figure 4.4: Time evolution of the velocity distribution during transient time. After only a few iterations, the distribution ressembles the characteristic Poisson distribution of statistical mechanics.

where $n(r, r+\Delta r)$ is the number of particles in the shell with radius r and N denotes the total number of particles. $n(r, r+\Delta r)$ is devided by the area $4\pi r^2$ of the shell, simply because more particles are expected to lie in the shell if the radius increases. We further devide by the average particle density ρ to ensure that $g(r)$ goes to one when r goes to infinity.
For a perfect crystal $g(r)$ would exhibit a series of peaks characteristic to the cristalline structure of the crystal. For a liquid, $g(r)$ is less structured due to the thermal motion of particles. It still exhibits peaks at small values of r. However, at longer distances, particle positions become less correlated, the peaks get broader and their magnitude is reduced. Figure 4.5 shows the radial distribution function for the pure aqueous system at different temperatures[1].
As expected, $g(r)$ shows several peaks that are more distinguished, the lower the temperature of the system is. For unit temperature $1k_bT$, only two peaks are significantly above the noise level, the first located around $0.875r_c$, the second around $1.6r_c$. For lower temperatures, further peaks can be observed. One might expect to find a phase transition for a critical temperature below which the system forms a crystal. However, even for temperature $0k_bT$ we could not find any crystaline structure. Instead, correlations still tend to disappear for longer particle distances. The cause for this might be that the system is frustrated – hence glass-like – and does not relax to its crystaline state within reasonable simulation times. Trofimov suspects this to be an artefact of the periodic boundary conditions of the simulation and points out how $g(r)$ changes with ρ [43].
An alternative approach to decide on fluid solid phase transitions is to analyze the

[1]We made a mistake in the key of figure 4.5: the analyzed temperatures are: $0.25k_bT$ instead of $0.5k_bT$, $0.0625k_bT$ instead of $0.25k_bT$ and $0.015625k_bT$ instead of $0.125k_bT$.

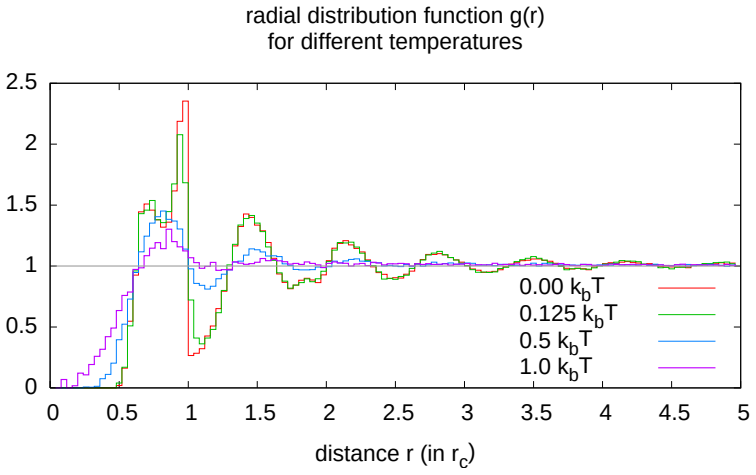

Figure 4.5: Radial distribution function $g(r)$ for different temperatures. The lower the temperature the stronger are the correlations – structures – in the system. However, even for temperature $0k_bT$, correlations vanish over long particle distances.

mean square displacement of particles in the system. The mean square displacement is defined by

$$msd = \left\langle |\mathbf{r}_i(t) - \mathbf{r}_i(0)|^2 \right\rangle \tag{4.5}$$

where the brackets denote the ensemble average over all particles in the system. For very short times, the *msd* grows quadratic in time. However, once a particle approaches one of its neighboring particles, it is hindered by the interactions between the two. As a consequence, the growth of the *msd* may be saturated. In the gas phase, the *msd* still grows quadratic with time, although slower than for the ideal gas. In a fluid, the *msd* grows linear with time, and, finally, in a solid, particles nearly never exchange their positions, thus, the *msd* saturates to a constant.
We can measure the *msd* straight forward to its definition. However, we have to be carful that boundary effects do not disturb the result. Therefore, we stop the calculation when the displacement of a single particle on the simulation exceeds half the size of the system. Before we measure, we let the system relax until the temperature error is less than 5%. It should be noted, however, that for low temperatures this might still correspond to the transient of the system, as temperature fluctuations become less when temperature is decreased. If this is the case, the *msd* will show a negative curvature, as particle motion slows down as the system approaches its equilibrium.
Figure 4.6 shows the mean square displacement as a function of time for different temperatures ranging from $0.0k_bT$ to $1.0k_bT$ [2]. For high temperatures ($0.25k_bT$ to $1.0k_bT$) the *msd* saturates to a straight line characteristic for fluids. A numerical fit yields a gradient of $1.201r_c^2/\tau$ for $1.0k_bT$, $0.214r_c^2/\tau$ for $0.5k_bT$ and $0.011r_c^2/\tau$ for $k_bT = 0.25$. This gradient is directly related to the self-diffusion constant of the fluid [45]:

$$D = \lim_{t\to\infty} \frac{1}{6t} msd(t) = \frac{1}{6}\frac{d}{dt} msd \tag{4.6}$$

[2] Figure 4.6 shares the mistake of figure 4.5. The correction is given in footnote 1.

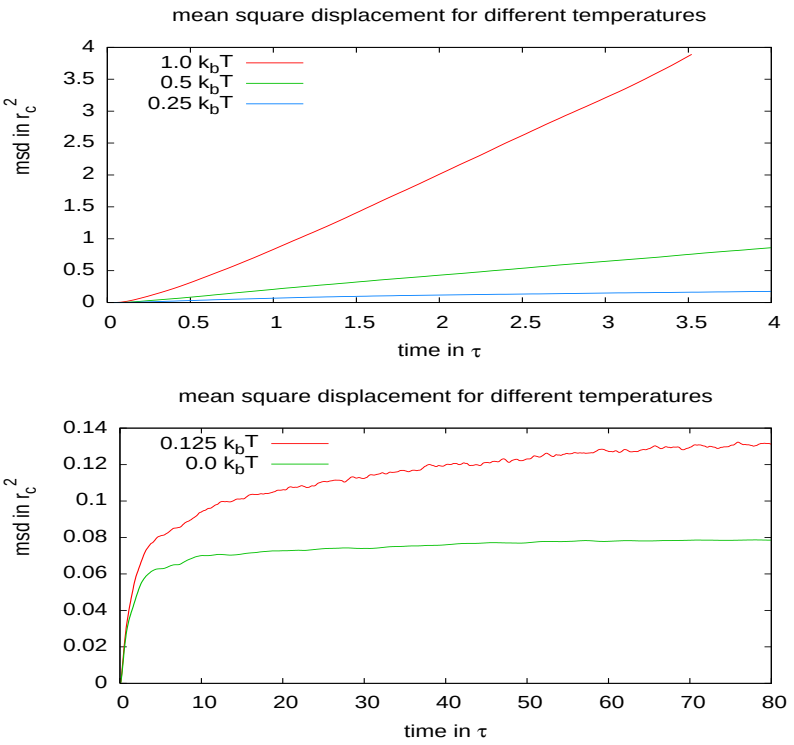

Figure 4.6: Mean square displacement for temperatures ranging from $1.0k_bT$ to $0.0k_bT$.

For lower temperatures (figure 4.6, bottom) shows the mean square displacement for $6.25 \times 10^{-2} k_bT$ and $1.5625 \times 10^{-3} k_bT$. In these cases, the system is still in a transient and possesses to much kinetic energy, when we start the the measurements. Due to the ongoing decrease of kinetic energy, the graphs for the msd have a negative curvature. We performed simulations until $t = 80\tau$ to decide, whether the msd approaches a finite value. However, even for large t, the linear function fitted to the data had a positive gradient.

4.1.4 Summary

In this section, we used the DPD formalism to analyse pure aqueous systems. These simulations had two purposes. First, the pure water system is best for validation of our implementation. Second, we measured several properties of the system, that we will use for further calibration.
We did the validation both for conservative and dissipative systems. We could show that for DPD standard parameters ($k_bT = 1$, $r_c = 1$, $\rho_W = 3.0 r_c^{-3}$, $a_{WW} = 25 k_bT$) total momentum is conserved up to $10^{-12} r_c/\tau$ which is close to the numerical resolution. We observed a slight trend in total energy for the conservative system. However, we do not expect this trend to introduce noteworthy errors, once the dissipative thermostat is used to equalibrate energy. For the dissipative system, we found that the difference between measured and tuned temperature depends quadratic on the numerical step width. For step widths commonly used in DPD

simulations, we estimated this error to be less than 5%. We estimated the transient time of the pure aqeous system at $1k_bT$ around 3τ for a step width of $0.04\Delta\tau$. From the total energy evolution and the velocity distribution, we could estimate the transient time τ_{trans}. For $1k_bT$ we obtained $\tau_{trans} < 3\tau$. We furthermore analyzed the radial distribution function and the mean square displacement of a pure aqueous system for various temperatures. Both of them did not show sharp transitions between a liquid and a solid phase.

4.2 Micellar system

To relate the simulations to experimental knowledge, we calibrate these parameters to the surfactant sodium heptylsulfate $Na^+C_7H_{15}SO_4^-$. However, the procedure we present here can be easily adapted to fit other surfactants like those in table 2.1. We first relate the length scale r_c and time scale τ of our simulation to the scales of the physical system. Then, we try to derive interaction parameters a_{ij} from known values $(N, CMC, \Delta G)$ of our system. The procedure we describe is orientated on the work of Groot and Rabone [54] but differs in the set of mesoscopic parameters that are fitted.

4.2.1 Physical length and time scale

We choose a coarse graining where heptylsulfate is represented by one head and one tail particle (see figure 4.7). Heptylsulfate is known to form spherical micelles of aggregation numbers around 22 with a radius approximately the length of the hydrocarbon chain – given as $(1.5 + 7 \times 1.28)$Å$= 10.46$Å. To fix the physical length scale r_c of our model, we set the radius of a micelle in our simulation to $1.5r_c$. This is a reasonable compromise between detailed representation and a physical relevant system size. From this relation we obtain the physical length scale of our simulation: $1r_c$ represents 6.97Å. With $r_c^3 \hat{=} 339$Å^3 and a chosen water density of $\rho_W = 3r_c^{-3}$, we find that the volume per water bead is 113Å^3. The molecular volume of real water is 30Å^3 [54]. Thus, one DPD bead lumps together 3.76 water molecules on the average. This value is called the coarse graining parameter (usually denoted N_m) and is a common numner to express the level of coarse graining for DPD simulations. Typically, N_m is between 3 and 5.
Knowing N_m, we can deduce a unit of concentration:

$$1mol/l \quad \hat{=} \quad \frac{N_A N_m}{\rho_W} \frac{(69.7nm/r_c)^3}{(10^8 nm)^3} \tag{4.7}$$

where N_A is the Avogadro number. We find that in our model, $1mol/l$ is represented by 0.256 particles per unit cube. From our analysis of the closed association model, we know that only 4% of the surfactant is micellized when the surfactant

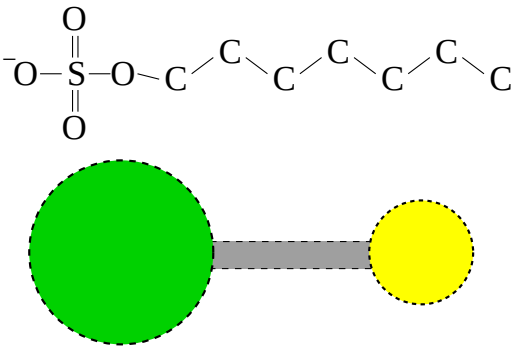

Figure 4.7: The surfactant heptylsulfate $C_7H_{15}SO_4^-$ and our coarse grained DPD representation by one head and one tail bead connected by an elastic spring.

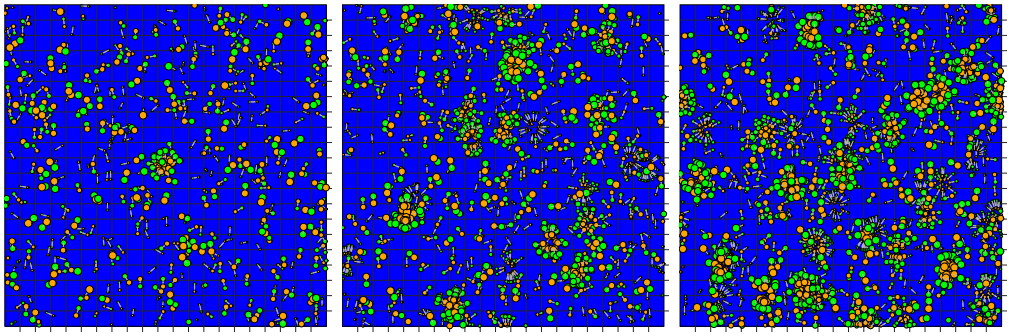

Figure 4.8: System states for three different surfactant concentrations. Amphiphiles are shown in yellow (tail beads) and green (head beads), water beads are not shown. The pictures are not the result of simulations, but show what has to be achieved by the calibration. Values are obtained from the closed association model (see text). System size is $(21r_c)^3$. For $[S]_T = CMC$ (left panel), one micelle of 22 surfactants forms while 484 surfactants are in bulk phase (4% micellization). For $[S]_T = 2CMC$ (middle), around 21 micelles are found and 550 surfactants are in bulk phase (45.5% micellization). For $[S]_T = 3CMC$ (rigth), one finds 43 micelles and 572 free surfactants.

concentration equals the CMC. To model a system at the CMC (5.632×10^{-2} particles per r_c^3), that contains only one micelle, we would need a simulation box of size approximately $(21r_c)^3$ that holds 506 surfactants and approximately 27000 water particles (to result in a average particle density of $3r_c^{-3}$). Snapshots of such systems for different surfactant concentrations are shown in figure 4.8.
The time scale of our model is related to the length scale by the self-diffusion of water that has been analyzed in section 4.1.3. For an equilibrium temperature of $1k_bT$ ($\nu = 4.5$, $\sigma = 3.0$) we measured a self-diffusion constant of $0.2002r_c^2/\tau$. When we relate this to the real self-diffusion of water given as $(2.43 \pm 0.001) \times 10^{-5} cm^2/s$, we can calibrate the physical time scale of our model. Some care has to be taken here, because in our model, one DPD bead represents 3 to 4 water molecules. It has been shown by Groot and Rabone that the physical and real diffusion of water are related by $D_{exp} = N_m D_s im$ [54]. We therefore obtain

$$\tau = 3.76 \frac{0.2002 r_c^2}{2.43 \times 10^{-5} cm^2/s} = 3.76 \frac{(0.2002 \times 6.97 nm)^2}{243 nm^2/s} = 150.49 ps \tag{4.8}$$

Groot and Rabone obtain a physical time scale around $88ps$ [54]. The difference can be explained by the water water bead interaction of $76k_bT$ they used (and for which they measured a diffusion constant of $0.1707r_c^2/\tau$), whereas we used the standard parameter $25k_bT$ from [38]. Although the value of $76k_bT$ seems to be closer to the physical system, we have chosen the standard parameter to have more comparable results. Let us again illustrate which scale of the physical system can be catched by our model. From section 2.2.2, we know that monomer association and dissociation happens in the order of nanoseconds ($k^- = 7.3 \times 10^8 s^{-1}$, and hence $1/k^- = 1.370ns$). We should therefore expect to find monomer associations and dissociations approximately every 9.104 DPD time units (228 iterations).

We have seen from the above calculations that our DPD model can capture the kinetics of heptylsulfate and probably short chain surfactants in general in the interesting length and time scale. The necessary system size to capture the system at the CMC is already at the upper bound of what is feasible in DPD simulations. However, the situation gets rapidly better for higher surfactant concentrations. For comparision, if we want to model sodium dodecylsulfate ($NaC_{12}H_{25}SO_4$)—assuming the same coarse graining parameter $N_m = 3.76$—a system size of $(126r_c)^3$ holding six million particles would be necessary to capture one micelle at the CMC. Monomer dissociations occur every 664.50 DPD time units, or 16612 iterations. The runtime of our simulations to capture the same kinetic events would therefore increase by four orders of magnitude. This is certainly beyond the scope of our model.

4.2.2 Parametrization

Once the physical scale of our model is known, we can try to fit the interaction parameters of our model to empirical data of the system. We are interested in concentration regimes where heptylsulfate forms spherical micelles of aggregation number around 22 and a radius of $r = 1.5r_c$. This means, that the average head distance in the micelle will be $r^*_{\mathbf{HH}} = \sqrt{4\pi r^2/22} = 1.133r_c$. At this distance, the resulting potential energy between two head groups should be the same as for two water particles: $\phi_{\mathbf{HH}}(r^*_{\mathbf{HH}}) = \phi_{\mathbf{WW}}(r^*_{\mathbf{WW}})$ From the first peak in the radial distribution function, we know that $r_{\mathbf{WW}}(r^*_{\mathbf{WW}}) = 0.875r_c$. We found that the desired potential is approximately achieved if we set $r^c_{\mathbf{HH}} = 1.5r_c$ and $a_{\mathbf{HH}} = 37.5k_bT$. Under the assumption that head particles have the same hydrophilic behavior as water, we set $r^c_{\mathbf{HW}} = r^c_{\mathbf{WW}} = 1r_c$ and $a_{\mathbf{HW}} = a_{\mathbf{WW}} = 25k_bT$.
We have now specified all necessary parameters for the water and head particles, respectively. We need to specify three further interaction potentials for the tail particles. To estimate these values, we would need to relate the free energy change ΔG^0_{mono} of surfactants in bulk phase and micellar phase to the interaction potentials $\phi_{\mathbf{TT}}$, $\phi_{\mathbf{TH}}$ and $\phi_{\mathbf{TW}}$. However, a rigorous calibration to capture all physical properties of a micellar system is a time-consuming endeavor. Until this point, it remains even unclear whether the softcore potentials usually used in DPD simulations can successfully capture all important kinetics of a micellar system. Unfortunately, the project our work is embedded in did not allow to spend much time and efford on method development. Although we undertook several attempts to calibrate our model, we have not been able to accomplish the task in the given time. While we will continue this analysis in future work, we will proceed with an uncalibrated model for the remainder of the simulations. The parameters of this model have been achieved by try and error to catch the properties of micelles necessary to serve as a protocellular container—namely, we tried to find a parameter set that allows micelles to grow and divide after reaching a critical size.
The bond interaction of the $\mathbf{H}-\mathbf{T}$ bond has been set to $r_b = 0.5r_c, b = 125k_bT$. The effective bond length, however, will increase because of the additional bead repulsion. To ensure that micelles maintain their spherical shape we captured a surfactant parameter $N_S < 1/3$ with the tail tail interaction $r^c_{\mathbf{TT}} = 0.5r_c$ and $a_{\mathbf{TT}} = 12.5k_bT$. Finally, head tail and water tail interactions have been set to $r^c_{\mathbf{HT}} = r^c_{\mathbf{WT}} = 1.5r_c$,

and $a_{\mathbf{HT}} = a_{\mathbf{WT}} = 37.5 k_b T$, which is equal to the head head interactions. With these values, the effective bond length for an isolated $\mathbf{H} - \mathbf{T}$ pair evaluates to $0.643 r_c$. Table 4.2 summarizes all interaction parameters used.

	W	**H**	**T**
W	$1.0, 25$	$1.0, 25$	$1.5, 37.5$
H	$1.0, 25$	$1.5, 37.5$	$1.5, 37.5$
T	$1.5, 37.5$	$1.5, 37.5$	$0.5, 12.5$

Table 4.2: Interaction parameters (r_{ij}^c, a_{ij}) as multiples of r_c and $k_b T$ for a micellar system consisting of water **W**, amphiphile head **H** and tail **T** beads. The bond interaction between $\mathbf{H} - \mathbf{T}$ is set to $125 r_c, 0.5 k_b T$.

4.2.3 Equilibrium micellar system

With the interaction parameters described in the last section, we performed simulations in a box of $12.5 \times 12.5 \times 12.5 r_c^3$ intialized randomly with 212 surfactants and 5433 water beads which corresponds to 2 times the CMC (particle density $3.0 r_c^{-3}$). Simulations where performed for $0\tau \leq t \leq 350\tau$

To obtain micellar size distributions from our model, we need to define a criterion that distinguishes micelles from monomers in the bulk phase. We decided that every two monomers, whose tail bead distance is less than $1.0 r_c$ participate to the same micelle. As $1.0 r_c$ is smaller than two times the effective bond length, this measure will accurately seperate nearby proper micelles. For monomers in bulk phase any such cutoff is rather arbitrary. Establishing this criterion, we adapted the simple flood-filling algorithm (see e. g. [59]) to identify micelles.

Figure 4.9 shows the initial condition and snapshots of the time evolution. The evolution of the micellar size distribution is plotted in figure 4.10. Initially, the system

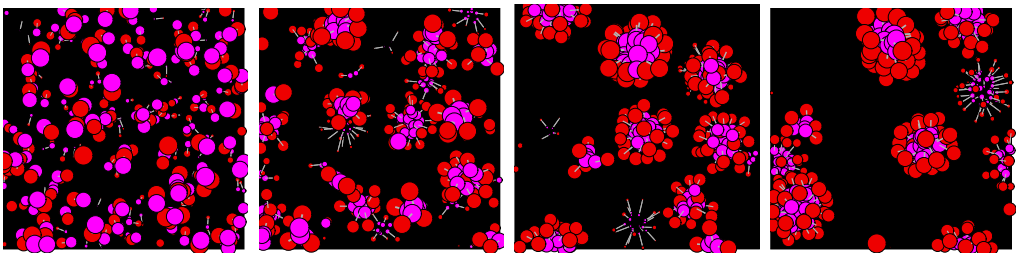

Figure 4.9: Self assembly of micelles in aqueous solution. Amphiphiles are shown in purple (tail beads) and red (head beads). System states are shown for $t = 0\tau$, $t = 12\tau$, $t = 100\tau$, and $t = 200\tau$.

is composed almost only of monomers along some dimers and trimers. During the simulation, monomers quickly form submicellar assemblies. These assemblies successively aggregate into bigger structures until spherical micelles occur. After 160 time units the size distribution reaches a stationary distribution with final aggregation numbers between 25 and 35 and a radius of approximately $3.5 r_c$. Hence, in our simulation, micellization follows a Smolouchowsky path to equilibrium (see 2.4)

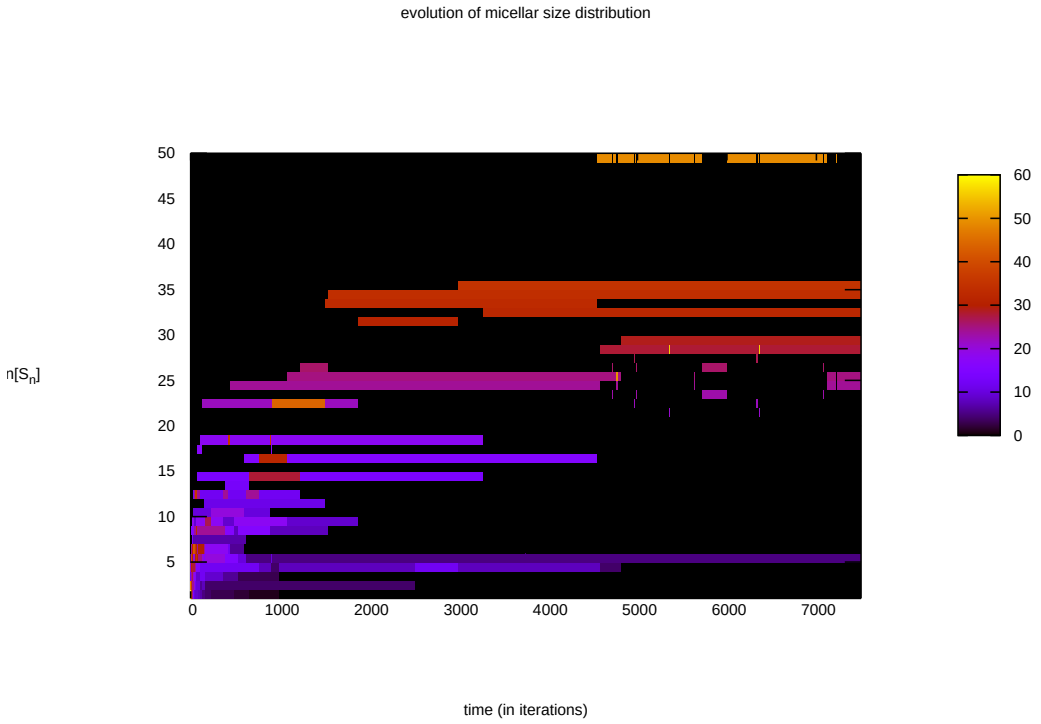

Figure 4.10: Evolution of the micellar size distribution for $0\tau \leq t \leq 375\tau$ (7500 iterations). After 160 time units the size distribution reaches a stationary distribution with final aggregation numbers between 25 and 35.

rather then a Becker-Döring like. Interestingly, between $t = 180\tau$ and $t = 290\tau$ two micelles temporarily fuse into an assembly of aggregation number 49. This assembly, however, is unstable and divides again. Fusion and division occur several times. During this process, monomers amoung the assemblies are exchanged. Thus, we can clearly see, that in this experiment, the aggregation number of assemblies has an upper limit.
Furthermore, we could not observe monomer dissociations from assemblies in the equilibrium regiem of the system: once inside a micellar aggregate, an amphiphile remains in the aggregate for the remainder of the simulation. As a consequence, the equilibrium distribution of our system consists only of micelles. No monomers are found in the bulk phase. The equilibrium distribution in our simulation is not only stationary but even steady.

4.2.4 Non-equilibrium micellar system

In the forthcoming simulations, we drive the micellar system out of its equilibrium by the introduction of chemical reactions. In this way, catalytic reactions might allow growth, destabilization and eventually fission of micellar aggregates. According to the prebiotic scenarios we will represent in the next sections, we defined a catalytic reaction that transforms precursor molecules into amphiphiles in the vicinity of existing surfactants.
Precursor molecules are modeled as single DPD particles **X** that can undergo the

autocatalytic reaction

$$\mathbf{X} + \mathbf{X} \xrightarrow{\mathbf{T}} \mathbf{H} - \mathbf{T} \tag{4.9}$$

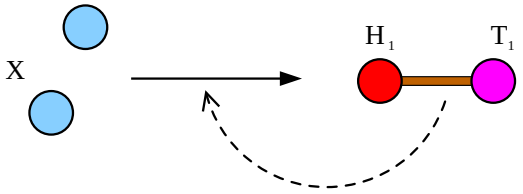

To localize the catalytic effects within a small region surrounding the micelle, we have choosen to make the tail part of the amphiphiles catalytic. Spontaneous reaction rates have been set to 0.0, whoch allows us to focus on the autocatalytic kinetics in the model. Catalyst radii are set to $1.0r_c$ with a maximal catalytic rate of 1.0.
We also tried reaction kinetics, where the head part of the surfactants serve as catalysts. However, with these settings, results became less clear than with the above reaction scheme. Using the same catalytic range of $1.0r_c$, new amphiphiles where formed comparatively far away from the micellar surface. These monomers did not join the existing aggregate but often formed new aggregates with other monomers in the bulk phase. We could reduce the probability of these events by reducing the catalytic range ro $0.5r_c$. However, the overall catalytic effect decreases cubic with the catalytic radius. Thus, simulation times were drastically increased, when using amphiphilic heads as catalyst with a short ranged catalytic effect.
To link to later simulations of the Lidip World, we decided to allow the precursor to diffuse relatively unhindered through the system. By making them weak polar particles, we avoid that the precursors themself assemble into droplets in the aqueous phase. Doing so, they can approach the micelle as individual particles and newly synthesized amphiphiles can enter the micelle one by one. We model these weak interactions with the following interaction parameters in addition to those used in table 4.2:

	W	**H**	**T**	**X**
X	0.5, 12.5	0.5, 12.5	0.5, 12.5	1.0, 25

With these additional parameters, we performed simulations in a space of size $7.5 \times 7.5 \times 7.5r_c^3$, initialized randomly with 1265 water and 210 precursor beads. A single initial amphile has been placed in the center of the box. Note that the average particle density $\rho \approx 3.5r_c^{-3}$ is higher than in the previous simulations. However, if we reduce the particle density, the system pressure would drop due to the weak precursor interactions. In order to constantly drive the system out of equilibrium, we introduce a particle exchange in the corner of the simulation space. In a spherical region of radius $2.0r_c$, water beads are exchanged by precursors with a probability of 1×10^{-3} per particle and time unit.
We run the simulation for 250 time units. Snapshots of the evolution are shown in figure 4.11. We observed that new surfactants are synthesized rapidly in the vicinity of the initial amphiphile. These surfactants form a spherical micelle, that grows in size by successively incorporating newly formed monomers. After a certain time,

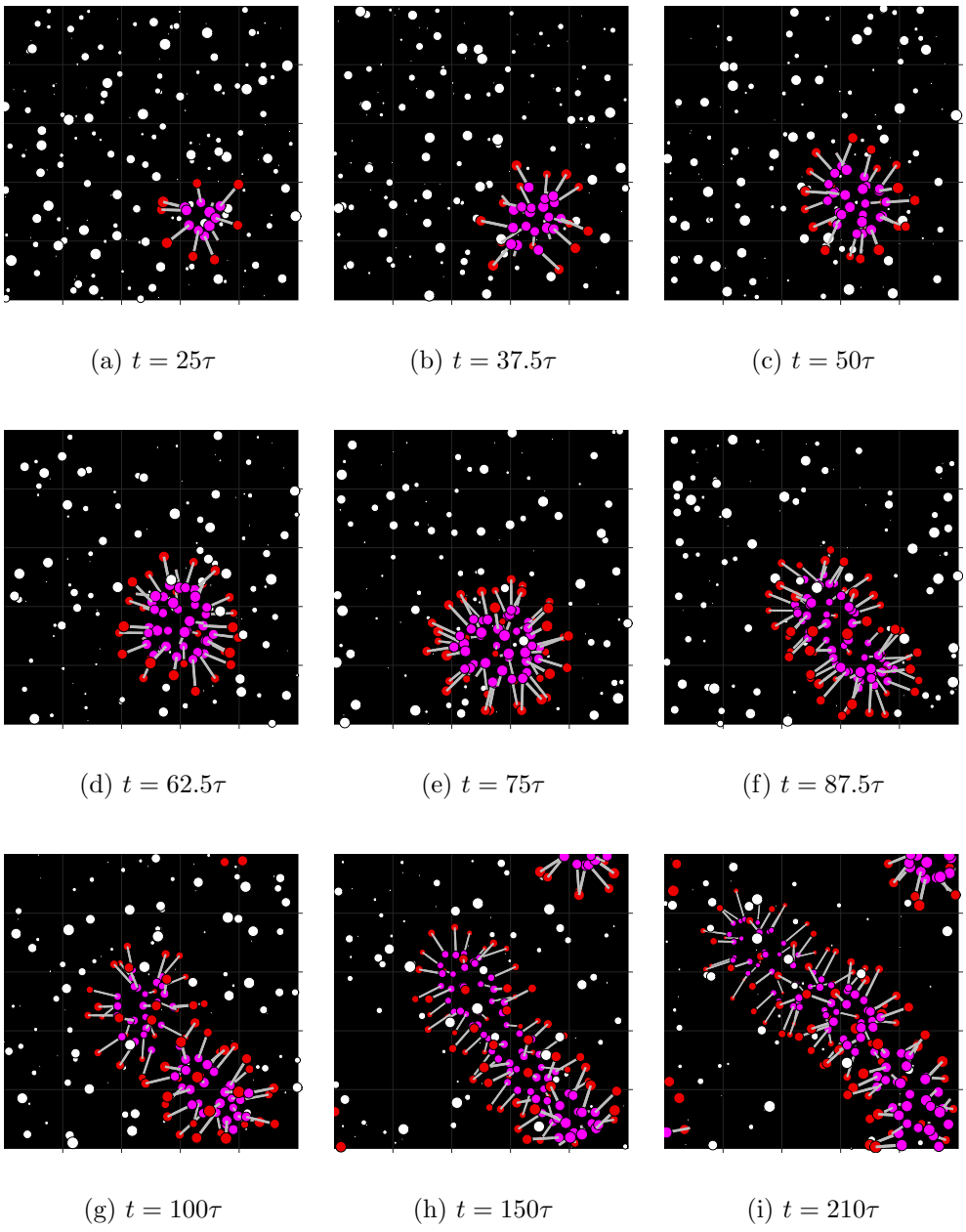

(a) $t = 25\tau$ (b) $t = 37.5\tau$ (c) $t = 50\tau$

(d) $t = 62.5\tau$ (e) $t = 75\tau$ (f) $t = 87.5\tau$

(g) $t = 100\tau$ (h) $t = 150\tau$ (i) $t = 210\tau$

Figure 4.11: Autocatalytic growth of a micelle. Precursors (white) are transformed into new amphiphiles (red and purple) in the vicinity of present amphiphiles. An initial micelle forms (a) and successively incorporates new surfactants (b-e). The spherical shape becomes unstable and the assembly turns into a rodlike shape (f). This shape elongates while the simulation proceeds (g-i).

the aggregation number of the micelle is too high to maintain a spherical shape and the micelle turns into a rodlike aggregate (f). In the elongated form, the micelle temporarily tends to dissociate into smaller aggregates (g). However, in none of the performed simulation runs, the eventual fission into two seperate aggregates could be observed. Instead, the aggregate rearranged into its rodlike shape again and continued its growth (h-i).

It is interesting that the rodlike aggregate does not form in the equilibrium system analyzed in the previous section. Even if we turn of the precursor supply at some point, to allow the autocatalytic system to settle in an equilibrium, it keeps its rodlike shape. This means that the system exhibits hysteresis: the final state depends on the kinetic pathway, i. e. on the history of the simulation. An explanation for this behavior is the following: in the equilibrium state, micellization follows a Smolouchowsky route. Monomers assemble into small aggregates that successively join into bigger and bigger aggregates. With a certain size, however, the energy barrier for two micelles to join becomes large because of the comparatively strong head head repulsion. In the non-equilibrium scenario, on the other hand, amphiphiles are synthesized one after the other, and are individually incorporated into the assembly. In this sense, they follow the Becker-Döring route. The energy barrier for a single amphiphile is smaller then in the former case. It becomes essentially independent of the aggregation number, once the rodlike micelle has formed. Thus, the non-equilibrium system can overcome the maximal aggregation number found in the equilibrium system.

We tried to force the elongating aggregate into a fission scenario by increasing the repulsive force between the head beads, because a stronger head repulsion was thought to increase the ideal curvature and thus energetically favors small aggregates. However, even for high head head repulsions ($a_{\mathbf{HH}} = 75k_bT$) we could not find actual fission. The aggregate remained rodlike. Only the distance between surfactants increased. Tail beads are seperated by more than $r^c_{\mathbf{TT}}$ in this configuration. The potential energy contribution of these tail pairs is zero. Tail particles can therefore move freely in the interiour of the rod, but there is no sufficient driving force to actually push the tails beads together to transform the elongated aggregate into smaller spheres.

We then decided to introduce an explicit attractive force between two tail particles. This mimicks the van-der-Waals attraction between the hydrocarbon chains of the surfactant. Note also that in the derivation of softcore potentials (section 3.3) we find remainders of this attraction in the measured effective potential. We achieved this attraction by replacing the linear force used before by a stepwise linear function. To be precise, we define the tail tail interaction force $\mathbf{F}^C(r)$ by linear interpolation between the points (0,12.5), (0.5,-3.75), (0.75,-1.875), (1.5,0). The interactions between tails and other particles remained unchanged. See figure 4.12 for a plot of all used interaction potentials.

With the modified tail interactions, we reran the experiment of autocatalytic micellar growth. Figure 4.13 shows snapshots of the time evolution of the system. Again, a spherical micelle forms around the initial surfactant (a). The micelle grows in size until the spherical micelle becomes unstable (e) and elongates into a rod again (f). Unlike in the last experiment, the rodlike shape is unstable due to the attractive

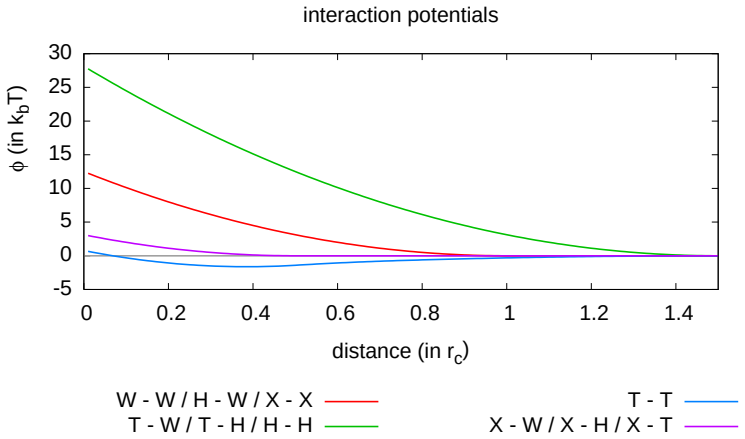

Figure 4.12: Interaction potentials for the micellar fission scenario. The potentials are integrals of stepwise linear interaction forces (see text).

tail interactions: tail beads concentrate in the cap regions of the elongated micelle, leaving a gap in its center. This gap induces the division of the rodlike aggregate into two smaller assemblies (g). With the constant supply of new precursors, growth, destabilization and fission continues while the simulation is running (h-i).
The size distribution of micelles as a function of time is plotted in figure 4.14. We found aggregation numbers between 25 and 55. Only the first micelle in our simulation reached an aggregation number of more than 60. We further observed, that the growth of individual micelles is approximately linear in time, although an exponential growth might be excepted due to the autocatalytic reaction scheme 4.9. The growth however is limited by the diffusion of precursors which is linear in time within aqueous phase (see section 4.1.3). During the whole simulation, the growth rate decreases and the replication of micelles slows down. This might be due to the consumption of precursors when their initial concentration is higher than their supply.

4.2.5 Summary

In this section, we have related the length and time scale of our model to the physical scales of a sodium heptylsulfate system. It turned out, that our model operates in a physical regime where micellar kinetics can accurately be captured. We related properties of the real system (surfactant concentration, number of micelles) to our model and discussed possibilities and difficulties concerning the calibration of the method.
Unfortunately, we could not develop a calibrated model in the given time. Thus, we presented the parameter set of a toy model, which we developed to capture the micellar kinetics envisioned in the Lipid World scenario. It turned out however, that this model produces artefacts when applied to an equilibrium surfactant system. Namely, we could not observe monomer dissociations from micelles. As a consequence, there are no free monomers in the bulk phase, once the simulation has reached a steady state.

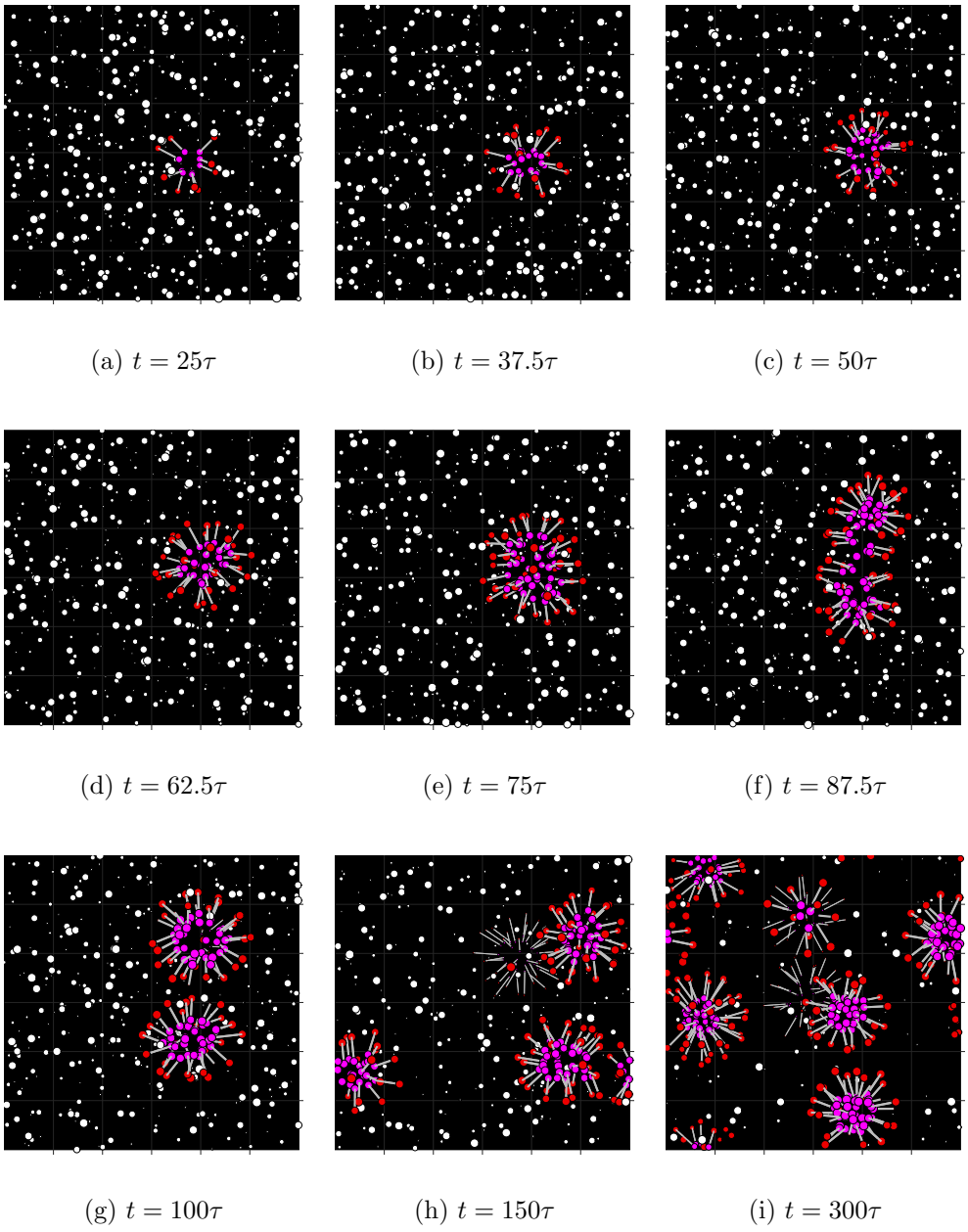

(a) $t = 25\tau$ (b) $t = 37.5\tau$ (c) $t = 50\tau$

(d) $t = 62.5\tau$ (e) $t = 75\tau$ (f) $t = 87.5\tau$

(g) $t = 100\tau$ (h) $t = 150\tau$ (i) $t = 300\tau$

Figure 4.13: Fission of spherical micelles (color scheme is the same as in figure 4.11): Driven by the synthesis of new amphiphiles, the initial micelle grows until its spherical shape becomes unstable (e). Reaching this size, it rearranges into an elongated, rodlike micelle. Amphiphile tails concentrate at the caps of this rod, forming a gap at the center (f). This gap initiates the fission of the micelle (g), that leads to two micelles of initial size. This process continues when new amphiphiles are formed (h-i).

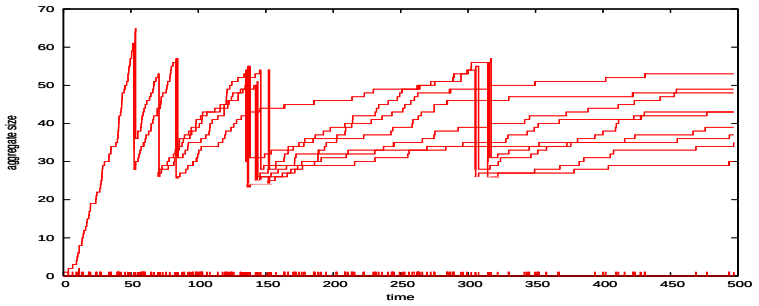

Figure 4.14: Evolution of micelle sizes for successive micellar fissions. Every line depicts the size of an individual micelle. Vertical lines correspond to actual fission events.

We also applied our model to a system, that is driven out of its equilibrium by the autocatalytic synthesis of new surfactants from supplied precursors. Contineous supply of precursor lead to the formation of a rodlike micelle. This micelle is stable even if the precursor support is eventually stopped. We discussed an hystersis effect in the equilibrium solution depending on the actual kinetic pathway which lead to the equilibrium state.
Finally, we could force catalytic growing micelle to divide by introducing attractive interaction between the tail beads of amphiphiles. Doing so, we could find model parameters that allowed the growth, destabilization and fission of sperical micelles, like it is envisioned in the Lipid World theory.

4.3 The Lipid World

In this section, we analyze the Lipid World scenario. Rather than to rebuild a complete GARD model in our extended DPD model, we focus our analysis on the consequences implied by the introduction of space into the theory of Lancet et al. It has been pointed out in section 1.1 that interesting spatial phenomena occur already for binary amphiphilic assemblies, that is, for aggregates composed of two sorts of surfactants. Therefore, we restrict our simulations to the case of two catalytically interacting amphiphiles $\mathbf{H}_1-\mathbf{T}_1$ and $\mathbf{H}_2-\mathbf{T}_2$. In particular, the catalytic network we study expresses cross-catalytic activity, i. e. the two amphiphiles mutually catalyze each other:

$$\mathbf{X}+\mathbf{X} \xrightarrow{\mathbf{T}_2} \mathbf{H}_1-\mathbf{T}_1 \tag{4.10}$$

$$\mathbf{X}+\mathbf{X} \xrightarrow{\mathbf{T}_1} \mathbf{H}_2-\mathbf{T}_2 \tag{4.11}$$

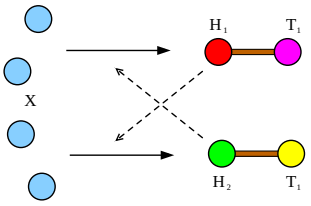

We use the same catalytic rates as in the last section: Spontaneous reaction rates are set to 0.0, catalyst radii are set to $1.0r_c$ with a maximal catalytic rate of 1.0.
Interaction parameters for these simulations were the same as in section 4.2.4 including the attractive tail in the $\mathbf{T}-\mathbf{T}$ potential. Both amphiphiles are described by identical interactions with respect to water and amphiphiles of the same type (e. g. $\phi_{\mathbf{H}_1\mathbf{H}_1}=\phi_{\mathbf{H}_2\mathbf{H}_2}=\phi_{\mathbf{HH}}$). We further set $\phi_{\mathbf{H}_1\mathbf{T}_2}=\phi_{\mathbf{H}_2\mathbf{T}_1}=\phi_{\mathbf{HT}}$ Hence, the introduction of the second amphiphile leaves us only with two more interactions to specify: $\phi_{\mathbf{H}_1\mathbf{H}_2}$ and $\phi_{\mathbf{T}_1\mathbf{T}_2}$. These parameters are subject to variation in the following experiments.
We are interested in the formation of domains and the diversity of amphiphile compositions throughout the micelles, i. e. the heterogeneity of the system. We define the global heterogeneity as the weighed sum of the Shannon entropies per micelle:

$$H=-\frac{1}{n}\sum_{i=1}^{N} n_i \sum_{j=1}^{N_G} \frac{p_{ij}}{n_i}\log_{N_G}\frac{p_{ij}}{n_i} \tag{4.12}$$

where N is the number of micelles of size n_i, $n=n_1+\ldots+n_N$, N_G the number of different types of surfactants and p_{ij} the number of surfactants j in micelle i. H lies in the interval $[0,1]$, whereby 0 is achieved for a system of micelles, that have only one type of surfactants, whereas $H=1$ is achieved when the amphiphiles are distributed equally over the micelles. Wheighing by the micellar size, we ensure that bigger micelles contribute more to H, thus new monomers that are not yet incorporated into an assembly disturb the measurement less.
We used a localized variant of this measure to quantify domain formation in terms

of heterogeneity within one micelle:

$$H_L = -\frac{1}{n}\sum_{i=1}^{n}\sum_{j=1}^{N_G} p_{ij}\log_{N_G} p_{ij} \tag{4.13}$$

where p_{ij} signifies the number of surfactants of type j whose tail beads are closer than $0.5r_c$ to the tail of surfactant i, and n and N_G are defined as above. H_L, too, ranges between 0 and 1. High values correspond to high Shannon entropies: the amphiphiles are distributed heterogeneously over the micelle. Low values signify a clear formation of domains. The exact value of H_L depends on the radius we use to determine the neighborhood of tail particles (in our case $0.5r_c$). Tendencies in H_L, on the other hand, are independent of this radius.
All following simulations have been performed with the following settings: system size was set to $7.5 \times 7.5 \times 7.5r_c^3$ (we were only interested in the surface and fission of one micelle—hence, a small system is sufficient), water density $\rho_W = 3.0r_c^{-3}$ and $\rho_X = 0.25r_c^{-3}$ if precursors are used. For every parameter set, we ran 20 simulations to get significant results.

4.3.1 Strong head repulsion

In the GARD model amphiphiles are supposed to differ in the catalytic activity of the head groups, while the amphiphile tails are supposed to be identical. Hence, it seems straight-forward to vary only the interaction potential of unlike head beads $\phi_{\mathbf{H}_1\mathbf{H}_2}$ and set all tail interactions equal: $\phi_{\mathbf{T}_i\mathbf{T}_j} = \phi_{\mathbf{TT}}$ for $i, j = 1, 2$. To identify the influence of head repulsion on domain formation, we ran simulations with $a_{\mathbf{H}_1\mathbf{H}_2}$ between $25k_bT$ and $100k_bT$, keeping $r^c_{\mathbf{H}_1\mathbf{H}_2} = 1.5r_c$ constant. We initialized the system with a micelle consisting of 15 surfactants of type 1 and 15 surfactants of type 2. No precursors have been used. Simulations have been run for $t = 0\tau$ to $t = 100\tau$ (2500 iterations). The first 5 time units have been considered as transient. The average local heterogeneities and their standard deviations are plotted in figure 4.15 against head head repulsion strength. Figure 4.16 shows snapshots of the respective systems. The stronger unlike heads repel each other, the smaller becomes the average local heterogeneity. However, the decrease is only small even for drastic changes in the mutual repulsion. The strong standard deviation for H_L suggests that these domains constantly change and are not stable over time.
Next, we introduced the surfactant synthesis from precursors with mutual catalysis. We initialized the system with a single surfactant (type 1) and provided precursors by particle exchange as in section 4.2.4. Figure 4.17 shows the number of surfactants and precursors against time. We can see that surfactant synthesis is approximately linear in time, despite the autocatalytic character of the whole system (see section 4.2.4). The curves for the two amphiphiles follow each other due to the cross-catalytic coupling. Once again, influx of new precursors is less than its turnover. Thus, the precursor is consumed with the production of new surfactants. This is not cricital, however, as we are only interested in properties of a single micelle and single fission events, not in the dynamics over many generations.
As the variance of head repulsion did not form significant domains, the fission events lead to mixed micelles with approximately the same surfactant composition. Figure

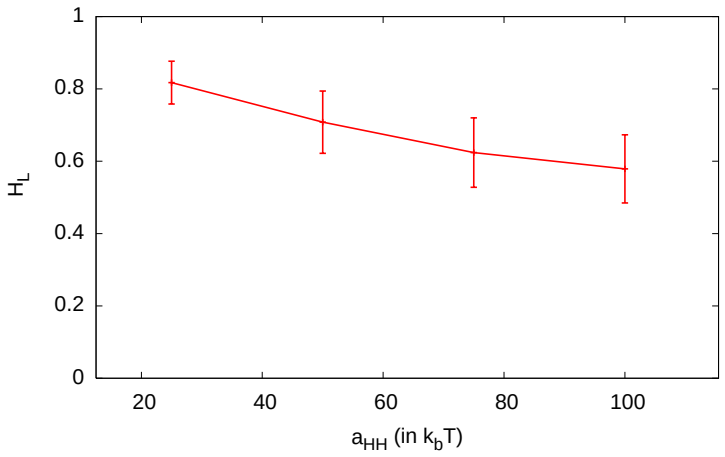

Figure 4.15: Localized Shannon entrogy H_L for different head head repulsion parameters $a_{\mathbf{H}_1\mathbf{H}_2}$. Stronger repulsion between unlike heads leads to the formation of domains. As a consequence the localized entropy decreses.

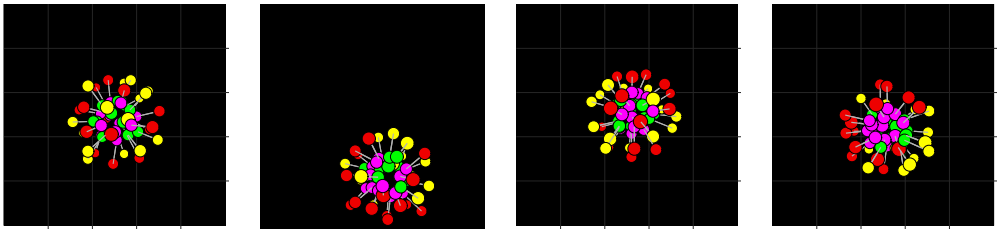

(a) $a_{\mathbf{H}_1\mathbf{H}_2} = 25k_bT$ (b) $a_{\mathbf{H}_1\mathbf{H}_2} = 50k_bT$ (c) $a_{\mathbf{H}_1\mathbf{H}_2} = 75k_bT$ (d) $a_{\mathbf{H}_1\mathbf{H}_2} = 100k_bT$

Figure 4.16: Snapshots of binary mixed micelles for different head head repulsion values. As $a_{\mathbf{H}_1\mathbf{H}_2}$ increases, domains become more distinct. However, even for high repulsion values, the separation is not sharp and single surfactants can be found in the unlike domain.

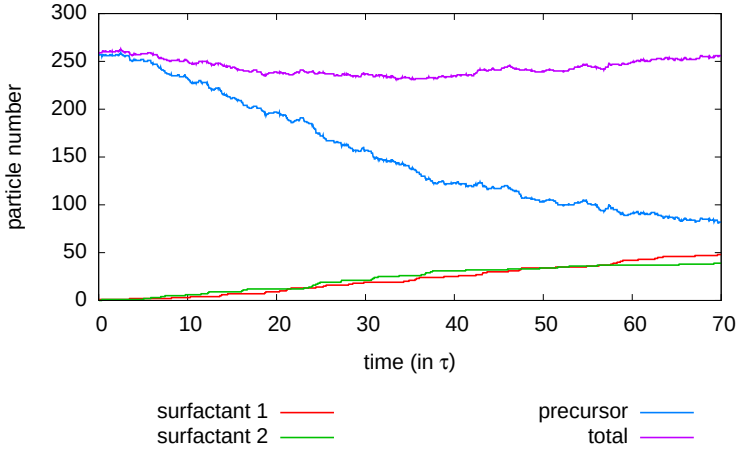

Figure 4.17: Number of surfactants and precursors against time. Surfactant concentration grows linear in time, while the number of precursors decreases. The graphs of surfactant concentration (type 1 and 2) follow each other as a result of the cross-catalytic coupling. The total number of of precursors and surfactants is approximately constant.

4.18 shows snapshot of a typical micellar fission event. As expected, in the absence of domain formation, surfactants are distributed homogeneously among the two micelles.

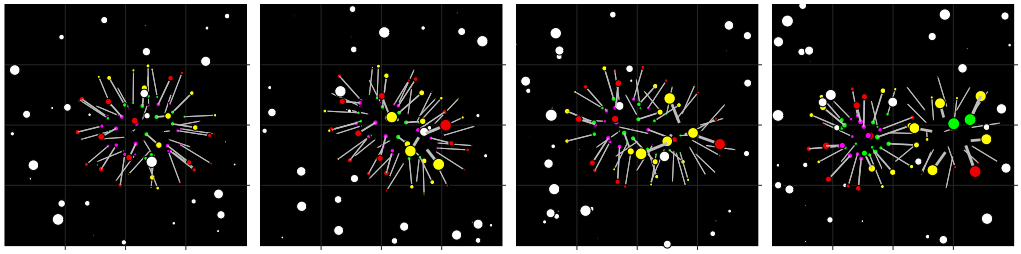

Figure 4.18: Fission of a mixed micelle of cross-catalytic amphiphiles with high mutual head repulsion ($a_{\mathbf{H}_1\mathbf{H}_2} = 25k_bT$). Snapshots are shown for $t = 82.5\tau$, $t = 85\tau$, $t = 87.5\tau$, and $t = 90\tau$. The two daughter micelles have approximately equal surfactant composition.

4.3.2 Strong tail repulsions

Discussions with experimentalists [60] clearified, that domain formation (at least on vesicles) is mainly due to the surfactant tails: Kinks in the comparatively long hydrocarbon chains can hinder the close stacking with outstreched chains. This leads to reduced van-der-Waals forces between the tails. We mimicked this phenomenon in the second parameter set by setting all head interactions equal ($\phi_{\mathbf{H}_1\mathbf{H}_2} = \phi_{\mathbf{HH}}$) and using pure repulsive tail interactions (without any attractive part). $a_{\mathbf{T}_1\mathbf{T}_2}$ has been set to 12.5, $r^c_{\mathbf{T}_1\mathbf{T}_2}$ has been varied from $0.5r_c$ to $1.0r_c$. Again, we initialized the system with a mixed micelle of 15 surfactants of each type and followed the evolution

of local heterogeneity. Figure 4.19 shows the evolution of local heterogeneity $H_L(t)$ for different tail interactions, snapshots of the system for different interaction forces and times are shown in figure 4.20. Both from figure 4.19 and 4.20, we can see that

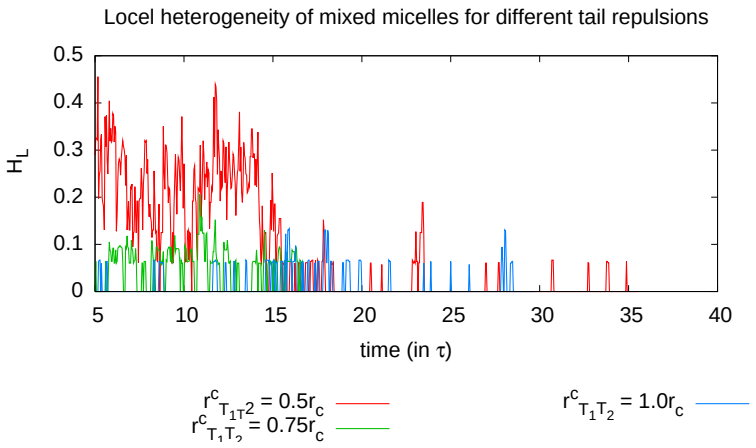

Figure 4.19: Localized Shannon entrogy H_L against time for different tail repulsion parameters $r^c_{\mathbf{T}_1\mathbf{T}_2}$. For all repulsions H_L detects a strong domain formation. Only the time needed for domain to form differs: the closer $r^c_{\mathbf{T}_1\mathbf{T}_2}$ resembles $r^c_{\mathbf{TT}}$, the longer it takes for domains to form.

the surfactants form significant domains on the micelle. We find domains for all the interaction values $r^c_{\mathbf{T}_1\mathbf{T}_2}$ between $0.5r_c$ and $1.0r_c$. Only the time needed for domains to form differs and is longest for $r^c_{\mathbf{T}_1\mathbf{T}_2} = 0.5r_c$, where the unlike tail repulsion is closest to the interaction between equal tail beads. In addition, we can see that the micelle deforms after domains have formed (figure 4.20(d) and (e)): the spherical micelles become elongated and form two centers for the respective amphiphiles. The assembly resembles two overlapping smaller micelles—one for each type of surfactant, respectively.
This observation justifies the assumption, that when growing, micelles will divide along the interface between the two domains.To test this assumption, we repeated the growth experiment of the last section with the second parameter set. We initialized a system with water ($\rho_{\mathbf{W}} = 3.0r_c^{-3}$), precursors ($\rho_{\mathbf{X}} = 0.25r_c^{-3}$) and one surfactant of type 1. We ran simulations from $t = 0\tau$ until $t = 500\tau$ and measured the number of micelles, H and H_L for the cross-catalytic growing micelle. Snapshots of the system are given in figure 4.21. The number of micelles and the evolution of global homogeneity H is shown in figure 4.22. Like in the one-component experiment (section 4.2.4) the assembly grows by incorporation of synthesized monomers. After reaching a critical size, the spherical shape becomes unstable and the micelle becomes rodlike (figure 4.21 (c)). Surfactants seperate on the surface of the assembly: the elongated shape consists of two caps each one hosting only one type of surfactant, respectively. Due to the crosscatalytic coupling, new amphiphiles are formed near the phase of the other amphiphile type. These single monomers diffuse through the unlike phase until they reach the phase of their respective type. The bigger the phases are, the more probable isolated monomers approach each other and initiate the formation of a new phase within the unlike phase.

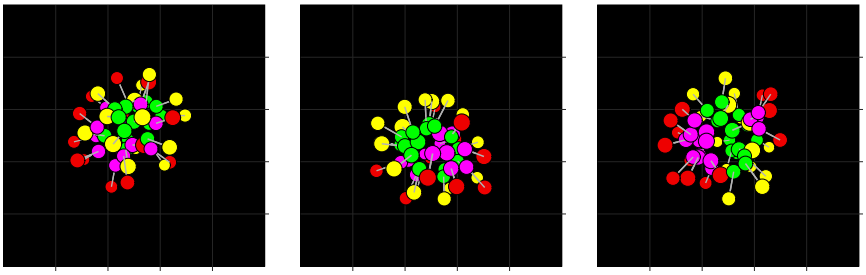

(a) $r_{\mathbf{T}_1\mathbf{T}_2} = 0.5r_c$, $t = 5\tau$

(b) $r_{\mathbf{T}_1\mathbf{T}_2} = 0.75r_c$, $t = 5\tau$

(c) $r_{\mathbf{T}_1\mathbf{T}_2} = 1.0r_c$, $t = 5\tau$

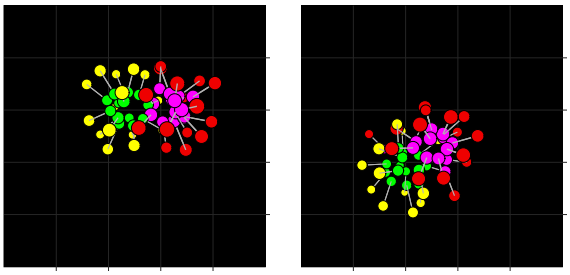

(d) $r_{\mathbf{T}_1\mathbf{T}_2} = 0.5r_c$, $t = 40\tau$

(e) $r_{\mathbf{T}_1\mathbf{T}_2} = 0.75r_c$, $t = 40\tau$

Figure 4.20: Domain formation on mixed micelles for different tail tail repulsion values. The stronger unlike tail repulsion, the faster domains form in the mixed micelle ((a) to (c)). But even for low mutual repulsion, domains form after a longer time ((d) and (e)).

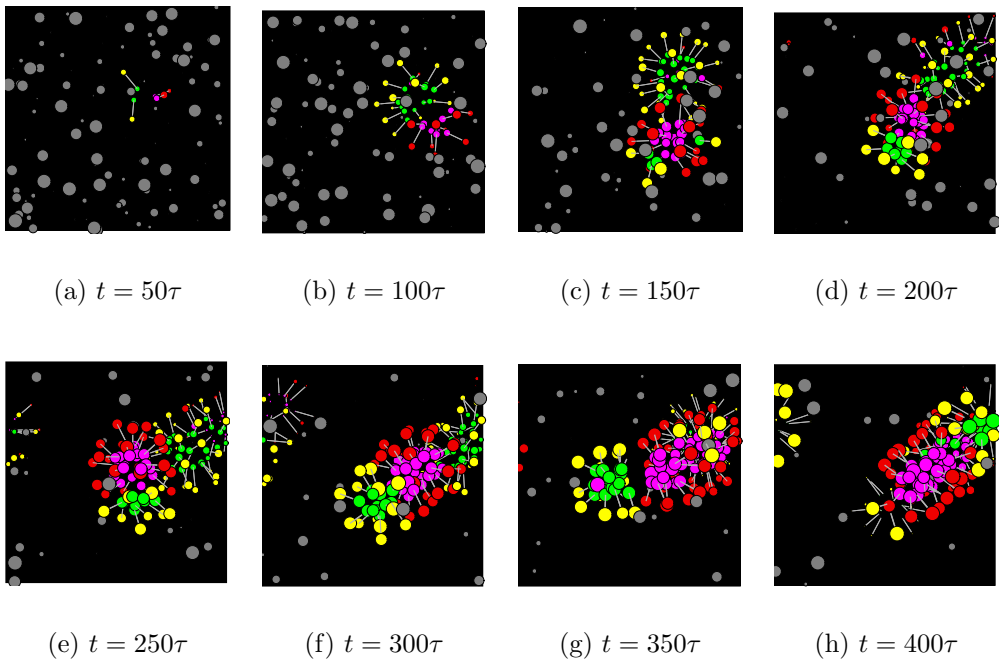

(a) $t = 50\tau$ (b) $t = 100\tau$ (c) $t = 150\tau$ (d) $t = 200\tau$

(e) $t = 250\tau$ (f) $t = 300\tau$ (g) $t = 350\tau$ (h) $t = 400\tau$

Figure 4.21: Growth of a mixed micelle with cross-acatlytic surfactants. The assembly elongates into a rodlike shape and exhibits clear phase separation of the two constituent surfactants. Eventually, the rodlike assembly devides into daughter micelles which differ in surfactant composition.

In the mixed system, the elongated form is more stable than the one-component system: the rodlike micelle elongates far beyond the size, where the one-component micelle divided (figure 4.21 (d) and (e)). As the parameter sets differ only in the absent attractive force between unlike tails, it seems reasonable to relate this stabilization to the reduced overall attraction. However, this explanation seems counterintuitive, as the absent attraction between domains should even promote fission along the domain boundary. From figure 4.22 one can see that the elongated aggregate finally splits. Compared to the one-component system, however, the micellar division is not a sharp event. Instead, the aggregate fluctuates, which leads to an oscillation in the (discretely) measured number of micelles. As a consequence, $H(t)$ fluctuates too (as the value is weighed by size and number of micelles). Nevertheless, its drastic decrease witnesses that fission occurs along the domain boundaries and that the resulting daughters differ in their composition. More detailed observations showed that the seperation along the interface is very accurate: the only defects from complete seperation of amphiphile types among the daughter micelles is caused by newly synthesized monomers that did not diffuse to the other domain before the fission was completed.

4.3.3 Summary

In this section, we analyzed micelles of surfactants with cross catalytic activity. The cross catalytic network we have choosen can be understood as a minimal scenario

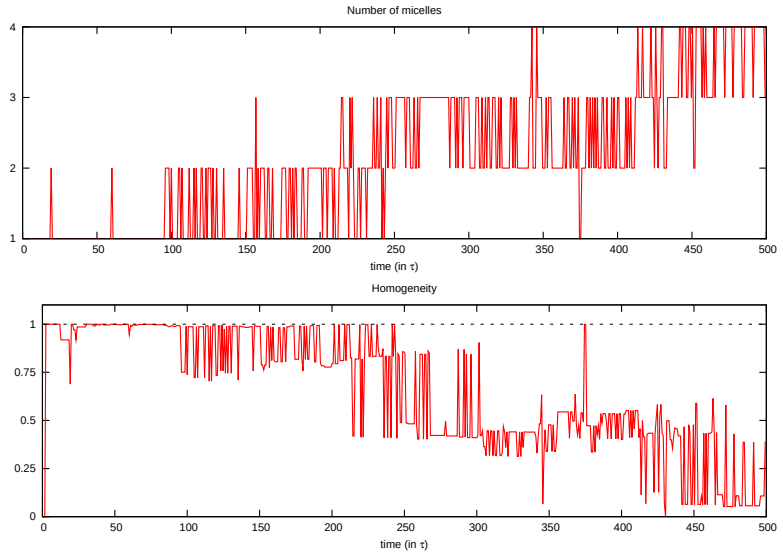

Figure 4.22: Heterogeneity and number of micelles in the Lipid World system with strong mutual head and weak mutual tail repulsions. Using these interactions, we find domain formation on the surface of the micelles. The micellar division occurs along the domain interface, which leads to a heterogeneous composition of surfactants within the daughter micelles.

of the Lipid World theory. We were especially interested in domain formation in mixed amphiphilic aggregates, as domains are known to play a possible role in fission scenarios. We analyzed the influence of different parameter sets on the formation of domains. We saw that the main interaction value responsible for domain formation is the interaction between mutual surfactant tail beads. This is in agreement with experimental results, but differs from the GARD model of the Lipid World, where tail parts are supposed to be identical for all amphiphiles.

4.4 The Los Alamos bug

We modeled the Los Alamos bug with the following components: water, surfactant precursor, surfactant, sensitizer, PNA templates and PNA precursors. Water (**W**) and sensitizer (**X**) are single DPD particles. Surfactants are modeled as amphiphilic dimers: one hydrophilic head (**H**) and one hydrophobic tail particle (**T**) connected by a covalent bond. Surfactant precursors are dimers of two hydrophobic particles (**T** − **T**). Two different representations have been used to model PNA templates: once, we connected hydrophilic bases (**A** and **B**) to an interconnected backbone of hydrophobic particles (**P**), second, we connected hydrophobic anchors to a hydrophilic strand of PNA bases. The first alternative seems closer to reality, while the latter simplifies the capture of certain PNA properties. In both cases, we used a strand of four interconnected dimers for the template and two interconnected dimers for the precursors.

This leaves us with seven different types of particles, for which we need to define 28 mutual interactions. We start by specifying parameters for water, amphiphile head and tail particles and then choose the missing interactions according to these parameters. For water, we adopt the interaction parameters proposed by Groot and Warren—$a_{\mathbf{WW}} = 25, r_c = 1.0$—which have become standard throughout the literature[38]. In order to model surfactants which form micelles (surfactant parameter $N_s < 1/3$), we mimick a conical shape by $a_{\mathbf{HH}} = 37.5, r_c = 1.5$ and $a_{\mathbf{TT}} = 25, r_c \approx 0.4$. For the tail tail interactions, however, we generalize the interaction as announced in section 3: $\mathbf{F_{TT}}$ is a stepwise linear function defined by the points $(0, 25), (0.5, -3.75), (0.75, -1.875),$ and $(1.5, 0)$. Head tail repulsion is set to $a_{\mathbf{HT}} = 37.5, r_c = 1.5$ and the spring force between two interconnected head and tail particles is $b = 125, r_b = 0.5$.

PNA is modeled as interconnected amphiphiles, thus the interaction parameters of P are equal to those of surfactant tail particles, and **A** and **B** interact like surfactant head particles. The affinity of the two complementary bases (**A** and **B**) is modeled by a second attractive interaction—namely a stepwise linear force going through the points $(0, 37.5), (0.5, -10), (0.75, -5),$ and $(1.5, 0)$. Bonds of the PNA backbone have the parameters $b = 125, r_b = 1.0$ both in the case of interconnected backbone particles **P** as well as interconnected bases **A** and **B**. Finally, the sensitizer is a hydrophobic particle with interaction parameters that allow it to diffuse freely through the hydrophobic phase. Table 4.3 summarizes the choosen set of parameters, figure 4.23 shows the resulting interaction potentials.

We used this model to study various aspects of the life cycle of the Los Alamos bug as depicted in figure 1.3. In particular, our simulations address the spontaneous formation of protocells (figure 1.3.1-2), the incorporation of resources (1.3.2-3), the metabolic growth of the protocell (1.3.4-5), template reproduction, and finally fission into two daughter cells (1.3.5-6). All simulations have been performed in three dimensional space with periodic boundaries. σ was set to 3, γ to 4.5 (equilibrium temperature $1 k_b T$).

particles	a_ij	r_c
hydrophile, hydrophile	25	1.0
hydrophile, hydrophobe	27.5	1.5
hydrophobe, hydrophobe	(1)	

particles	a_ij	r_c
H, **H**	37.5	1.5
A, **A**	37.5	1.5
B, **B**	37.5	1.5
A, **B**	(2)	
X, **T**	25	0.5
X, **X**	25	1.0

Table 4.3: Generic and specialized interactions for the different particle pairs in our simulation. Interactions for two hydrophilic particles (1) are described by stepwise linear functions throught the points $(0, 25), (0.5, -3.75), (0.75, -1.875)$, and $(1.5, 0)$. Likewise, complementary bases (2) interact by a stepwise linear function defined by the points $(0, 37.5), (0.5, -10), (0.75, -5)$, and $(1.5, 0)$.

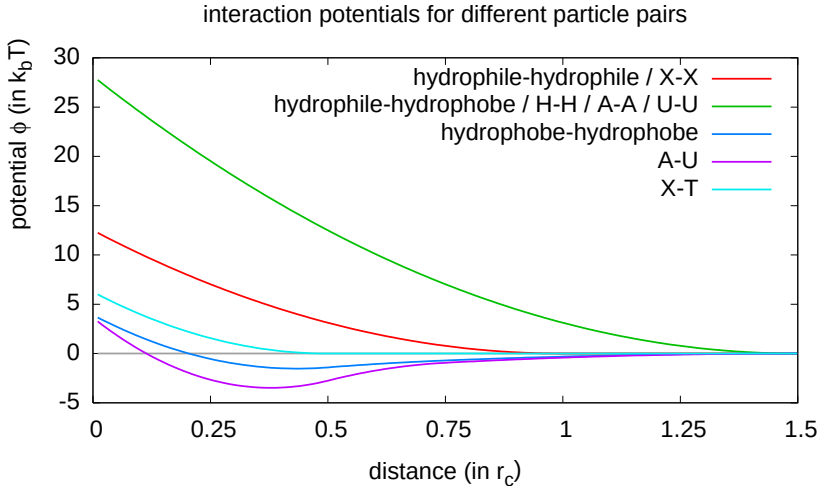

Figure 4.23: Interaction potentials resulting from the parameter set denoted in table 4.3.

4.4.1 Self-assembly of the protocell

Using 20 surfactant molecules, 8 sensitizer particles, one PNA polymer consisting of 4 backbone and 4 base particles and 1225 water particles, we observed the spontaneous self-assembly of a protocell (see figure 4.24). Thanks to the small size of our system, the aggregation happens within a very short period: after 30 time units (750 iterations), we already find a complete self-assempled protocell. This protocell is stable and shows the desired features: sensitizer resides in the interior of the micelle, while PNA sticks at its surface with the head beads exposed to the aqueous phase.

4.4.2 Incorporation of resources

We now start to "feed" the protocell with metabolic resources. As a proof of concept, we first feed the system with surfactant precursors only. In the region opposite to the protocell, we exchange water particles with surfactant precursors (two water

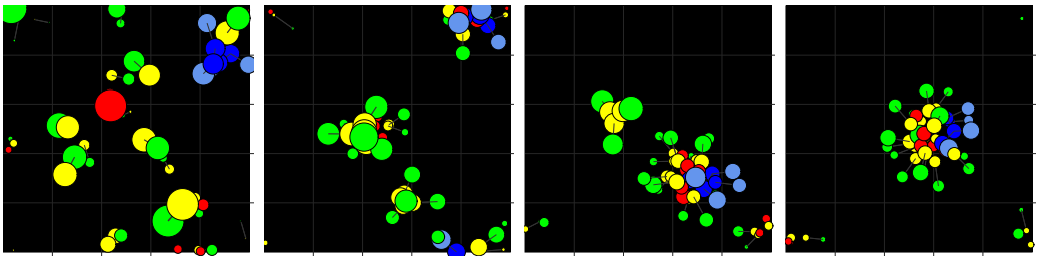

Figure 4.24: Self-assembly of the protocell. The diagrams show the state of the system at times (a) $t = 0\tau$, (b) $t = 10\tau$, (c) $t = 20\tau$, and (d) $t = 30\tau$. Surfactants are shown in green (head bead) and yellow (tail), sensitizers are shown in red, PNA backbone in dark blue and PNA nucleotides in light blue.

beads with one precursor molecule). This particle exchange occurs with probability 5×10^{-5} per particle pair and time unit within a spherical region of radius $3r_c$ (volume $\approx 113.1r_c^3$) – thus we have an overall exchange rate of $\approx 1.696 \times 10^{-2}$ surfactants per time unit.

Because of their hydrophobic nature the precursor molecules tend to agglomerate into droplets. The diffusion of such droplets is slower the bigger they are. This initiates a positive feedback: the bigger the droplets, the slower they diffuse out of the exchange zone. The slower they diffuse, the more likely they agglomerate additional precursors. Thus, there must be an optimal exchange rate, that leads to a high support rate of precursors. In general, when we increase the radius of the exchange area but keep the effective rate constant, the agglutination of precursors is reduced. However, we want to keep the exchange region small, in order to prevent the non-continuous exchange events from disturbing the kinetics of the protocell. Thus, we consider $3r_c$ the maximal range of the exchange region. We both increased and decreased the rate the precursor support. 5×10^{-5} seemed to be the optimum, for which droplets of precursor molecules assemble are provided with reasonable speed, but are still small enough to diffuse. With this value, we measured precursor droplets of around 15 molecules.

Once in the vicinity of a protocell, precursor droplets are immediately absorbed by the micelle, because of their reduced chemical potential in the hydrophobic interior of the micelle compared to the aqeous phase. Figure 4.25 shows an incorporation of a procursor droplet into the micelle

4.4.3 Metabolism

Next, we introduce the part of the metabolism that transforms surfactant precursors into actual surfactants. In the real chemical implementation of the Los Alamos bug, the precursors are fatty acid esters. The surfactant breaks the ester bond thereby producing fatty acid—the surfactant—and some aromatic molecule—which is considered waste. Disregarding the production of waste, we model this reaction by the scheme

$$\mathbf{T} - \mathbf{T} \longrightarrow \mathbf{H} - \mathbf{T} \tag{4.14}$$

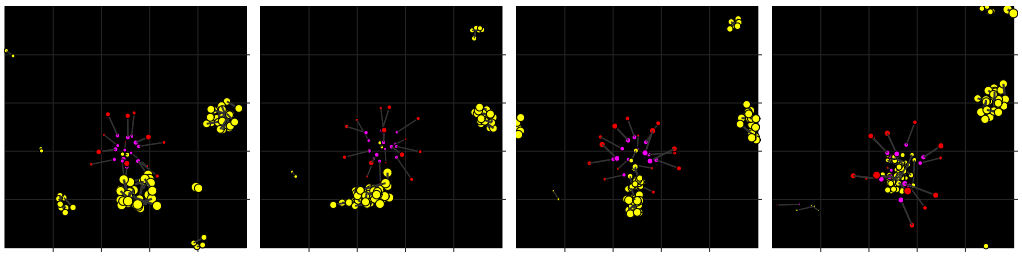

Figure 4.25: Incorporation of precursors into the micelle. Due to their hydrophobic nature, precursors aggregate into droplets, that get incorporated into the micelle as a whole. The system is shown for (a) $t = 27.5\tau$, (b) $t = 30\tau$, (c) $t = 32.5\tau$, and (d) $t = 35\tau$. Surfactants are shown in purple (tails) and red (heads), prucursor is shown in yellow.

which reflects, that both parts of the ester are hydrophobic, while the resulting surfactant is an amphiphile. For simplicity, the spontanous reaction rate is set to 0. The sensitizer acts as a catalyst with catalytic radius of $1.0r_c$ and a maximal catalytic rate of $1.0\tau^{-1}$. This ensures that precursor transformation only occurs in the vicinity of sensitizers, hence in the interior of the micelle. Using a protocell with eight sensitizers, we observe an immediate transformation of precursors once they are absorbed. The transformation of 15 surfactants happens in less than 2 time units on average.

We also experimented with a scenario where the catalytic activity of the sensitizer can interactively be turned on and off. This reflects the photoactivity of the sensitizer which uses light energy to enhance the reaction. A controllable light source can regulate the kinetics of the metabolism in the following way: when light is turned off, the protocell collects precursors in its interior. After light is turned on, the collected precursors are transformed instantaneously into surfactants. Thus, when regulated by light bursts, the metabolic turnover is steplike rather than smooth. However, the effect of this lightswitch is less suspected: Because of the droplet formation of precursors, the micelle grows in spurts even if the sensitizer catalyzes permanently.

In a later study, we will couple the functioning of the sensitizer with PNA: the catalyst rate will depend on the amount and type of nearby bases. Applying this coupling, the PNA will actually affect in the growth rate of the protocell—thus turning the template into a real genome.

4.4.4 Genome replication

Replication of the genome is divided in two consecutive steps: hybridization and polymerization. Hybridization denotes the alignment of short PNA precursors along the template of the existing PNA strand. Polymerization is the reaction the turns aligned precursors into an actual PNA strand (see figure 4.26).

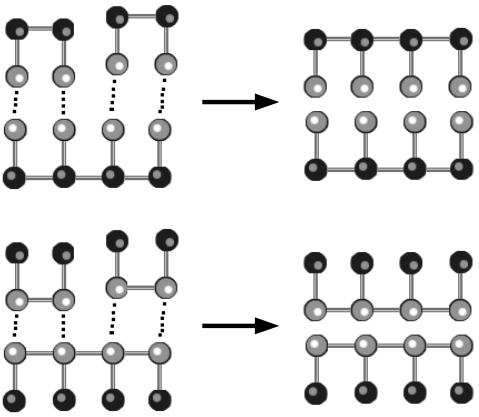

Figure 4.26: Schematic of hybridization and polymerization for the two different PNA represenations. In the first case, the PNA backbone is modeled as a strand of interconnected beads, with nucleotides attached to it; in the second case, bases are interconnected and hydrophobic anchors are attached. In both cases, complementary bases must align properly, before they can polymerize into a double strand.

Hybridization

The simplistic representation of nucleotides by one DPD bead only makes the hybridization process somewhat hard to capture. Therefore, we tried several representations of PNA (as described in section 4.4) as well as several mechanisms of hybridization. In the real system, hybridization is due to hydrogen bonds between complementary bases. In our toy model, we represent these hydrogen bonds by attractive forces between nucleotide beads. Two different types for these attractions have been probed: directed and undirected attraction.

Undirected force The undirected attraction between complementary nucleotides is achieved by our generalized potential functions with the parameters listed in table 4.3 for $\mathbf{A}-\mathbf{A}$, $\mathbf{A}-\mathbf{B}$ and $\mathbf{B}-\mathbf{B}$. Note that these interactions are only attractive for complementary bases, otherwise purely repulsive.

Directed force In this variant, the attraction depends on the angle between the two nucleotides with respect to their backbone (in case of connected anchors) or anchor particles (in case of connected bases). In both cases, the attraction is strongest perpendicular to the PNA strand, negative tangential to the strand and negative in the backward direction. The exact definition of the attraction reads:

$$F_{ij}^{H} = a_{ij}^{H}\omega^{R}(r_{ij})\,\langle n_{ij}, n_{ik}\rangle \tag{4.15}$$

where k is the non-nucleic bead bonded to i. Appart from this, the interaction is described by the potential for $\mathbf{A}-\mathbf{A}$, no matter which nucleotides interact.
We tested these interactions for both representations of the PNA molecule. We initialized a system with a micelle of 22 surfactants and two PNA strands—one containing only bases of type **A**, the other only bases of type **B**—in its vicinity. In all scenarios, both PNA strands first attached to the micelle and then diffuse

on its surface eventually feeling their vicinity. Actual hybridization occurred only in the case of the undirected attraction—no matter which PNA representation we used. The problem with directed attraction, in the way we implemented it, is that the bonds between bases and backbones arrange radial to the micelle. Thus, two strands are usually outlaid perpendicular to these bonds, and the attractive force between the strands is therefore zero.
Using undirected attraction, we achieved more promising results. However, only in the case of connected bases (PNA representation II), we could observe a proper alignment of the complementary strands (see figure 4.27). With the parameters we used, 4.6% of the simulated time, we found a proper base pairing between the complementary strands. By fine tuning the attraction parameters, however, we expect to achieve a far more reliable hybridization.

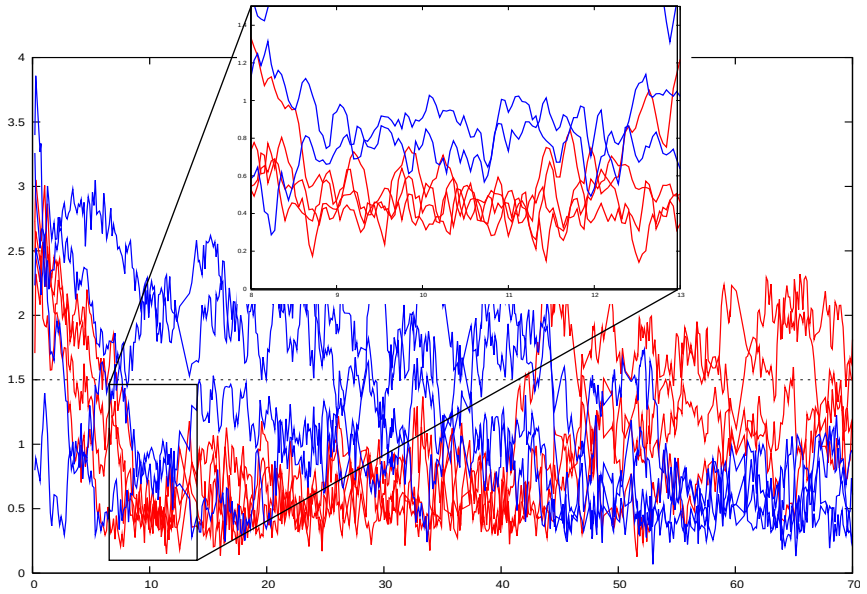

Figure 4.27: Distances between complementary bases of two attracting PNA strands. Between $t = 10\tau$ and $t = 40\tau$ we find a hybridization between the two strands (red lines). Between $t = 55\tau$ and $t = 70\tau$ the strands change their orientation and align vice versa, but in this case, the base pairing is less significant. Proper alignment of the two strands only occurs between $t = 9\tau$ and $t = 12\tau$.

For the undirected attraction and interconnected bases, we compared hybridization of PNA templates in water opposed to the micellar surface. It turned out, that the strands never hybridized properly in water. Due to the hydrophobic nature of the backbone, the backbone is more tangeld then at the surface of the micelle (compare the configuration of PNA in figures 4.24 (a) and (d)).
The problem we encountered with undirected attraction is the following: In the real system, only two bases can align to each other (at least in the Watson-Crick pairing). Once aligned, the hydrogen bond is saturated and no other nucleotide can hybridize. Undirected forces, on the other side, behave more like Coulomb forces: several complementary bases can be attracted by a single nucleotide. This significantly violates the biological mechanism and is the main reason that a proper alignment. One possibility to overcome this problem is to introduce explicit hydrogen bonds in

addition to the attractive force: when two complementary bases approach each other, a bond is formed with a relatively high probability. A backward reaction breaks this bond with the same probability and allows to overcome temporary misspairing of the strands. During this reaction, the bases actually change their type from an unbonded to a bonded state. By making only unbonded bases attractive, it seems possible to prevent the discribed disadvantages of undirected attraction. Further simulations have to be performed using this mechanism.

Another difficulty for proper alignment is the possibility of self-pairing of bases in a single strand. While this might also be an issue in the real system, where PNA can form loops in a single strand, it occurs much more likely in our current PNA representation. Consider a template of with the nucleotide sequence $\mathbf{A}-\mathbf{A}-\mathbf{B}$: the first and third base are complementary and will attract each other forcing the template to bend. The situation gets even worse, once explicit hydrogen bonds are introduced, because the self-bonded strand will no linger attract a nearby second strand. We could observe, that self-binding makes the hybridization effectively impossible, simply because it is more likely to be in the vicinity of a base of the same strand than of another strand. So far, we prevented self-binding by restricting our analysis to only a subset of possible templates—those where all bases within one strand are of the same type. While this successfully prevents self-binding, it is certainly not satisfying. A better way to prevent self-binding, would be to introduce stiffness in the PNA backbone: we can increase the potential energy of a strand, when it is twisted. Such bending potentials are common in MD simulations and have already been used in DPD studies of phospholipids [61].

Polymerization

Polymerization is the reaction, by which hybridized PNA dimers connect to longer oligomers and eventually form a complementary copy of the whole PNA template. So far, we modeled polymerization only for the second representation of PNA, as it was the only one for which we achieved reliable hybridization.

We model this polymerization reaction straight forward with the synthesis

$$\mathbf{A}+\mathbf{A} \longrightarrow \mathbf{A}-\mathbf{A} \tag{4.16}$$

$$\mathbf{B}+\mathbf{B} \longrightarrow \mathbf{B}-\mathbf{B} \tag{4.17}$$

We restrict the maximal number of bonds per base bead to 3 to prohibit the formation of branches.

We compared two implementations of this reaction: in the first scenario, we set the spontaneous reaction rate to 0.1 in a reaction range of $1.0r_c$. In the second scenario, we set the spontanous rate to 0 and declared the complementary base as catalyst with catalyst rate 1.0 in a range od radius $0.5r_c$. The latter implementation is intented to increase the reliability of PNA replication, as the probability of polymerization depends on proper alignment. However, we could not find significant differences between the two implementations. This might be due to the fact, that actual hybridization happened so far only for very short times.

4.4.5 Division

The last step in the life cycle of the Los Alamos bug is the fission of the grown organism into two daughter cells. With the parameter set we used, this fission process is generic for all growth scenarios.
To study the division kinetics, we initialize the system with a spherical micelle of 20 monomers and supply single amphiphiles to the system. The micelle grows by incorporating monomers, until—at an aggregation number around 35 monomers—the spherical shape becomes unstable and the micelle starts to elongate into a rodlike structure. Elongation continues until at aggregation numbers between 50 and 60 the ratio of long to short axis exceeds 2:1. A gap forms in the center of the micelle and initiates a fission process, after which the micelle has dublicated. Daughter micelles have an aggregation number between 25 and 30.
In the scenario of the Los Alamos bug, monomers are not supplied contineously but in spurts. We simulated the fission scenario with a system initiallized with one micelle of 15 monomers, 4 to 8 sensitizer beads in its interior and the reaction and particle exchange described in section 4.4.3, but without genetic template. We found that the division is still similar to the one outlined above: the intially spherical micelle elongates and splits into two spherical daughter cells, once the critical axis ration exceeds 2:1. In our experiments, the incorporation of a single precursor droplet already resulted into division.
We could observe several problems involved in the fission process, that might also be issues in the real system. One issue is the equal distribution of sensitizers between the two daughter cells: using only 4 sensitizers, we observed fission results, where one micelle hosted all sensitizers, the other one had no sensitizers. This is an example of a failed reproduction, as only one daughter cell is able to reproduce further. In our simulation, the “infertile” daughter cell continued to incorporate precursors, thereby reducing the amount of accessible precursors for the “fertile” daughter cell.
The equal distribution of PNA strands is a second issue in the life cycle of the Los Alamos bug. We performed simulations with a system of 20 surfactants, 4 sensitizers and two PNA strands of 4 A-bases. Using only equal bases prevented the hybridisation of the strands on the surface of the micelle. In our simulations, we could never observe, that the two strands are on the same micelle, whereas the other micelle lost its genome. However, we could observe the problem that a single PNA strand connects the two daughter cells after an otherwise successful division, resulting in “’Siamese twins’.

Chapter 5

Discussion

In this work we have applied the simulation method dissipative particle dynamics (DPD) to micellar systems in the context of protocellular scenarios. We have reported relevant results of equilibrium micellar systems, obtained from calculations of formal reaction kinetics. We calibrated the length and time scale of DPD to the physical scales of a real systems (sodium heptylsulfate). We could show, that DPD operates on appropriate length and time scales to analyse micellar kinetics.
We pointed out strategies to calibrate the DPD interaction parameters to system parameters obtained from the equilibrium calculations. However, we have not been able to calibrate our system in the given time. Our model is therefore a toy model, that catches some features of micellar systems cannot reproduce all relevant ascepts of the real system. In our simulation, we find the aggregation of surfactants into spherical micelles with typical aggregation numbers between 25 and 35 surfactants. However, we could not model the dissociation of single surfactants from supramolecular aggregates. As a consequence, we cannot obtain realistic micellar size distributions with the coexistance of micelles and monomers. Therefore, some of the results obtained from simulations are clearly artefacts of the parameters used.
We applied our model to two scenarios from the early life and protocell literature: the Lipid World and the Los Alamos bug. While both of them consider micelles as embodiments for proto-organisms, they substantially differ in the way, micellar growth and division—necessary conditions for the replication of the cell—is achieved. In the Lipid World scenario, micelles grow by incorpotation of *individual* surfactants synthesized from precursors due a catalytic reaction enhanced by nearby surfactants in the micellar phase. The Los Alamos bug, on the other side, grows by incorporating droplets of precursors, that are transformed into surfactants by light energy *in the interior* of the micelle.

5.1 Micellar kinetics

In our simulations, we observed growth and division of micelles for both systems. However, we have to discuss the impact of model artefacts on the outcome of our simulations. Doing so, we obtain evidence that only the kinetic pathway of the Los Alamos bug—incorporation of precursors in spurts— is likely to allow growth and division of micelles. Our argument is based on formal reaction kinetics based on the

Becker-Döring scheme (section 2.2.2).
We consider a micelle S_N in equilibrium size (aggregation number N). If we drive this system out of equilibrium, growth of the micelle happens if and only if the inflow of surfactants into the micelle is greater than the outflow of monomers that dissociate, otherwise the micelle could respond to every incorporation of precursors with the dissociation of another monomer to maintain its equilibrium size. As the dissociation rate of monomers depends only on the stability of the micellar aggregate, not on the surfactant concentration in bulk phase, we assume that the equilibrium rate constant k^- also applies for the non-equilibrium system. The inflow consists of two seperate steps: synthesis and incorporation.
For the Lipid World, we assume that the synthesis is the rate limiting factor and treat association as an instantanious process. With this assumption, inflow and outflow reduce to

$$X \xrightarrow{k_X} S_n \xrightarrow{k^-} S \tag{5.1}$$

where k_X is the kinetic constant of precursor synthesis and k^- the dissociation rate of monomers. The condition that the inflow must be higher than the outflow gives:

$$k_X[X] > k^- \Longleftrightarrow [X] > \frac{k^-}{k_X} \tag{5.2}$$

We can now estimate the necessary minimal precursor concentration to drive the micellar system out of its equilibrium. Table 2.1 lists dissociation rates for several sodium alcylsulfate surfactants. More values can be found in [25]. All of them lie inbetween $6 \times 10^4 s^{-1}$ and $1.32 \times 10^9 s^{-1}$, whereby the value is bigger the shorter the length of the hydrocarbon chain, as their smaller hydrophobic effect results in less stable micelles. We choose $1 \times 10^4 s^{-1}$ as a lower bound for the dissociation rate.
Bachmann et al. [3] measured the catalytic production rate of sodium caprilate from ethylcaprilate in the presence of caprilate micelles. They estimated the bimolecular rate constant of $0.19 M^{-1}s^{-1}$. Let us assume that this is a representative value for comparable catalytic reactions. To be conservative, we choose $k_X = 1 M^{-1}s^{-1}$. Using equation 5.2, we find $[X] > 10^4 M$. To illustrate how ridiculous this concentration value is, we mention that water has a concentration of approximately $55M$—thus, our precursor would need to have less than 1/20 of the molecular volume of water, to obtain such high molar values. Even then, the precursor would be pure, not in aqueous solution.
All estimations in the previous calculation have been conservative, thus even higher precursor concentrations would be needed. The weak point in this calculation is maybe the procurser synthesis rate, that might differ for other reactants. Thus, we repeat the calculation above and solve it for k_X to obtain the necessary reaction rate for more realistic precursor concentrations. For concentrations between $0.01M$ and $1M$ we obtain necessary minimal synthesis rates k_X between $10^3 M^{-1}s^{-1}$ and $10^6 M^{-1}s^{-1}$.
The situation might be improved for other types of surfactants (e. g. phospholipids) that form more stable aggregates so that their dissociation rate k^- is smaller. Further calculations on this could be done for several kinds of surfactants. However, the above calculations render the micellar growth scenario proposed in the Lipid World highly inprobable. For most reasonable prebiotic scenarios, only a minor fraction of

surfactant will be micellized. The inheritable potential of a compositional genome based on micelles is jeopardized by the high rates of monomer exchange with the bulk phase. The situation is even worse, if one further takes the slow relaxation time τ_2 into account (see section 2.2.2): the lifetime of typical micelles, after which it dissociates into monomers, is inbetween milliseconds and minutes. That said, we can only come to the conclusion that *the Lipid World much likely resembles a well mixed reaction system with the occasional formation of micelles*. While these micelles are likely to govern the overall reaction rate due to their catalytic effect, it is unlikely that they are able to store inheritable information. Thus, in terms of information, little is achieved by the organizational complexity of the micellar system.

Let us repeat the above considerations for the growth scenario of the Los Alamos bug. Again, the limiting factor of micellar growth is the production rate of new surfactants and we can neglect the association rate. This time, however, to neglect the incorporation is not a simplifaction of the real kinetics, because we can control the surfactant turnover by the light energy to which we expose the system—that is, we can trigger the reaction once the micelle incorporated enough precursors, no matter how fast this process happened.

The effective turnover of surfactant precursors into new surfactants is influenced by several processes: diffusion of the precursor towards the sensitizer, electron transport from the sensitizer onto the precursor, cleavage of an ester bond in the precursor, and others. Bankö and Rasmussen estimate a maximal production rate between 10^4 and $10^7 M^{-1} s^{-1}$ [62] for the bimolecular reaction

$$\text{precursor } \mathbf{P} + \text{sensitizer } \mathbf{X} \longrightarrow \text{surfactant } \mathbf{S} + \text{sensitizer } \mathbf{X} \tag{5.3}$$

Apart from the significantly higher reaction rate, the precursor is not in solution but concentrated in the interior of the micelle, thus $[P]$ is supposed to be in the range of $1M$. By increasing the number of precursors inside the micelle, one can increase the overall turnover. Thus, the turnover rate is expected to exceed the dissociation rate. Apart from rate considerations, the hydrophobic loading of micelles stabilizes their shape. Before the transformation of precursors, the micelle is in its equilibrium size. This size is greater, because the hydrophobic core increases the radius of the assembly, thereby allowing more amphiphiles to surround it. Once new surfactants are synthesized, the assembly rearranges to a shape that allows most surfactants to anchor at the surface of the hydrophobic core. Similar phenomena are well known in the study of detergents. This effect would even stabilize rodlike shapes until all precursors are transformed. When this happened, the aggregate looses its stability and will dissociate into several micellar aggregates.

5.2 Lipid World

Despite the problems that the calculations of the last paragraph impose on the Lipid World theory, we discuss the implications of our simulation results. These results affect the Lipid World theory for systems whose growth kinetics are accurately described by Lancet et al.—i. e. where monomer dissociation is small. As we

have pointed out (section 1.1), domain formation is the main feature not taken into account by the mathematical model of Segré et al.
In section 4.3 we modeled a minimal system of two cross-catalytic amphiphiles with our extended DPD model. For different repulsion parameters between unlike amphiphiles, we measured the local and global heterogeneity on the basis of the Shannon information of amphiphile distribution. Domain formation in our simulations could be attributed to reduced attraction between unlike surfactant tails (section4.3.2). This is in good aggreement with the theory: in experimental work of Baumgart et al. [12] domain formation is due to reduced van-der-Waals forces between kinked and outstretched hydrocarbon chains. Thus, our model qualitatively captures the expermiental results. It is interesting to mention, that the GARD model of Segré et al. [6] assumes equal tails for all surfactants and only distinguishes head groups of the molecules. However, a straightforward generalization of the GARD model that accounts for differences in the surfactant tails is imaginable, and there is no reason to assume that this generalization would affect the general findings of Segré et al.
How domain formation affects the predictions of the GARD model can be most clearly seen in section 4.3.2: the fission of the grown micelle occurs along the interface between two domains. After this divison, we find two daughter cells, each one holding one of the two cross-catalytic amphiphiles. Thus, if fission along a domain boundary occurs, each cell can contain only a part of the molecules that form the catalytic cycle and *the compositional genome is spread over several protocells*. However, as long as every single surfactant type can act as a catalyst on its own, the cells can still produce the "missing" components of the catalytic cyle.

5.3 Los Alamos bug

In section 4.4, we used our extended DPD model to simulate the Los Alamos bug. In our model, the minimal protocell consists of surfactants, precursors, sensitizers and PNA information carriers. We analyzed several aspects of the whole life cycle of the self-replicative system. Self-assembly and growth of the micellar organism has been achieved with interaction parameters similar to those used in previos experiments. Likewise, fission of the assembly followed the outcome of former simulations.
We studied the incorporation of precursor supplied by particle exchange. It was found that precursors most likely aggregate into droplets before they are incorporated into the micelle. Therefore, the amount of precursor inside the micelle grows in spurts rather than continuously. This suggests that the replication mechanism of the protocell might even work, when light energy is supplied continuously. In this case, control of the light exposure would not be necessary to regulate the replication.
We further studied the genome replication (hybridization and polymerization) of the Los Alamos bug. Due to the very simplistic representation of nucleotides by point particles, proper hybridization cannot be achieved easily. Using undirected attractive forces, we could achieve proper alignment only for less than 5% of the simulated timespan (We expect, however, that the reliability can be imporved by fine tuning the interaction parameters).
One problem we encountered with undirected attraction is the following: in the

real system, only two bases can align to each other (at least in the Watson-Crick pairing). Once aligned, the hydrogen bond is saturated and no other nucleotide can hybridize. Undirected forces, on the other side, behave like Coulomb forces: several complementary bases can be attracted by a single nucleotide. This significantly violates the biological mechanism and is the main reason why proper alignment fails in our simulations. One possibility to overcome the problem is to introduce explicit hydrogen bonds in addition to the attractive force: when two complementary bases approach each other, a bond is formed with a certain probability. A backward reaction brakes this bond with the same probability, allowing to overcome temporary missparing of the strands. During this reaction, the bases actually change their type from an unbounded to a bounded state. By making only unbounded bases attractive, it seems possible to prevent the described disadvantages of undirected attraction. Further simulations have to be performed using this mechanism.
Another difficulty to proer alignment is the possibility of self-pairing. While this might be also an issue in the real system, where PNA can form loops in a single strand, it occurs much more likely in our model, due to the current PNA representation. Consider a template with the nucleotide sequence $\mathbf{A}-\mathbf{A}-\mathbf{B}$: the first and third base are complementary and will attract each other forcing the template to bend. The situation might get even worse, once explicit hydrogen bonds are introduced, because the self-bonded strand will no longer attract a nearby second strand. We could observe that self-binding makes the hybridization effectively impossible, simply because it is more likely to be in the vicinity of a base of the same strand than of another strand. So far, we prevented self-binding by restricting our analysis to to only a bsubset of of possible templates—those where all bases are within one strand are of the same type. While this successfully prevents self-binding, it is certainly not satisfying. A better way to prevent self-binding, would be to introduce stiffness in the PNA backbone: we can increase the potential energy of a strand that is twisted. Such bending potentials are common in MD simulations and have already been used in DPD simulations of phospholipids [61].
In a later study, we want to couple the functioning of the sensitizer with the genomic information of the PNA: the catalytic rate will depend on the amount and type of nearby bases. Applying this coupling, the PNA will actually affect the growth rate of the protocell—thus turning the template into a real genome.

Concerning the dynamics of the whole system, we could make the following observations: one issue of successful protocell replication is the equal distribution of sensitizers between the two daughter cells. Using too few sensitizer molecules (4 sensitizers in a micelle of aggregation number 22), we ended up with a fission result, where only one daughter micelle hosted all sensitizers, whereas the other one hosted none. In our simulation, the infertile daughter cell continued to incorporate precursors, thereby reducing the amount of accessible precursors for the fertile daughter cell. When the infertile daughter cell grows, it looses its spherical shape as it becomes more and more droplet-like. Once it has less surfactants than are necessary to cover its surface, it becomes possible that it fuses with another, possibly fertile micelle. Thus, although the distribution of of sensitizers might not be reliable, products of failed divisions are available as nutrients for a later fission process.

The equal distribution of PNA strands is a second issue in the life cycle of the Los Alamos bug. We could observe the problem that a single PNA strand connects the two daughter cells after an otherwise successful division, resulting in "'Siamese twins'. The future of such twins mainly depends on the ability of PNA to leave one of the aggregates to get incorporated completely in the other one. With our model parameters, however, the amphiphilic character of PNA is to strong to allow the PNA strand to leave the micellar surface.

Acknowledgments

This work is part of the PACE Programmable Artificial Cell Evolution project and has been granted by the 6th European Union Framework Program under contract FP6002035 and the Deutscher Akademischer Austauschdienst DAAD.
I want to thank my supervisor Ricard V. Solé for constant support, encouraging guidance and fruitful discussions during my stay at the Complex Systems Lab. I further want to thank all members of the Lab for the joyful and inspiring atmosphere they provide. Norman Packard, Mark Bedau and Martin Hanczyc from Protolife Inc. deserve thanks for the share of experimental knowledge and the European Center for Living Technology ECLT Venice for financial support during a three week period of colaboration. Furthermore, I want to thank Steen Rasmussen and Hans-Joachim Ziock for their support and help and the Los Alamos National Laboratories for financial support during my two months colaboration at LANL. Last but not least, I want to thank Ignatio Pagonabarraga and Anders Eriksson for insightful discussions about DPD physics and calibration.

Appendix A

Implementation

The underlying mathematical model of DPD is a stochastic differential equation of Newtons third law (3.2). The basis of the computer simulation is therefore a numerical integrator of this equation. However, the special nature of the problem defines boundary conditions for reasonable algorithms and guides to specializations of the integration scheme for performance enhancements. Second, the stochastic nature of the differential equation has to be taken into account.

A.1 The Particle Space

A.1.1 Boundary Conditions

Our DPD implementation allows simulations in two and three dimensional space. Although periodic boundary conditions are mainly used in DPD simulations, the implementation allows also to study no flux boundary conditions. To provide this flexibility without messing up further calculations, we introduce the notion of positions and directions. Both are floating point vectors with two or three coordinates, respectively. By destingishing between them, we can hide the care for boundaries in the calculations: boundary conditions affect positions, but not directions. Each particle has a position. Its velocity and acceleration are directions.
Directions are ordinary two or three dimensional vectors for which we define common vector arithmetics:

$$\text{Dir} \pm \text{Dir} \rightarrow \text{Dir} \tag{A.1}$$
$$\text{Scalar} * \text{Dir} \rightarrow \text{Dir} \tag{A.2}$$
$$< \text{Dir}, \text{Dir} > \rightarrow \text{Scalar} \tag{A.3}$$
$$\text{length}(\text{Dir}) \rightarrow \text{Scalar} \tag{A.4}$$

Positions are locations in space. They are related to directions by the following operations:

$$\text{Pos} + \text{Dir} \rightarrow \text{Pos} \tag{A.5}$$
$$\text{Pos} - \text{Dir} \rightarrow \text{Pos} \tag{A.6}$$
$$\text{Pos} - \text{Pos} \rightarrow \text{Dir} \tag{A.7}$$

For periodic boundary conditions, operations A.5 and A.6 adjust the resulting vector sum to fit into the periodic boundaries in a straight forward way:

$$\begin{aligned} x &\rightarrow x \bmod \texttt{size\_x} \\ y &\rightarrow y \bmod \texttt{size\_y} \\ z &\rightarrow z \bmod \texttt{size\_z} \end{aligned}$$

Operation A.7 performs the so called *minimal image condition*: For two given positions i and j, the direction from i to the closest of all periodic images of j is returned.
For no flux boundary conditions, the operations A.5 and A.6 mirror the intermediated result at the edge. For one coordinate the adjustment reads:

$$x \rightarrow \begin{cases} -x & \text{if } x < 0 \\ 2 * \texttt{size\_x} - x & \text{if } x \geq \texttt{size\_x} \\ x & \text{else} \end{cases}$$

In this case, A.7 returns the common difference $i - j$ as direction.
The distinction between positions and directions completely hides the topology of the space. Further calculations can be performed without any respect to the underlying topology.

A.1.2 Partitioning the Space

As each particle has 4 to 6 degrees of freedom, the observed systems usually have a very high dimension (e.g. 486000 for a simulation published in [13]) The most timecritical part is the calculation of intermolecular forces.

The naive approach

A straight forward implementation of formula 3.3 results in the following algorithm – written in the python programming language as pseudo code:

```
for i in space :
    i.force = 0
    for j in space :
        j.force += physics.pairwise_force(i,j)
```

The runtime of both outer and inner loop are $O(N) = O(C * S)$ where C specifies particle concentration and S the size of the system. Hence, the overall performance of the naive approach is $O(N^2) = O(C^2 * S^2)$

Profit from cutoff

Taking into account the cutoff radius of the pairwise potential functions (equation 3.7) leads to an algorithm that is quadratic in particle concentration,but only linear in the number of particles. The particle space is partitioned into a grid where each field has a size slightly greater than the cutoff distance. Each field can hold an

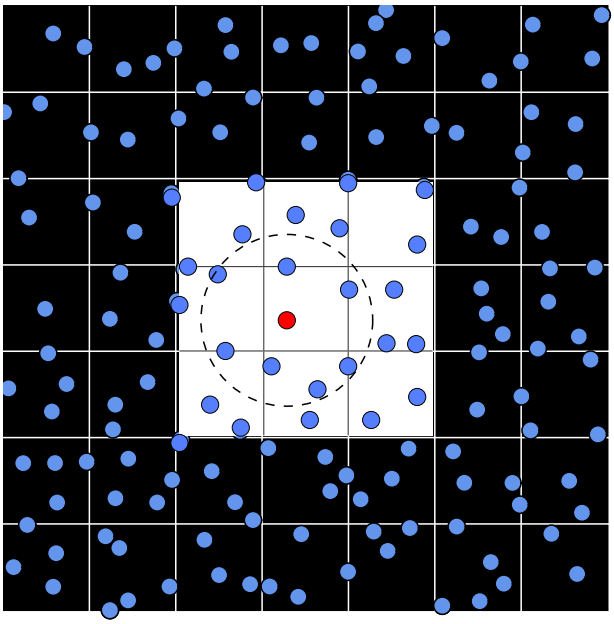

Figure A.1: The reaction space is partitioned into a grid with field size slightly above the cutoff distance. Interactions only occur between particles within this cutoff radius (dashed circle). Therefore, only particles within a Moore neighborhood (white box) have to be considered. In this particular example, only 24 instead of 122 particles have to be checked as potential interaction partners. 7 of them are actual neighbors.

arbitrary number of references to particles in a list. Figure A.1 shows an example of a grid configuration. During initialization, neighbors are determined for every field (with respect to the choosen boundary conditions). This information is used to speed up the lookup of particle neighborhoods. To determine partners for interaction, the algorithm only needs to consult the Moore neighborhood of a particle (9 fields in 2 dimensions, 27 fields in 3 dimensions):

```
for i in space :
    i.force = 0
    for j in space.neighbors(i) :
        if (i.pos-j.pos).length() < physics.cutoff :
            i.force += physics.pairwise_force(i,j)
```

Thereby, `space.neighbors` is an iterator that successively yields all particles in the Moore neighborhood of a particle. The performance of the outer loop is $O(N)$, whereas the one of the inner loop is only $O(C)$. As $C = N/S$, the total performance of this algorithm is $O(C * S) = O(N^2/S)$. This procedure is commonly known as *linked cell* algorithm in MD simulations [50].

Profit from Symmetry

All DPD forces are central: $\mathbf{F}_{ij} = -\mathbf{F}_{ji}$for every two particles i and j. This restriction can be used to further reduce the computational efford. In the previous algorithm, the force between every two particles was calculated twice, once for (i, j),

once for (j, i). Instead of iterating first over each particle and second over each of its neighbors, one can build the calculation upon particle pairs:

```
for i in space :
    i.force = 0
for i,j in space.pairs(i.field) :
    if (i.pos-j.pos).length() < physics.cutoff :
        f = physics.pairwise_force(i,j)
        i.force += f
        j.force -= f
```

In this algorithm, `space.pairs` defines an iterator that acts in the following way: we first iterate over all particles. For every particle (in the following called center particle), we first iterate over its neighbors within the same field. However, because of the symmetry condition, we only need to iterate over those neighbors, which are further behind in the list that holds the particles of one field. Second, we iterate over all particles in half of the Moore neighborhood. Figure A.2 shows the reduces area that has to be taken into account by this improved iterator.

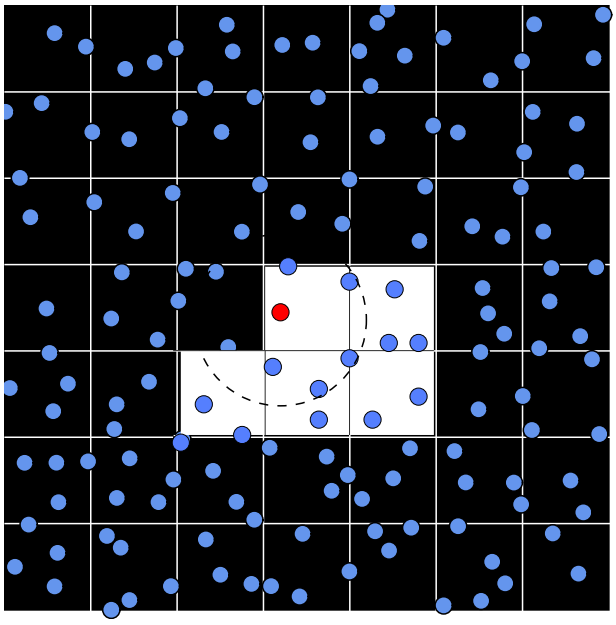

Figure A.2: By taking advantage of symmetric forces, one can reduce the computational efford further: Search of interaction partners can then be restricted to the white region in this figure. Doing so saves additional 50% of the calculations.

For each particle class the simulation we provide a seperate grid. This highly increases particle lookup when search possible partners for interaction. Espacially as water is not a reactant and most of the space is filled by water particles, this increases the computational speed of reactions by approximately 80% for the systems we analyzed.

Keeping track of neighbors

Although not implemented in our current work, we want to briefly discuss an alternative strategy to the *linked cell* algorithm, called the *linked list* algorithm. Following this procedure, the particle space is not partitioned. Instead, a list of particle pairs within the interaction range is repeatedly calculated. Basically, this leads back to the naive algorithm. However, the recalculation of the neighbor-list can be performed less often than the position/velocity update of the particles (In atomistic MD, this recalculation is usually done only every 100 timesteps) [50]. The *linked list* algorithm is easier to implement than the *linked cell* algorithm, however, the performance of the latter is better—especially then the box size is increased.
Nowaday high-end MD simulation packages combine both algorithms in a smart fashion: the binning of particle space improves the performance of linked list building. On the other hand, the list reduces distance calculation, where particle distance exceeds the cutoff, although particles may be in adjacent boxes. The ideal average improvement of the combined algorithm compared to the *linked cell* algorithm is determined by the ratio of sphere diameter to cube size (65% in two dimensions, 85% in three dimensions).

A.2 Numerical Solvers

In its original form, the DPD equations of motion (formula 3.2) have been solved with a slightly modified Euler integrator [35]. In the following years, much work has been done by R. D. Groot and P. B. Warren [38], K. E. Novik and P. Coveney [63], and especially I. Vattulainen and coworkers [64, 65, 66] to find better integrators for the special set of equations araising in DPD simulations.

A.2.1 Accounting randomness

Before we discuss possible integration schemes for the DPD equations of motion (3.2,3.5-3.6), we need to care about the stochastic term ξ in the calculation of $\mathbf{F}^R$. What needs to be done is relating the magnitude of the random force to the choosen step width Δt of the numerical solver. Otherwise, the mean variance of the random variable is not preserved and becomes bigger, the smaller we choose Δt as more intermediate steps are performed to simulate a given time interval. Further explanations on how ξ and Δt are exaclty related can be found in [38], where the random walk process introduced by ξ is related to the mean square replacement of particles. Here, we only mention that the factor with which ξ and therefore $\mathbf{F}^R$ need to be adjusted equals to $\Delta t^{-1/2}$. The random force then reads:

$$\hat{\mathbf{F}}_{ij}^R = \sigma \omega^R(r_{ij}) \xi_{ij} \mathbf{n}_{ij} \Delta t^{-1/2} \tag{A.8}$$

A.2.2 Basic Verlet integrator

Due to the fact, that the second derivate $d^2\mathbf{r}/dt^2$ is given explicitely in equation 3.2, the Verlet integrator (which is the standard integrator in atomistic MD simulations)

seems to be a good candidate for the numerical integration. Its scheme can be derived by two Taylor expansions around $r_i(t + \Delta t)$ and $r_i(t - \Delta t)$, respectively:

$$\begin{aligned}\mathbf{r}_i(t + \Delta t) &= \mathbf{r}_i(t) + \Delta t \frac{d\mathbf{r}_i}{dt} + \frac{1}{2}\Delta t^2 \frac{d^2\mathbf{r}_i}{dt^2} + \frac{1}{6}\frac{d^3\mathbf{r}_i}{dt^3} + O(\Delta t^4) \\ \mathbf{r}_i(t - \Delta t) &= \mathbf{r}_i(t) - \Delta t \frac{d\mathbf{r}_i}{dt} + \frac{1}{2}\Delta t^2 \frac{d^2\mathbf{r}_i}{dt^2} - \frac{1}{6}\frac{d^3\mathbf{r}_i}{dt^3} + O(\Delta t^4)\end{aligned}$$

Adding these two Equations and substituting $d^2\mathbf{r}_i/dt^2 = \mathbf{a}_i$ yields the classical Verlet integrator [67]:

$$\mathbf{r}_i(t + \Delta t) = 2\mathbf{r}_i(t) - \mathbf{r}_i(t - \Delta t) + \Delta t^2 \mathbf{a}_i(t) + O(\Delta t^4) \tag{A.9}$$

As one can see, this integrator is a forth order algorithm, but involves only slightly more efford than the somewhat oversimplified Euler scheme. To be precise, unlike other higher order numerical integrators (e. g. Runge-Kutta) the Verlet integrator uses only one function evaluation per time step.
A disadvantage of the basic integration scheme A.9 is that it only computes positions but no velocities. If we are, for example, interested in the temperature of the system, we need to calculate particle velocities afterwards. There are, however, variants of the Velocity algorithm, that compute both particle positions and velocities during their integration step.

A.2.3 Velocity Verlet integrator

It has been pointed out, that the Verlet integrator cannot accurately approximate the DPD equations of motion, because the force acting on a particle pair depends not only on their (relative) position, but their velocities, too. There have been proposed several modifications to circumvent this limitation. The one that has become sort of standard for DPD simulation has been developed by Allen and Tildesley [68] and was introduced into DPD by Groot and Warren [38]. This algorithm is similar to the so-called leapfrog variant of the Verlet algorithm, as velocities of the sytem are calculated at timesteps $(t + \lambda\Delta t)$ inbetween the positional update (t) (see figure A.3):

$$\begin{aligned}\mathbf{r}_i(t + \Delta t) &= \mathbf{r}_i(t) + \Delta t \mathbf{v}_i(t) + \frac{1}{2}\Delta t^2 \mathbf{a}_i(t) \\ \tilde{\mathbf{v}}_i(t + \lambda\Delta t) &= \mathbf{v}_i(t) + \lambda\Delta t \mathbf{a}_i(t) \\ \mathbf{a}_i(t + \Delta t) &= \frac{1}{m_i}\mathbf{F}_i(\mathbf{r}_i(t), \tilde{\mathbf{v}}_i(t + \lambda\Delta t)) \\ \mathbf{v}_i(t + \Delta t) &= \mathbf{v}_i(t) + \frac{1}{2}\Delta t(\mathbf{a}_i(t) + \mathbf{a}_i(t + \Delta t))\end{aligned} \tag{A.10}$$

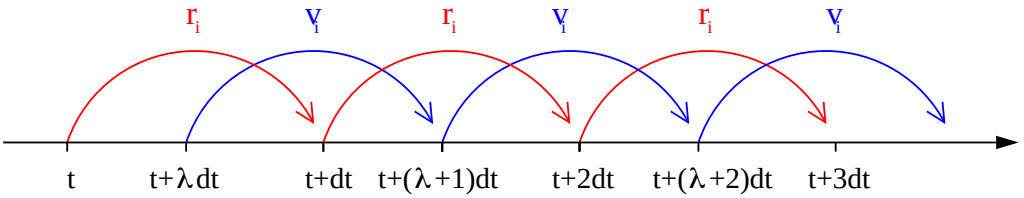

Figure A.3: Schematic view of the leapfrog Velocity Verlet algorithm: For the calculation of interaction forces, positions and velocities are evaluated at "interwoven" timesteps (see update scheme A.10).

Bibliography

[1] John Maynard Smith and E. Szathmary. *The Major Transitions in Evolution*. W. H. Freeman Press, New York, 1995.

[2] Aleksandr I. Oparin. *The Origin of Life on Earth*. Macmillan, New York, 1957.

[3] Pascale Angelica Bachmann, Pier Luigi Luisi, and Jacques Lang. Autocatalytic self-replicating micelles as models for prebiotic structures. *Nature*, 357:57–59, 1992.

[4] Peter V. Coveney, Andrew N. Emerton, and Bruce M. Boghosian. Simulation of self-reproducing micelles using a lattice-gas automaton. *J. Amer. Chem. Soc.*, 118:10719–10724, 1996.

[5] Daniel Segré, Dafna Ben-Eli, David W. Deamer, and Doron Lancet. The lipid world. *Origins of Life and Evolution of the Biosphere*, 31:119–145, 2001.

[6] D. Segré, D. Lancet, O. Kedem, and Y. Pilpel. Graded autocatalysis replication domain (GARD): Kinetic analysis of seelf-replication in mutually catalytic sets. *Origins of Life and Evolution of the Biosphere*, 28:501–514, 1996.

[7] Daniel Segré, Doron Lancet, Ora Kedem, and Yitzhak Pilpel. Graded autocatalysis replication domain (gard): Kinetic analysis of self-replication in mutually catalytic sets. *Origins of Life and Evolution of the Biosphere*, 28:501–514, 1998.

[8] Daniel Segré and Doron Lancet. A statistical chemistry approach to the origin of life. *Chemtracts - Biochemistry and Molecular Biology*, 12:382–397, 1999.

[9] Doron Lancet. Composing life. *EMBO reports*, 1(3):217–222, 2000.

[10] Daniel Segré and Doron Lancet. *Exobiology: Matter, Energy and Information in the Origin and Evolution of Life in the Univers*, chapter Mutually Catalytic Amphiphiles: Simulated Chemical Evolution and Implications to Exobiology, pages 123–131. Kluwer Academic Publishers, The Netherlands, 1998.

[11] D. Lancet. private communication. June 2005.

[12] Tobias Baumgart, Samuel T. Hessm, and Watt W. Webb. Imaging coexisting fluid domains in biomembrane models coupling curvature and line tension. *Nature*, 425:821–824, 2003.

[13] Satoru Yamamoto and Shi-Aki Hyodo. Budding and fission dynamics of two-component vesicles. *Journal of Chemical Physics*, 118(17):7937–7943, 2003.

[14] August Andersson. *The Application of Isotropic Bicelles as Model Membranes*. PhD thesis, Stockholm University, 2005.

[15] P. L. Luisi, P. Walde, and Oberholzer T. Enzymatic RNA synthesis in self-reproducing vesicles: An approach to the construction of a minimal synthetic cell. *Ber. Bunsenges. Phys. Chem.*, 98:1160–1165, 1994.

[16] A. Pohorille and D. Deamer. Artificial cells: prospects for biotechnology. *Trends in Biotechnology*, 20:123–128, 2002.

[17] Tibor Ganti. *The Principles of Life*. Oxford University Press, 2003.

[18] Steen Rasmussen, Liaohai Chen, Martin Nilsson, and Shigeaki Abe. Bridging nonliving and living matter. *Artificial Life*, 9:269–316, 2003.

[19] Martin M Hanczyc and Jack W Szostak. Replicating vesicles as models of primitive cell growth and division. *Current Opinion in Chemical Biology*, 8:660?664, 2004.

[20] C. Tanford. *The Hydrophobic Effect*. Wiley-Interscience, 1973.

[21] P.L. Privalov and S.J. Gill. Stability of protein structure and hydrophobic interaction. *Advances in Protein Chemestry*, 39:191–234, 1988.

[22] J Israelachvili, D. J. Mitchell, and B. W. Ninham. Theory of self-assembly of hydrocarbon amphiphiles into micelles and bilayers. *J. Chem Soc. Faraday Trans.*, 72(2):1525–1568, 1976.

[23] R. Nagarajan. Molecular packing parameter and surfactant self-assembly: The neglected role of the surfactant tail. *Langmuir*, 18:31–38, 2002.

[24] D. Fennell Evans and Hakan Wennerström. *The Colloidal Domain - Where Physics, Chemistry, Biology, and Technology Meet*. Wiley-VCH, New York, Chichester, Weinheim, Brisbane, Singapore, Toronto, 1999.

[25] E. A. G. Aniansson, S. N. Wall, M. Almgren, H. Hoffmann, L. Kielmann, W. J. Ulbricht, R. Zana, J. Lang, and C. Tondre. Theory of the kinetics of micellar equilibria and quantitative interpretation of chemical relaxation studies of micellar solutions of ionic surfactants. *J. Phys. Chem.*, 80:905, 1976.

[26] E. A. G. Aniansson and S. N. Wall. On the kinetics of step-wise micelle association. *J. Phys. Chem.*, 78:1024, 1974.

[27] E. A. G. Anianssin and S. N. Wall. A correction and improvement of "on the kinetics of step-wise micelle association". *J. Chem. Phys.*, 79:857, 1975.

[28] Alexander Patist, James R. Kanicky, Pavan K. Shukla, and Dinesh O. Shah. Importance of micellar kinetics in relation to technological processes. *Journal of Colloid and Interface Sciences*, 245:1–15, 2002.

[29] E. Lessner, M. Teubner, and M. Kahlweit. Relaxation experiments in aqueous solutions of ionic micelles. 2. experiments on the system water-sodium dodecyl sulfate-sodium perchlorate and their theoretical interpretation. *J. Phys. Chem.*, 85:3167 – 3175, 1981.

[30] J.-B. Mailet, V. Lachet, and Peter V. Coveney. Large scale molecular dynamics simulation of self-assembly processes in short and long chain cationic surfactants. *Phys. Chem. Chem. Phys.*, 1:5277–5290, 1999.

[31] Alexander P. Lyubartsev and Aatto Laaksonen. On the reduction of molecular degrees of freedom in computer simulations. *Lect. Notes Phys.*, 640:219–244, 2004.

[32] U. Frisch, B. Hasslacher, and Y. Pomeau. Lattice-gas automata for the Navier-Stokes equation. *Physical Review Letters*, 56:1505–1508, 1986.

[33] U. Frisch, D. d' Humires, B. Hasslacher, and and Y. Pomeau P. Lallemand. Lattice gas hydrodynamics in two and three dimensions. *Complex Systems*, 1:649–707, 1987.

[34] James Maxwell Buik. *Lattice Boltzmann Methods in Interfacial Wave Modelling*. PhD thesis, University of Edinborgh, 1997.

[35] P. J. Hoogerbrugge and J. M. V. A. Koelman. Simulating microscopic hydrodynamic phenomena with dissipative particle dynamics. *Europhys. Lett.*, 19:155–160, 1992.

[36] P. Español and P. Warren. Statistical mechanics of dissipative particle dynamics. *Europhys. Lett.*, 30:191–196, 1995.

[37] Pep Español. Dissipative particle dynamics revisited. *Simu Challanges in Molecular Simulations*, pages 59–77, 2002.

[38] R. D. Groot and P. B. Warren. Dissipative particle dynamics: Bridging the gap between atomistic and mesoscale simulation. *J. Chem. Phys.*, 107(11):4423–4435, 1997.

[39] Colin Marsh. *Theoretical Aspects of Dissipative Particle Dynamics*. PhD thesis, Lincoln College, University of Oxford, 1998.

[40] I. Pagonabarraga and D. Frenkel. Dissipative particle dynamics for interacting systems. *Journal of Chemical Physics*, 115:5015–5026, 2001.

[41] Gianni De Fabritiis, Peter V. Coveney, and Eirik G. Flekkoy. Multiscale dissipative particle dynamics. *Phil. Trans. R. Soc. Lond. A*, 360:317–331, 2002.

[42] S. Y. Trofimov, E. L. F. Nies, and M. A. J. Michels. Thermodynamic consistency in dissipative particle dynamics simulations of strong ideal liquids and liquid mixtures. *Journal of Chemical Physics*, 117(20):9383–9394, 2002.

[43] Sergey Y. Trofimov. *Thermodynamic consistency in dissipative particle dynamics*. PhD thesis, Technische Universiteit Eindhoven, 2003.

[44] Bruce M. Forrest and Ulrich W. Suter. Accelerated equilibration of polymer melts by time-coarse-graining. *J. Chem. Phys.*, 102(18):7256–7266, 1995.

[45] R. K. Pathria. *Statistical Mechanics*. Pergamom Press, Oxford, New York, Toronto, Sydney, Paris, Frankfurt, 1972.

[46] Naoki Ono. *Artificial Chemistry: Computational Studies on the Emergence of Self-Reproducing Units*. PhD thesis, Institute of Physics, University of Tokyo, 3-8-1 Komaba Meguro-ku, Tokyo 153-8902, Japan, 2001.

[47] Kampen N. G. *Stochastic Processes in Physics and Chemistry*. North-Holland Publishing Company, Amsterdam, New York, Oxford, 1981.

[48] J. M. V. A. Koelman and P. J. Hoogerbrugge. Dynamic simulations of hard-sphere suspensions under steady shear. *Europhys. Lett.*, 21(3):363–368, 1993.

[49] N. S. Martys. Study of a dissipative particle dynamics based approach for modeling suspensions. *J. Rheol.*, 49(2):401–424, 2005.

[50] James S. Sims and Nicos S. Martys. Simulation of sheared suspensions with a parallel implementation of QDPD. *Journal of Research of the National Institute of Standards and Technology*, 109(2):267–277, 2004.

[51] Y. Kong, C. W. Manke, W. G. Madden, and A. G. Schlijper. Effect of solvent quality on the conformation and relaxation of polymers via dissipative particle dynamics. *J. Chem. Phys.*, 107:592, 1997.

[52] Y. Kong, C. W. Manke, W. G. Madden, and A. G. Schlijper. Modeling the rheology of of polymer sulotions by dissipative particle dynamics. *Tribology Letters*, 3:133, 1997.

[53] M. Venturoli and B. Smit. Simulating self-assembly of model membranes. *Phys. Chem. Comm.*, 10, 1999.

[54] R. D. Groot and K. L. Rabone. Mesoscopic simulation of cell membrane damage, morphology change and rupture by nonionic sufactants. *Biophysical Journal*, 81:725–736, 2001.

[55] Satoru Yamamoto, Yutaka Maruyama, and Shi aki Hyodo. Dissipative particle dynamics study of spontaneous vesicle formation. *Journal Chemical Phsyics*, 116(13):5842–5849 5842–5849, 2002.

[56] R. D. Groot. Mesoscopic simulation of polymer-surfactant aggregation. *Langmuir*, 16:7493–7502, 2000.

[57] R. D. Groot. Electrostatic interactions in dissipative particle dynamics-simulation of polyelectrolytes and anionic surfactants. *J. Chem. Phys.*, 118(24):11265–11277, 2003.

[58] Patrick B. Warren. Vapor-liquid coexistence in many-body dissipative particle dynamics. *Physical Review E*, 68:066702, 2003.

[59] Foley, v. Dam, Feiner, and Hughes. *Computer Graphics: Principles and Practice in C*. Addison Wesley, New York, 1996.

[60] Martin Hanczyc. private communication. June 2005.

[61] Julian C. Shillcock and Reinhard Lipowsky. Equilibrium structure and lateral stress distribution of amphiphilic bilayers from dissipative particle dynamics simulations. *Journal of Chemical Physics*, 117(10):5048–5061, 2002.

[62] Gil Bankö and Steen Rasmussen. private communication. October 2005.

[63] K. E. Novik and P. V. Coveney. Finite-difference methods for simulation models incorporating nonconservative forces. *J. Chem. Phys.*, 109(18):7667–7677, 1998.

[64] Gerhard Besold, Ilpo Vattulainen, Mikko Karttunen, and James M. Polson. Towards better integrators for dissipative particle dynamics simulations. *Physical Review E*, 62:7611–7614, 2000.

[65] I. Vattulainen, M. Karttunen, G. Besold, and J. M. Polson. Integration schemes for dissipative particle dynamics simulations: From softly interacting systems towards hybrid models. *J. Chem. Phys.*, 116:3967–3979, 2002.

[66] P. Nikunen, M. Karttunen, and I. Vattulainen. How would you integrate the equations of the motion in dissipative particle dynamics simulations? *Computer Physics Communications*, 153:407–423, 2003.

[67] Loup Verlet. Computer "Experiments" on classical fluids. i. thermodynamical properties of lennard-jones molecules. *Phys. Rev.*, 159:98–103, 1967.

[68] M. P. Allen and D. J. Tildesley. *Computer Simulation of Liquids*. Clarendon, Oxford, 1987.

Beiträge des Instituts für Umweltsystemforschung der Universität Osnabrück

1. Eberhard Umbach: Umweltverträgliches Wirtschaftssystem in den Bereichen Abfall und Emissionen. März 1997.

2. Stefan Trapp, Bernhard Reiter, Michael Matthies: Überprüfung und Fortentwicklung der Bodenwerte für den Boden-Pflanze-Pfad - Teilprojekt Transferfaktoren Boden-Pflanze. August 1997.

3. Michael Matthies (Hrsg.): Stoffstromanalyse und Bewertung. September 1997.

4. Dirk Melcher: Quantifizierung, Klassifizierung und Modellierung der Phytotoxizität organischer Chemikalien. Oktober 1997.

5. Stefan Schwartz: Organische Schadstoffe in der Nahrungskette - Vorstudie zur Validierung von Expositionsmodellen. November 1997.

6. Volker Berding: Private Hausbrunnen - Vergleichende Bewertung von Maßnahmen zur Verbesserung der Trinkwasserqualität. Oktober 1997.

7. Horst Malchow (Hrsg.): Modellbildung und -anwendung in den Wissenschaften I.
   Januar 1998.

8. Birgit Radtke: Bifurkationen in einem Modell mariner Planktondynamik. Januar 1998.

9. Werner Berens: Konzeption eines Umweltinformationssystems für die Universität Osnabrück. Juni 1998.

10. Michael Matthies (Hrsg.): Studienprojekte 1998. September 1998.

11. Michael Matthies (Hrsg.): Globaler Wandel. September 1998.

12. Klaus Brauer (Hrsg.): Institutsbericht. September 1998.

13. Klaus Brauer, Horst Malchow, Michael Matthies, Eberhard Umbach (Hrsg.): Materialien des Arbeitstreffens Systemwissenschaft in der Lehre, Universität Osnabrück, 29./30.9.1998.
    Dezember 1998.

14. Horst Malchow (Hrsg.): Modellbildung und -anwendung in den Wissenschaften II.
    Dezember 1998.

15. Horst Malchow (Hrsg.): Modellbildung und -anwendung in den Wissenschaften III.
    August 1999.

16. Michael Matthies (Hrsg.): Regionale Nachhaltigkeit. September 2000.

17. Markus Klein: Langjähriger Wasserhaushalt von Gras- und Waldbeständen. Entwicklung, Kalibrierung und Anwendung des Modells LYFE am Groß-Lysimeter St. Arnold.
    Juni 2000.

18. Markus Brune: Multimediale Umweltmodellierung mit Fuzzy-Mengen. Juli 2000.

19. Michael Matthies (Hrsg.): Fraktale in Hydrologie und Biologie. Oktober 2000.

20. Stefan Fuest (Dissertation): Regionale Grundwassergefährdung durch Nitrat. Dezember 2000.

21. Carsten Schulze (Dissertation): Modelling and evaluating the aquatic fate of detergents.
    Januar 2001.

Die Beiträge können gegen einen Selbstkostenpreis (ca. 10 EUR pro Exemplar) beim Institut für Umweltsystemforschung, Universität Osnabrück, 49069 Osnabrück bestellt werden.

Alle folgenden Beitrge sind herunterzuladen unter `http://www.usf.uos.de/usf/beitraege/`.

22. Horst Malchow (Hrsg.): Modellbildung und -anwendung in den Wissenschaften IV.
    Januar 2001.

23. Horst Malchow (Hrsg.): Modellbildung und -anwendung in den Wissenschaften V.
    August 2001.

24. Kai Leßmann (Diplomarbeit): Probabilistic Exposure Assessment. Parameter Uncertainties and their Effects on Model Output. November 2002.

25. Frank M. Hilker (Diplomarbeit): Parametrisierung von Metapopulationsmodellen.
    März 2003.

26. Nadja Rüger(Diplomarbeit): Habitat suitability for Populus euphratica in the Northern Amudarya delta - a fuzzy approach. Juni 2003.

27. Claudia Pahl-Wostl, Eva Ebenhöh (Hrsg.): Komplexe Adaptive Systeme. Juli 2003.

28. Horst Malchow (Hrsg.): Chaos und Ordnung in Natur und Gesellschaft. Dezember 2004.

29. Andreas Focks (Diplomarbeit): Modeling the transfer of antibiotic drug resistance genes between E. coli strains. Juni 2005.

30. Christiane Zarfl (Diplomarbeit): Modellierung von Arsen in der Mulde. Juni 2005.

31. Sven Lautenbach (Dissertation): Modellintegration zur Entscheidungsunterstützung fr die Gewässergütebewirtschaftung im Einzugsgebiet der Elbe. November 2005.

32. Frank M. Hilker and Frank H. Westerhoff: Control of chaotic population dynamics: Ecological and economic considerations. November 2005.

33. Harold Fellermann (Diplomarbeit): Micelles as containers for protocells. Dezember 2005.

ISSN 1433-3805